Investigation of the effect of an adjustable rear-end wing-type spoiler on aerodynamic braking performance of vehicle: A case of Suzuki Dzire

Tsinukal Aklilu Bekele

A Thesis Submitted to the Department of Mechanical Engineering

School of Mechanical, Chemical and Materials Engineering

Presented in Partial Fulfillment of the Requirement for the Degree of Master of Science in Automotive Engineering

Office of Graduate Studies

Adama Science and Technology University

June, 2024

Adama, Ethiopia

Investigation of the effect of an adjustable rear-end wing-type spoiler on aerodynamic braking performance of vehicle: A case of Suzuki Dzire

Tsinukal Aklilu Bekele

Advisor: Dr. Ramesh Babu Nallamothu

A Thesis Submitted to Department of Mechanical Engineering

School of Mechanical, Chemical and Materials Engineering

Presented in Partial Fulfillment of the Requirement for the Degree of Master of Science in Automotive Engineering

Office of Graduate Studies

Adama Science and Technology University

June, 2024

Adama, Ethiopia

DECLARATION

I hereby declare that this Master Thesis entitled **"Investigation of the effect of an adjustable rear-end wing-type spoiler on aerodynamic braking performance of vehicle: A case of Suzuki Dzire"** is my original work and that has not been submitted to any other university for similar purpose. The references used in this proposal are duly recognized by proper citation.

____________________	____________________	________________
Name of the student	Signature	Date

RECOMMENDATION

I, the advisor of this thesis, hereby certify that I/we have closely advised the student while developing this thesis and read the revised version of the thesis entitled **"Investigation of the effect of an adjustable rear-end wing-type spoiler on aerodynamic braking performance of vehicle: A case of Suzuki Dzire"** prepared under my/our guidance by Tsinukal Aklilu Bekele. Therefore, I recommend the submission of a revised version of the thesis to the department following the applicable procedures.

.

______________________	______________________	______________
Major Advisor	Signature	Date

APPROVAL

I, the advisors of the thesis entitled **"Investigation of the effect of an adjustable rear-end wing-type spoiler on aerodynamic braking performance of vehicle: A case of Suzuki Dzire"** and developed by Tsinukal Aklilu; hereby certify that the recommendation and suggestions made by the board of examiners are appropriately incorporated into the final version of the thesis.

________________________ ________________________ ________________

Major Advisor Signature Date

We, the undersigned, members of the Board of Examiners of the thesis by Tsinukal Aklilu have read and evaluate the thesis entitled **"Investigation of the effect of an adjustable rear-end wing-type spoiler on aerodynamic braking performance of vehicle: A case of Suzuki Dzire"** and examine the candidate during the open defense. This is, therefore, to certify that the thesis accepted for partial fulfillment of the requirement of the degree of Master of Science in Automotive Engineering.

________________________ ________________________ ________________

Chairperson Signature Date

________________________ ________________________ ________________

Internal examiner Signature Date

________________________ ________________________ ________________

External examiner Signature Date

Final approval and acceptance of the thesis is contingent upon submission of its final copy to the Office of Postgraduate Studies (OPGS) through the Department Graduate Council (DGC) and School Graduate Committee (SGC).

________________________ ________________________ ________________

Department head Signature Date

________________________ ________________________ ________________

School Dean Signature Date

________________________ ________________________ ________________

Office of Postgraduate Studies, Dean Signature Date

ACKNOWLEDGMENT

My first and greatest thanks are to almighty God, for letting me through all difficulties and helped me to complete this thesis. Next, I would like to acknowledge and express my deepest gratitude to my advisor Dr. Ramesh Babu Nallamothu for his guidance on this thesis work. Last but not least, I am grateful for all of the people who have helped to make my thesis a success by providing inspiration, support, and guidance.

TABLE OF CONTENTS

ACRONYMS AND NOMENCLATURES

API	Application Programming Interface
ASME	American Society of Mechanical Engineers
CAD	Computer Aided Design
CPU	Central Processing Unit
CFD	Computational Fluid Dynamics
DC	Direct Current
DNS	Direct Numerical Simulation
EMR	Electro mechanical relays
FVM	Finite Volume Method
GCI	Grid Convergence Index
GND	Ground
GRA	Grey Relation Analysis
IDE	Integrated Development Environment
LCD	Liquid Crystal Display
LED	Light Emitting Diode
LES	Large Eddy Simulation
NACA	National Advisory Committee for Aeronautics
PDE	Partial Differential Equation
PWM	Pulse Width Modulation
RANS	Reynolds-Averaged Navier-Stokes
RNG	Realizable k-epsilon model
SSR	Solid State Relay
SST	Shear Stress Transport
TCW	Tinned Copper Wire
USB	Universal Serial Bus
3D	Three Dimension
V	Speed

Km/h	Kilometer per hour
m/s	Meter per second
G	Gravity
c_d	Coefficient of drag
c_l	Coefficient of lift
c_s	Coefficient of side
F_d	Drag force
F_l	Lift force
F_s	Side force
ρ	Density
E	Epsilon
Ω	Omega
%	Present
T	Temperature
V	Speed
μ_t	Eddy viscosity
Re	Reynolds number
A	Frontal area

LIST OF TABLES

LIST OF FIGURES

ABSTRACT

When a vehicle travels at high speed, it may face a variety of aerodynamic challenges. These challenges can have a significant impact on vehicle performance. One of these challenges is lift, which is related to unstable handling and reduced braking performance. Fortunately, by using suitable aerodynamic devices like rear-end wing- type spoilers, these challenges can be reduced. This thesis work shows an Investigation of the effect of an adjustable rear-end wing-type spoiler on aerodynamic braking performance of vehicle. The baseline model of the Suzuki Dzire car and the wing-type spoiler (half section NACA 0012 airfoil) were designed by SOLIDWORKS 2023 software. The coefficient of aerodynamic forces of a Baseline model car with and without a rear-end wing-spoiler at different angles of inclination (0, 10, 20, 30, 40, 50, and 90 angles) was analyzed using ANSYS Fluent 2022 software at different speeds (80, 120, and 160 km/h). The results indicated that as the angle increased, both the drag and negative lift also increased. The braking distance was also calculated, and at model seven, the maximum reduction of braking distance was achieved. It can reduce 9.1% compared to the model one on the icy road. A prototype was built to demonstrate the functionality of the adjustable spoiler. The prototype has both software and hardware components. The software component is the code that runs on the microcontroller. The programming was written using ARDUINO IDE software, and the circuits were designed and performed using Proteus and Cirkit Designer software. The hardware components (including an Arduino UNO board, solid state relay, solenoid, breadboard, brake switch, infrared speed sensor, LCD, DC motor circuit wire, and DC motor PWM speed controller) were assembled to create the prototype of an adjustable rear-end wing-type spoiler.

Keywords: Aerodynamic, Aerodynamic brake**,** Drag, lift, spoiler, prototype

CHAPTER ONE
INTRODUCTION

1.1 Background of the study

The Aerodynamics of a vehicle are a crucial factor that needs to be considered when designing the shape of cars. This is important for various reasons, such as improving vehicle performance, reducing fuel consumption, enhancing lateral stability and increasing safety while braking (Janković & Dukic, 2011). The primary concerns of users have consistently revolved around safety and fuel efficiency (Yakkundi, 2018). Excessive drag forces on the automobile's body can result in excessive engine energy waste, whilst excessive lift forces can make the car unstable and unsafe to drive. Because of the design of a sedan, the lift force is usually concentrated in the back of the vehicle. Moving at fast speeds causes high-speed air to follow the car's body shape, resulting in significant pressure on the front hood and front windshield. However, as the air approaches the car's back, it loses its track, causing turbulence in the airflow and producing a low-pressure zone near the car's rear. This low pressure is problematic since it could cause the back of the car to lift and the tires lose attachment to the road, resulting in an accident (Nawam et al., 2018). The aerodynamic force is beneficial for vehicles travels at high speed as it not only improves their handling but also enhances their braking performance. Initially, devices for active aerodynamic control were used to enhance racing vehicles' ability to brake. For example, let's take the 1968 Porsche 908LH as an instance. This car had two flaps positioned at the back that would automatically rise when braking, increasing both the downforce and drag (Kurec et al., 2019). Traditional braking systems rely on the relationship between wheels as well as the surface of the road. However, their effectiveness can be limited by factors like friction or uneven roads. So, it becomes crucial to explore braking methods that can address these challenges and improve brakes to reduce stopping distances. While alternative braking systems might require space and longer activation time it may not be practical due, to their size constraints. Nevertheless, incorporating configurations could potentially enhance a car's braking capability by complementing the existing system (Ramar et al., 2020).

Active control of aerodynamics, in vehicles offers advantages; 1) It can help reduce air resistance and fuel consumption when driving at high speeds, 2) During braking, the adjustable wing plate can be utilized to increase the vehicles wind facing surface area thereby increasing resistance and reducing the amount of braking force required by the tires. 3) At high speeds, active aerodynamic mechanisms can improve downward force and expand the operational capabilities of the tires. These active aerodynamic systems were employed to elevate the drag coefficient for braking purposes. A mechanism was devised that generated deceleration, through the utilization of resistance (Muralidharan et al., 2018).

A technique called braking utilizes the forces of air to enhance a vehicle braking capability. This feature is commonly found in high performance cars, sports cars. To assist in deceleration the air brake applies increased resistance to the vehicles motion. Typically, an air brake is a component attached to the vehicles body, such, as a spoiler or flap. When activated it disrupts the airflow in front of the vehicle. Causes separation in the airflow behind it. This significantly increases resistance and aids in slowing down the vehicle. The air brake proves useful for sports cars during braking situations. Depending on speed and road conditions it can decrease lift and increase drag potentially reducing stopping distance. This enhancement, in braking efficiency contributes to driving safety improvements (Kurec et al., 2019). Airfoils have gained popularity as wings, for cars in recent years because they can decrease lift (increase downward force) and modify drag based on the angle of the wing (Ramar et al., 2020). A rear-wing spoiler is a device installed at the back of a vehicle to improve aerodynamics and stability by reducing undesirable movement of airflow around the vehicle's surface. Commonly fitted on the trunk lid of a passenger vehicle (Nawam et al., 2018). Unlike performance and racing cars regular passenger vehicles do not currently incorporate air brakes. This is primarily due, to a lack of research and studies focused on improving braking specifically for these types of cars. While air brakes have proven successful in high performance automobiles their implementation in passenger vehicles has not received attention. In today's aerospace industries Computational Fluid Dynamics (CFD) simulations are widely used to apply aerodynamics during product development. By utilizing this technology engineers can optimize the performance of a design and gain insights into the underlying processes without the need for testing of numerous prototypes. Furthermore, CFD provides a tool for flow pattern visualization providing insights, into flow physics that would otherwise be challenging or expensive to obtain through traditional experimentation (Leary, 2010). In computational fluid dynamics (CFD), turbulent flows are simulated through the use of turbulence models. The RANS model is another approach used to simulate turbulent flow. Because of its low computing requirements and affordability, it has been the core of the current CFD method for simulating turbulent flow for the past few decades. The aim of this study is to investigate the effect of an adjustable rear-end wing-type spoiler at different angles of inclination and speeds on a Suzuki Desire car to enhance aerodynamic braking performance. This study employs a numerical simulation method using the ANSYS Fluent 2022 software to analyze the drag and lift coefficients. Additionally, a demonstration model was developed to control the angle of inclination of the spoiler.

1.2 Statement of the problem

Vehicles typically use conventional braking systems, may not always be effective enough to significantly reduce braking distances. The performance of these brakes depends on the interaction between the wheels and the road surface. Their effectiveness can be limited by factors such as friction levels and road conditions, including uneven or slippery surfaces. As a result, many auxiliary braking systems have been developed but they take up a lot of space for mounting (Ramar et al., 2020). The application of an aerodynamic airbrake system is one way to address this issue. This work helps in reducing those problems by using an adjustable wing-type spoiler. At high speeds, a lower angle maintains optimal stability and handling. Conversely, during high deceleration, a higher angle increases drag force, acting as an aerodynamic brake to shorten braking distance.

1.3 Objectives

1.3.1 General objective

The general objective of this thesis work is to investigate the effect of an adjustable rear-end wing-type spoiler on aerodynamic braking performance of vehicle.

1.3.2 Specific objectives

- To model the baseline model of the Suzuki Dzire car and spoiler by using SOLIDWORKS CAD modeling software.
- To analyze the drag and lift at different angles of the spoiler with varying speed by using CFD software.
- To design circuit for actuating adjustable spoiler and write a controller program.
- To develop the prototype to show the working principle of the adjustable spoiler system.

1.4 Significance of the study

This study work examine how a vehicle's aerodynamics impact its safety and performance. This study work helps in:

- Reducing risk of accident
- Minimizing wear and tear on brake parts
- Improving handling, stability and ride quality
- Serving as a resource and point of reference for the future researchers in the related field of study.

1.5 Scope of the Study

This study investigates the impact of an adjustable rear-end wing-type spoiler on aerodynamic drag and lift during acceleration and deceleration for the Suzuki Dzire car. The effects of drag force and lift force at different angles were analyzed using ANSYS Fluent software at various speeds for the Suzuki Dzire (baseline model), and the spoiler modeled using SOLIDWORKS 2023 software. And also, Arduino programming code was written and compiled using Arduino IDE software, proteus and Cirkit designer software used to design and simulate an electric circuit. Finally, a demonstration model was developed to control the angle of inclination of the spoiler during deceleration.

1.6 Limitations

In this study, there are some limitations due to a short period of time and financial constraints. The first limitation of this study is that it did not include an actual wind tunnel test (experimental) due to the high cost associated with printing a 3D model of the vehicle. Because there was an additional expense to make the prototype, and the CAD 3D model does not consider the side mirrors and front openings on the grille.

1.7 Organization of the study

This thesis is divided into six chapters. The first chapter serves as an introduction and includes the study's background, statement of the problem, objectives and scopes, significance of the study, and thesis organization. Chapter two presents a literature review that focuses on the effects of aerodynamics on on-road vehicles, improves the aerodynamic effect of passenger cars, provides a summary of the review, and identifies a research gap. The third chapter explains the materials and methods used to complete this thesis. Chapter four explains system modeling and analysis in ANSYS Fluent. Chapter five explains and presents the results obtained from ANSYS Fluent and the assembly of the prototype, including circuit diagrams. Finally, there is Chapter six, which includes a summary, conclusion, and recommendations.

CHAPTER TWO

LITERATURE REVIEW

2.1 Introduction

Understanding the study of aerodynamics and CFD analysis is important. Reviewing different literature is very important to fully understand the aerodynamic effects on vehicles. Literature review mainly include different researches on aerodynamics.

2.2 Aerodynamic forces

Various aerodynamic forces that affect vehicles on the road can have a major effect on their stability and performance. These forces, which induce uneven pressure on the vehicle's exterior and affect its motion dynamics, include aerodynamic drag, lift and side wind stability.

2.2.1 Drag force

Aerodynamic drag is the primary obstacle to movement. It is the force that opposes the path of motion and is brought on by a combination of viscous and friction elements. The viscous element is generated by turbulence from the car's body, which is the most important factor in vehicular motion. Aerodynamic drag, also known as wind resistance, is the force that slows down a vehicle as it moves through the air. When a vehicle moves forward, it disrupts the air flow, leading to a region of low pressure behind the car (the wake). This causes the high-pressure air around the wake to move through the region of low pressure, creating a force that pulls the vehicle backward (Vinith & Sathiamurthi, 2020).The equation below illustrates the connection between aerodynamic drag and vehicle speed.

$$F_d = \frac{1}{2} c_d A \rho v^2 \tag{2. 1}$$

This indicates that the drag force (F_d) on the vehicle is directly related to the frontal area (A), air pressure (ρ), vehicle speed (V), and a factor representing the vehicle's shape called the drag coefficient (c_d). Therefore, the key elements for reducing the total resistance of a car are its drag coefficient and frontal area.

The frontal area refers to the overall two-dimensional space visible to an observer from the front of the car. Designers face limitations in reducing this area due to the impact of the ergonomics of the seats for the driver and passengers on the overall frontal shape of the car. Figure 2.1 shows the frontal area of the vehicle.

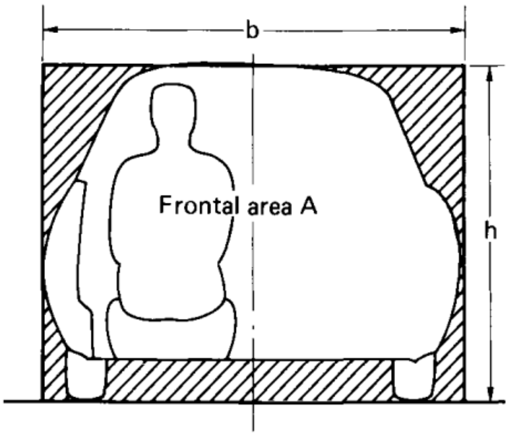

Car class	Frontal area A [m²]
Mini	1.8
Medium size	1.9
Upper medium size	2.0
Full size	2.1

Figure 2.1. Vehicle Frontal Area (Hucho & Ahmed, 1987)

Therefore, the most influential variable to control in Equation (1) is the drag coefficient of the vehicles. The drag coefficient is a unitless parameter that quantifies the level of aerodynamic resistance a blunt body creates in the airflow around it. A lower coefficient indicates reduced air resistance for the object as it moves through the air.

2.2.2 Lift force

The lift force acts vertically on the vehicle body, causing it to be lifted into the air when applied in the positive direction. Conversely, if applied in the negative direction, it can lead to increase downward force on the wheels. The formula commonly used to describe this force is typically expressed as

$$F_L = \frac{1}{2} c_L A \rho v^2 \qquad (2.\ 2)$$

This indicates that the lift force (F_L) on the vehicle is directly related to the frontal area (A), air pressure (ρ), vehicle speed (V), and the lift coefficient (c_L) (Cakir, 2012).

This occurrence has a much smaller impact on regular vehicles compared to drag, as it has a minimal effect at speeds under 100 km/h. additionally, the lift force doesn't impede the vehicle's movement. Therefore, the majority of production vehicles do not utilize aerodynamic devices intended to generate negative lift force. Instead, most modern road vehicles use aerodynamic aids that reduce the vehicle's lift coefficient and also decrease the drag acting on the vehicle (Jesshope, 2012).

The primary cause of the lift force is the pressure differential between the object's top and bottom surfaces. A major factor in lift creation is the conservation of mass and Bernoulli's principle. The air traveling over the top of the vehicle has a longer distance to travel compared to the air traveling underneath. Since the attributes were identical on both sides of the vehicle before being separated, their overall pressure remains constant. The air which

travels the longest distance will be compelled to speed up due to the streamline's air particles behind it. This air moving more quickly will have a lower static pressure value, given that a portion of the pressure remained converted to dynamic pressure during the increase in velocity. Consequently, there is a difference in the static pressure of the air on the upper and lower sides of the vehicle. This imbalance results in a lift force because the vehicle is pushed upward by the high static pressure side and pulled upward by the low static pressure side. The lift force theory provided indicates the lift force's direction of action is shown below.
Wind tunnel testing was done on a Volkswagen 1600 coupe to evaluate various aerodynamic devices and how they affected lift and drag forces. Figure 2.2, shows the overall lift and drag coefficients of a vehicle with and without a spoiler.

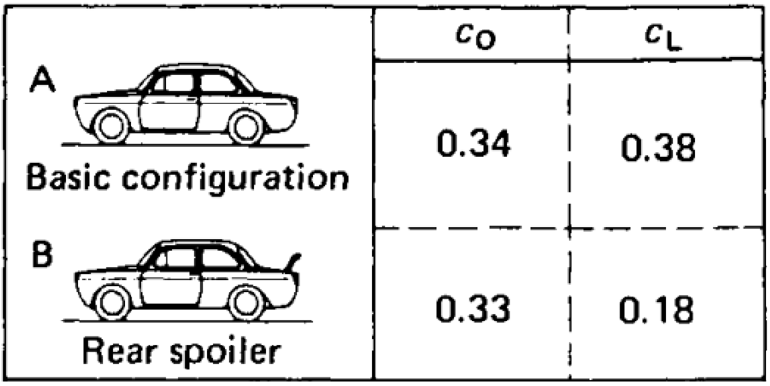

Figure 2.2. The Effect of a Spoiler on Drag and Lift (Hucho & Ahmed, 1987)

The vehicle's lift coefficient was reduced by more than 50% with the installation of the spoiler, and there was a slight decrease in the drag coefficient as well, as illustrated in Figure 2.2 (Hucho & Ahmed, 1987).

2.3 Factors affecting drag

A solid body moving through a gas or fluid will cause the fluid to try to slow down or resist the motion of the body. The aerodynamic force opposing an object's motion in that direction is called the drag force. The drag force effect is the main subject of the current study (Saxena et al., 2020).

2.3.1 Shape of the Object

The shapes of different objects have a significant impact on the formation of drag. The degree of drag is also influenced by the size of the item as it passes through air or a fluid. The formation of drag is a result of variation in pressure surrounding an object and is determined by the cross-sectional area at its front. Furthermore, an object's three-dimensional shape influences its friction drag, which is influenced by the object's surface roughness. Figure 2.3, shows the aerodynamic drag coefficient for various shapes.

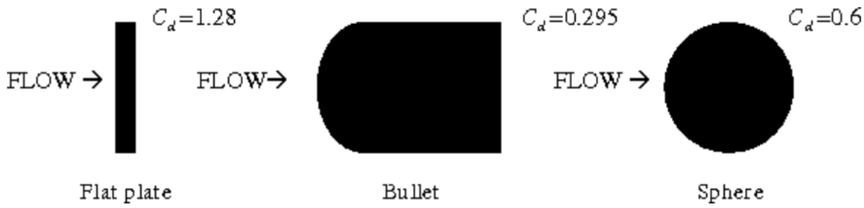

Figure 2.3. Drag Coefficients of standard shapes (Gemba, 2007)

2.3.2 Motion of the Air

Drag is linked to the movement of an object through the air and is influenced by the air's velocity. Similar to lift, drag changes in relation to the square of the object's relative velocity in the air. The angle of the object in relation to the airflow also impacts the level of drag produced by a specific shaped object. When the object travels at speeds close to the speed of sound, shock waves form on the object, resulting in an additional drag component called wave drag. The object's motion through the air also leads to the formation of boundary layers on its surface, which are regions of very slow-flowing air that contribute to skin friction.

2.3.3 Properties of the Air

Drag is directly correlated to the mass of the flow passing the object. Drag is also complexly related to two other air properties: viscosity and compressibility. These factors influence wave drag and skin friction. The drag equation is a single mathematical equation that incorporates all of the information about the components that influence drags. The drag equation allows you to anticipate how much drag force a given body will generate as it moves through a given fluid at a specific speed.

2.4 Factors that affect the flow field around the vehicle

A vehicle's flow field is influenced by several variables. In studies that examine Aerodynamic effects of a rear wing or spoiler on passenger vehicles, factors such as the boundary layer, flow separation, Reynolds number, pressure distribution, and friction drag have a notable impact on the flow patterns surrounding the vehicle (Selvaraju et al., 2015).

2.4.1 Flow separation

Basic fluid dynamics and a variety of engineering applications are also very interested in flow separation control (Sudin et al., 2014).There are certain moments when the fluid's flow across the vehicle's surface stalls and reverses direction due to the change in velocity. The term "separation" refers to the division of the fluid flow. This typically happens at the back of the car. The outer layer of the flow imposes a pressure distribution that mostly determines this separation. The flow field surrounding the car is impacted by this separation since it causes the flow trailing the vehicle to alter in behavior. When examining the vehicle's wake, this phenomenon is the main thing to take into account. Flow separation reduces pressure recovery because it causes a bigger wake and less pressure on the back surface. The airflow pathway between the roof and the rear window should be smoother to avoid insufficient airflow separation. (Cakir, 2012). In comparison to laminar flow, the turbulent boundary layer can endure significantly higher pressure with no separating. This separation leads the flow to change as it moves behind the vehicle, and hence affects the field of flow around the vehicle. (Selvaraju et al., 2015). The wake area's size and the quantity of aerodynamic drag are determined by the flow separation position. The wake is a broad, turbulent, low-pressure area that forms behind an automobile as the air moving over it separates at the back end. This wake plays a part in creating pressure drag (Nath et al., 2021).

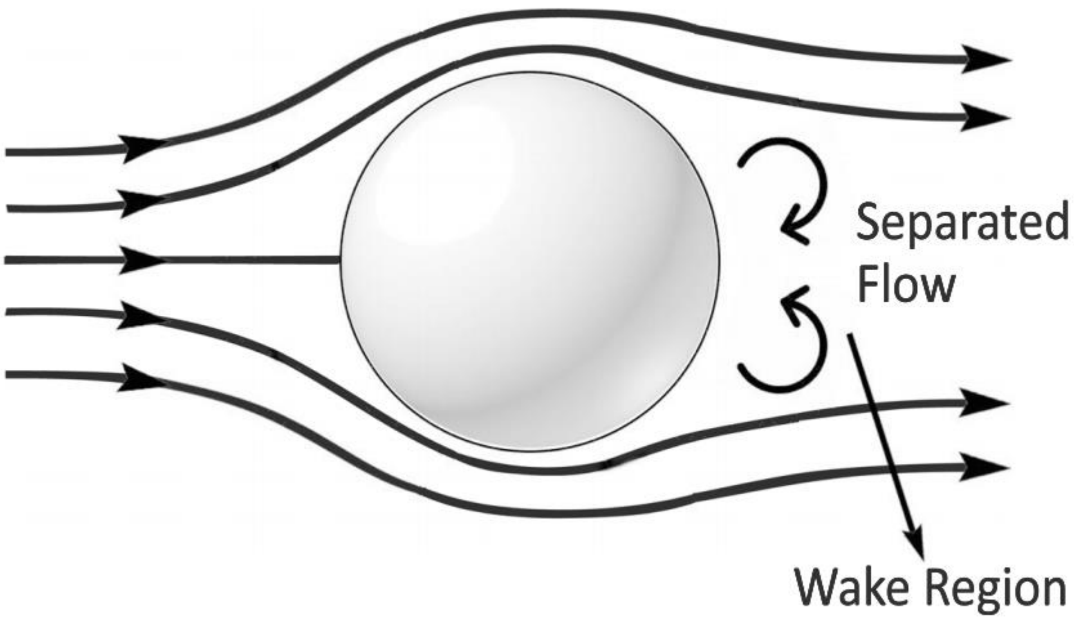

Figure 2.4. Separation of the flow and wake zone formation (Nath et al., 2021)

2.4.2 Reynolds number

The Reynolds number, which is a dimensionless measure, is used to describe the pattern of flow in a fluid system (Nagappan et al., 2023). For the purpose of studying fluid flow, the Reynolds number (Re) is uses. It establishes the laminar or turbulent nature of a fluid flow. Fluids in motion typically follow streamlines. Fluids will travel along laminar flow with smooth streamlines. These streamlines fracture turbulent flow, leading to the fluid's unpredictable movement. The precise numbers that determine whether Re is "big" or "small" are not well defined; instead, they rely on the particular problem at hand. Re values determine the flow's classification: laminar flow occurs when Re is less than 2000, transition flow occurs when Re is between 2000 and 4000, and turbulent flow occurs when Re is greater than 4000 (Ismail et al., 2022). Reynolds Number (Re) is generally represented as:

$$\mathrm{Re} = \frac{\rho VL}{\mu} \tag{2. 3}$$

The fluid's density (ρ) expressed in kg/m3, its velocity (V) expressed in m/s, its length (L) or typical linear dimension expressed in m, and its dynamic viscosity (μ), expressed in kg/ms.

2.4.3 Boundary layer

The boundary layer of aerodynamics was initially established in a German conference by Ludwig Prandtl, an aerodynamic engineer. As a result, the path of flow can be separated into two regions one inside the boundary layer and one outside, allowing aerodynamicists to simplify the fluid flow equations. Viscosity is the primary material in this boundary layer around the vehicle and it significantly contributes to its drag. In the fluid regions outside of this boundary layer, viscosity is disregarded because it has little bearing on the solution. The boundary layer is highly considered in the body form design in order to minimize drag. Designers view the boundary layer as a significant contributor to aerodynamic drag for two reasons. First, the boundary layer increases the body's effective thickness through displacement thickness, which raises pressure drag. The second explanation is skin friction drag, which is brought on by shear pressures at the vehicle's surface (Selvaraju et al., 2015)

2.5 Passive aerodynamic devices

Passive aerodynamic devices for vehicles are integrated into the vehicle's design to enhance its aerodynamic efficiency without necessitating any active driver input or control. Typically, these components are stationary and function in response to the airflow surrounding the vehicle. In efforts to minimize the aerodynamic resistance of commercial vehicles, various external flow-control attachments like side skirts, spoilers, deflectors, flaps, and cab track-trailer gap fairings are employed. Enhancing the aerodynamic effectiveness of these attachments and making design enhancements present potential opportunities in this area.

The utilization of a rear diffuser at high speeds aids in decreasing drag force. It was also observed that the rear diffuser device only dislodges and alters the car's rear flow pattern at speeds above 70 km/h. A base model was created in CATIA and imported into a CFD simulation to assess the impact of rear diffusers of varying lengths. To replicate a passenger car in motion on a real road, the computational domain dimensions were selected to ensure that the aerodynamic force remained unaffected by the domain size (Mohan Kumar & Raj, 2015).

A study was conducted on a sedan car to reduce aerodynamic drag by installing vortex generators at the back of the car on the trunk that were used to delay and prevent flow separation. Computational fluid dynamics (CFD) simulations and physical experiments both show that vortex generators narrow the low-velocity region of the airflow and significantly reduce airflow resistance from the rear window to the trunk. The vortex generators themselves, however, can also produce drag. Vortex generators may be a useful and effective way to reduce drag in cars, according to the study's conclusion (Hasan Ali et al., 2013).

Using a computational fluid dynamics (CFD) numerical model, the aerodynamic properties of a sedan with various rear configurations such as a spoiler and various body profiles—were conducted and the primary goal was to determine how these configurations affected lift (vehicle stability) and drag (fuel consumption) at three different velocities. The study found that installing a spoiler at the right angle of attack changed the lift and drag coefficients, improving vehicle stability and requiring less fuel. The Skoda Superb model was used for the analysis, and drag was decreased from 0.325 to 0.305. (Socrates et al., 2018).

The research investigated how to reduce drag on a car model by using external modifications like passive flow control rear wing spoilers, rear diffuser slices, and vortex generators. It used the SOLIDWORKS 2018 modeler and the computational fluid dynamics (CFD) software ANSYS Fluent 19 to perform a theoretical study using the finite volume method (FVM) to solve the Reynolds-averaged Naiver-Stokes equations (RANS) with a realizable k–epsilon (k–ε) turbulence model. at the inlet velocity of an incompressible car model (V = 10, 20, 30, and 40 m/s). The car had a drag coefficient of 0.34, according to the analysis and the findings showed that vortex generators, rear wing spoilers, and rear underbody diffuser slices could all reduce drag by up to 1.73%, 3.05% and 2.47%, respectively. Combining all of the changes could potentially reduce the drag by up to 3.8% (Saleh & Ali, 2020).

2.6 The Rear Spoiler/Wing

The purpose of a vehicle's rear spoiler is to reduce air movement's negative impacts, like drag and turbulence, while the vehicle is in motion and also to increase the downward force of the vehicle (Das & Riyad, 2017). Due to their significant impact on both safety and performance, wing-type spoilers were initially commonly used in high-performance sports cars and race cars. Today, they are commonly found in passenger cars (Che, 2008). Sedan spoilers work specifically with the separation flow characteristics of these vehicles to reduce drag. Two distinct recirculation areas at the rear window and rear trunk combine to form one enormous recirculation area in sedans. Installing a spoiler stops the sedan's recirculation zone at the rear window. Large vortices arise from a sudden loss of air attached to the vehicle's rear. These vortices will cause a significant pressure drop in the rear end of the car, which will greatly increase pressure drag. It's evident that the car's pressure at the back has increased since the spoiler was installed (Mariaprakasam et al., 2023).

A study was done to find out how passenger cars' drag reduction was affected by splines and rear spoilers. A stock passenger car model with no rear spoiler was built and contrasted with the same model with one installed. In comparison to the base car model, there was a 15% reduction in drag and a 12% reduction in lift when both splines and the rear spoiler were utilized. On the passenger car, this led to a corresponding decrease in lift and drag forces (Shukla & Saxena, 2015).

A recent study evaluated the impact of adding a rear spoiler to a basic sedan car and various forces acting on the car. The NACA 4412 airfoil profile was used at a bunch of different attack angles, from 8 to 14 degrees, using some computer simulation software coupled with a CAD program and then the lift and drag coefficients were estimated at the different angles. The goal was to Figure out which angle provided the best aerodynamic improvements. The simulation used a standard k-epsilon algorithm and second-order equations to model the flow. Based on the results, an 8-degree angle provided the best combo of drag, which went up over 10.34% while lift doubled compared to without spoiler. Specifically, the drag coefficient jumped from 0.29 to 0.322, while the lift coefficient became more negative, dropping from -0.1325 to -0.27. So, in plain terms, the spoiler added both stability and some braking action at this angle (Sakib & Mahmud, 2022).

Three different spoiler shapes were on a Proton Waja sedan car to see which worked best on things like lift and drag. Wind tunnel testing and computer simulations to evaluate each were used to analyze the spoiler's aerodynamics. The computer models matched the wind tunnel data pretty closely, within 5 percent, except for one design and so the simulation method seems solid. Spoiler 1 (NACA 9509), shaped like an upside-down airplane wing performed the best. It created a lot of downforce, pressing the car down into the road. Extra downforce improves high-speed stability. The study suggests inverted airfoil spoilers make good choices for sedan spoilers and reduce lift (Norwazan et al., 2012).

The study examined the effects of rear spoilers on an automobile's aerodynamics using computational fluid dynamics (CFD) techniques. A pre-existing rear spoiler design was modeled with CAD software. The two scenarios that were compared were the car by itself (case 1) and the car with the rear spoiler mounted to the rear deck (case 2). The simulation was done using CFD software (ANSYS Fluent 15.0). The rear spoiler was designed to be a Selig 1223 Aerofoil with a 1.7-meter span, 0.20-meter chord, 11.92% camber, 3.071% chord thickness, and a 10-degree angle of attack. The coefficient of drag (C_d) for case 1 (vehicle only) was 0.001, while for case 2 (vehicle + spoiler), it was 0.0045, according to the convergence history plots. Likewise, case 1 coefficient of lift (C_l) was 0.0005, while case 2 was -0.006, signifying negative lift (or downforce) (Ipilakyaa et al., 2018).

Research has been done to investigate how adding a rear-end spoiler affects a vehicle's aerodynamics, with a specific emphasis on the modifications that result from doing so. and looks into the ideal rear spoiler height in relation to the rear trunk at a constant high speed and angle of attack. The study uses computational fluid dynamics (CFD) to assess the effects of employing two symmetric and one cambered type NACA aerofoils as rear spoilers in order to arrive at these conclusions. The model of a BMW 3 Series automobile used in the study was made in SOLIDWORKS 19 and imported into ANSYS Fluent (2020R2). The study finds that the best height for the spoiler to be placed on the rear trunk is 0.4 times the height between the rear body and the upper surface of the vehicle body. This maximizes the generation of downforce. Among the three types of NACA profiles analyzed, NACA 0012 generates the most downforce when used as a rear spoiler in a car, outperforming NACA 0018 and NACA 2412 (Islam & Inam, 2022).

Based on the Honda Accord 8th generation studied by various aerodynamic configurations, such as different wing shapes, were explored to enhance the car's braking performance. The car body and air foils were designed using SOLIDWORKS software. The research involved analyzing the aerodynamic coefficient, force and airflow over the car body with the rear wing at different angles through CFD analysis and wind tunnel testing. The effects of three distinct airfoils (NACA 2414, 4414, and 6412) on the vehicle's stopping distance were assessed at two different angles of attack. The lowest angle of attack is 1 degree and the maximum angle of attack is 48 degrees. Testing at a 48-degree angle resulted in the largest reduction in braking distance (Ramar et al., 2020).

2.7 Downforce

This is the force that moves a vehicle into the ground. When air flows over an automobile, it creates downforce, or a terrible lift. The purpose of an airplane's wing is to raise the craft off the ground. That's considered a bad thing when it comes to race cars. The car is shaped to allow air to be forced up and down its body, which presses the car down and aids in keeping it on track. Install devices like as splitters, wings, and aero foils to help the car gain more grip while consuming less power in relation to speed. Additionally, as speed increases, more energy is produced, enhancing the ability to hold on. The grip of the tires is nearly equal to the working force on the floor or the friction between the the tread of the tire and road surface; traction can be increased by applying additional force to the ground or lifting the weight downward. Therefore, this negative lift allows the wheels to transmit more power without spinning at maximum speed (Jadhav et al., 2021). When an airfoil is positioned upside down, this is generates downforce (Sripathi, 2017). Figure 2.5 shows the difference in lift and downforce produced by an airfoil.

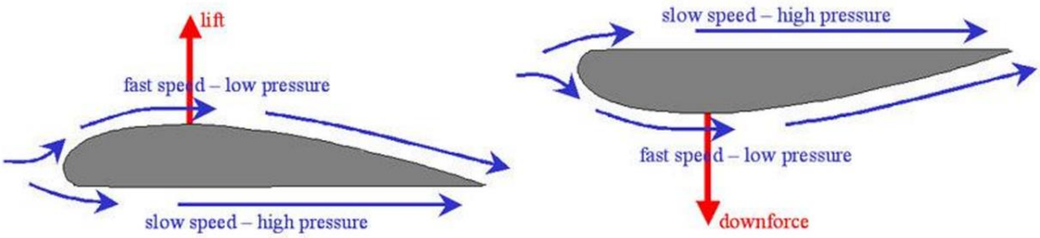

Figure 2.5. The difference in lift and downforce produced by an airfoil (Sripathi, 2017)

2.8 Active aerodynamic control

The term active aerodynamics describes the use of movable or adjustable aerodynamic devices on a car that can be adjusted in terms of shape or location to enhance handling, stability, comfort and braking efficiency. Many experts have carefully researched and developed this technology to improve the performance of road vehicles, especially those meant for high speeds (Gao et al., 2021).

The study used computational fluid dynamics (CFD) simulations to investigate the performance of a sedan with a rear diffuser under different driving scenarios. It investigated how the diffuser's height and angle affected the car's aerodynamics in an effort to reduce drag and boost fuel economy. The simulations were conducted using a detached eddy simulation turbulence model and the commercial solver ANSYS Fluent. It covered a range of driving conditions, including different speeds, wheel rotation rates, and ground clearance. The results showed that the rear diffuser of the sedan effectively reduced its aerodynamic drag coefficient, increasing fuel efficiency (Kang et al., 2012).

Numerous aerodynamic setups can be used to improve the braking ability of a sports vehicle. It analyzes the aerodynamic force coefficients and flow characteristics of a Targa top car body using CFD calculations and data from wind tunnels. This study examines the effects of applying an air brake to a vehicle's rear wing at both low and high angles of attack. The findings indicate that lowering the lift coefficient and increasing the drag coefficient can shorten the stopping distance, depending on the speed and driving circumstances of the vehicle. This suggests that using active aerodynamics when braking can increase driving safety (Kurec et al., 2019).

2.9 Braking distance

The distance that a car covers while braking and stopping completely is referred to as the braking distance. Several factors come into play when it comes to the braking distance, including road incline, tire pressure tread depth, road grip capability, vehicle speed, tire traction drivers braking technique and the condition of the vehicle’s braking system (Poul Greibe, 2007). To make sure that roads are safe, it's important to consider the braking distance, as part of the stopping distance. The stopping distance consists of two components: the reaction distance and the braking distance. Several factors, such, as driver attentiveness, visibility and awareness can influence the reaction distance (Tang et al., 2017).

2.10 Governing Equations

Modern computational fluid dynamics (CFD) is based on the Navier-Stokes model, which is also widely used in simulations of blood flow in arteries, ocean currents, aerodynamics, and weather forecasting. The behavior of fluids and gases can be mathematically explained by applying a system of formulas called the Navier-Stokes equations. The basic governing equations for fluid motion are known as the Navier-Stokes equations. These consist of the mass, momentum, and energy conservation principles (Zharfan et al., 2023). These equations make it possible to calculate and analyze the aerodynamics of an automobile or any other fluid flow when they are paired with the proper boundary conditions and numerically solved via CFD techniques (Zafaruddin et al., 2023).

2.10.1 Mass Conservation Equation

According to the mass conservation principle, a fluid's mass doesn't change over time. The mass flow over a fluid's surface is equal to the mass change within the fluid's volume, the equation is shown below.

$$\frac{\partial \rho}{\partial \mathrm{t}} + \nabla \cdot (\rho \mathrm{v}) = 0 \qquad (2.\ 4)$$

P : Fluid density , ρ : Fluid velocity vector , ∇ : Divergence operator , t : time

The formula states that the density flowing into or out of a volume equals the rate of density change over time. The time derivative of the density is on the left, while the net mass flow of the volume is on the right. With zero net mass flow, mass is conserved. The mass of the control volume needs to stay constant in order for this equation to hold (Zharfan et al., 2023).

2.10.2 Momentum Conservation Equation

According to the momentum conservation principle, the total momentum of a fluid and the things in its immediate vicinity don't change. The momentum conservation equation relates the force applied to a fluid volume and its velocity. It basically says that the net force acting on the fluid volume equals the momentum change rate of that volume. The following formula can be used to express it.

$$\partial \frac{(\rho v)}{\partial t} + \nabla \cdot (\rho v v) = -\nabla p + \nabla \cdot \tau + \rho f \quad (2.5)$$

ρ : Fluid density u: Fluid velocity vector t : Time

p : Fluid pressure

τ : Viscous stress tensor

f : Force vector (such as gravity)

∇ : Divergence operator

The forces operating on the fluid to cause that change in momentum are specified on the right side of the equation, whereas the left side of the equation shows the rate at which momentum changes inside a volume over time. According to the equation, the rate at which momentum changes inside a control volume is equal to the net force acting on it. To represent this, use the equal sign. The pressure force, viscous force, and any other body forces acting on the fluid make up the total force, also referred to as the net force. This vector equation describes the flow of a fluid in three dimensions. It can be applied to both laminar and turbulent flows without modification (Zharfan et al., 2023).

2.10.3 Energy conservation equation

The conservation of all energy, including kinetic, potential, and internal energy, is taken into consideration by the energy equation. The terms on the right-hand side reflect the work performed by pressure (ΔP · v), heat conduction (∇ · (kΔT)), and any heat sources or sinks (Q), whereas the left-hand side represents the rate of change of energy (Zafaruddin et al., 2023).

$$\partial \frac{(\rho E)}{\partial t} + \nabla \cdot (\rho \mathrm{E v}) = -\mathrm{P}\nabla \cdot \mathrm{v} + \nabla \cdot (\mathrm{k}\nabla \mathrm{T}) + \mathrm{Q} \quad (2.6)$$

2.11 Turbulence models

In computational fluid dynamics (CFD), turbulent flows are simulated through the use using turbulence models (Leok et al., 2023). In a fluid field, turbulence is an unstable flow field that manifests as uneven motion and three-dimensional velocity. As with most flows in industrial equipment and surroundings, turbulent flows are found in nature and have significant uses in engineering. Turbulent flows happen at large Reynolds numbers and are always dissipative. Various numerical techniques, including the Reynolds-Averaged Navier-Stokes (RANS) model, the Large Eddy Simulation (LES) model, the Direct-Numerical Simulation (DNS) model, and others, have been widely employed in the last three decades to numerically analyze turbulent flow and other flow issues. The most precise method for modeling turbulent flow is DNS, which solves the Navier-Stokes equations in order to seek a comprehensive three-dimensional resolution of all the turbulent scales in time and space. Unfortunately, DNS can only be applied to low Reynolds number flows over basic geometry at this time and is quite expensive. Only the large-scale motions of turbulent flow, or big eddies, were resolved by LES. Although the model is less expensive than DNS, most real-world applications still require too much computer power and effort. The RANS model is an alternate method for simulating turbulent flow. In RANS, every turbulent length scale is modeled. Because of its low computing requirements and affordability, it has been the core of the current CFD method for simulating turbulent flow for the past few decades (Yusuf et al., 2020).

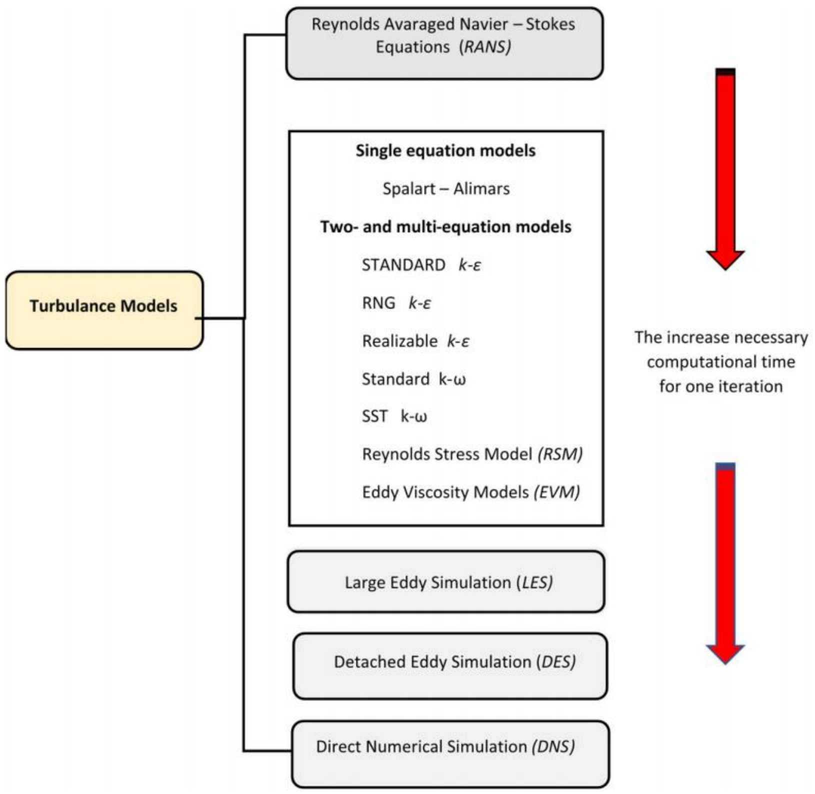

Figure 2.6. Classification of turbulence models (Jaszczur & Młynarczykowska, 2020)

2.11.1 RANS Turbulence Model

Due to it is less expensive to compute than high-fidelity (Hi-Fi) simulations, Reynolds-averaged Navier-Stokes (RANS) is still the primary method used in the majority of industrial purposes (Zhao et al., 2020). The input of turbulent motion modifies the flow's temperature, pressure, velocity, and even density (if the flow is compressible) (Yusuf et al., 2020). While they are not very good at accurately predicting flow in separated zones, attached flow can be predicted with good accuracy using this method. Consequently, these approaches only solve a portion of the important turbulence scale (Al-Saadi, 2019). In the 1960s, the first "eddy viscosity" model for turbulent viscosity was developed; it is classified as algebraic (Baldwin & Lomax, 1978), containing one equation(Spalart & Allmaras, 1992) and two-equation models Based on the correlation between the local values of turbulent viscosity (V), turbulent dissipation (ε), and turbulent kinetic energy (k), two-equation models were developed (Jones & Launder, 1972).

The spalart–allmaras model

A single transport equation can be used to solve for a variable having viscosity-like qualities in the Reynolds-averaged Navier-Stokes model, the Spalart-Allmaras model. The model is both effective and computationally affordable, and it can account for all sources of turbulence generation and destruction. The Spalart-Allmaras model was used to analyze two- and three-dimensional instances in software with significant parallelism (Bourgoin et al., 2021). The model was developed and improved for flows via wings and airfoils. This method has the advantage of yielding highly desirable answers for adverse pressure gradients and boundary layers with only one more equation to solve. One limitation of this approach is that it is only applicable to flow fields when the transition is caused by a separate flow. It is not suitable for predicting a natural transition within an attached boundary layer (Yusuf et al., 2020).

$$\frac{\partial}{\partial t}(\rho\tilde{v}) + \frac{\partial}{\partial x_i}(\rho\tilde{v}u_i) = G_v + \frac{1}{\sigma_{\tilde{v}}}\left[\frac{\partial}{\partial x_i}\left\{(\mu + \rho\tilde{v})\frac{\partial\tilde{v}}{\partial x_i}\right\} + C_{b2}\rho\left(\frac{\partial\tilde{v}}{\partial x_i}\right)^2\right] - Y_v + S_{\tilde{v}} \quad (2.7)$$

Where Gv denotes the formation of turbulent viscosity, Y_v denotes the lowering of turbulent viscosity due to blockage and viscosity damping, $\sigma_{\tilde{v}}$ and C_{b2} are constants parameter, v is the molecular kinematics viscosity and $S_{\tilde{v}}$ is user user-defined terms.

The k–ε Turbulence Models

The most popular and frequently applied of the several two-equation turbulence models is the k-ε model. In computational fluid dynamics (CFD), the k-epsilon turbulence model is a two-equation model that is commonly used to approximate mean flow characteristics for turbulent flow situations. It provides a general explanation of turbulence through the use of two transport equations, also known as partial differential equations, or PDEs. The model is based on the theory that the two most important variables for representing turbulence are the turbulent kinetic energy (k) and the rate at which it dissipates (ε) (Jones & Launder, 1972). The $k - \varepsilon$ model is preferred when a study involves with free-shear layers and wake field view (Kamal et al., 2021).However, there are certain limitations. For example, distortion or non-local effects are not taken into account. Over time, k-ε models have taken on many different forms, such as the standard k-ε model, the RNG k-ε model, and the realizable k-ε model (Gorman et al., 2021).

Standard k- ε model

The most widely used two-equation turbulence model in computational fluid dynamics (CFD) is the standard k-ε turbulence model. According to the model, the primary parameters determining the behavior of turbulence are the turbulent kinetic energy (k) and its dissipation rate (ε) (Gorman et al., 2021).

$$\frac{\partial}{\partial t}(\rho k) + \frac{\partial}{\partial x_i}(\rho k u_i) = \frac{\partial}{\partial x_j}\left[\left(\mu + \frac{\mu_t}{\sigma_k}\right)\frac{\partial k}{\partial x_j}\right] + G_k + G_b - \rho\varepsilon - Y_M + S_k \quad (2.8)$$

And

$$\frac{\partial}{\partial t}(\rho\varepsilon) + \frac{\partial}{\partial x_i}(\rho\varepsilon u_i) = \frac{\partial}{\partial x_j}[(\mu + \frac{\mu_t}{\sigma_\varepsilon})\frac{\partial \varepsilon}{\partial x_j}] + C_{1\varepsilon}\frac{\varepsilon}{k}(G_k + C_{3\varepsilon}G_b) - C_{2\varepsilon}\rho\frac{\varepsilon^2}{k} + S_\varepsilon \quad (2.9)$$

Where the viscosity of a turbulent (or eddy), $\mu_t = \rho C_\mu \frac{k^2}{\varepsilon}$

G_k represents the kinetic energy generated by turbulence as a result of mean velocity gradients. G_b represents the kinetic energy of turbulence produced by buoyancy.

Realizable k- ε model

A more advanced and feature-rich version of the standard k-ε turbulence model is the realizable k-ε turbulence model. More accurate forecasts for complex flows are intended by the realizable k-ε model, which is based on the Reynolds stress transport equation. The model is called "realizable" because it meets certain mathematical criteria that guarantee the model's practical implementation (Muiruri et al., 2019). With the standard wall function, one may compute the turbulent kinetic energy and its dissipation rate from the wall shear stress, implying that the flow near the wall is in an equilibrium condition. This is a semi-empirical method. Modeling turbulent flows around barriers is a good application for this computationally efficient technology.

$$\frac{\partial}{\partial t}(\rho k) + \frac{\partial}{\partial x_j}(\rho k u_j) = \frac{\partial}{\partial x_j}\left[\left(\mu + \frac{\mu_t}{\sigma_k}\right)\frac{\partial k}{\partial x_j}\right] + G_k + G_b - \rho\epsilon - Y_M + S_k \quad (2.10)$$

And

$$\frac{\partial}{\partial t}(\rho\varepsilon) + \frac{\partial}{\partial x_j}(\rho\varepsilon u_j) = \frac{\partial}{\partial x_j}\left[\left(\mu + \frac{\mu_t}{\sigma_\varepsilon}\right)\frac{\partial \varepsilon}{\partial x_j}\right] + \rho C_1 S_\varepsilon - \rho C_2\frac{\varepsilon^2}{k+\sqrt{v\varepsilon}} + C_{1\varepsilon}\frac{\varepsilon}{k}C_{3\varepsilon}G_b + S_\varepsilon \quad (2.11)$$

RNG k- ε model

The standard k-ε model has been modified to create the RNG k-ε turbulence model. Using the mathematical method known as the RNG approach, one can derive a turbulence model that is similar to the k-ε model. To try to account for the different scales of motion, the production term in the RNG model is changed (Somashekar, 2021).

$$\frac{\partial}{\partial t}(\rho k) + \frac{\partial}{\partial x_i}\&(\rho k u_i) = \frac{\partial}{\partial x_i}\left(\alpha_k \mu_{eff} \frac{\partial k}{\partial x_i}\right) + G_k + G_b - \rho\varepsilon - Y_M + S_k \quad (2.\ 12)$$

And

$$\frac{\partial}{\partial t}(\rho\varepsilon) + \frac{\partial}{\partial x_i}\&(\rho\varepsilon u_i) = \frac{\partial}{\partial x_j}\left(\alpha_\varepsilon \mu_{eff} \frac{\partial \varepsilon}{\partial x_j}\right) + C_{1\varepsilon}\frac{\varepsilon}{k}(G_k + C_{3\varepsilon}G_b) - C_{2\varepsilon}\rho\frac{\varepsilon^2}{k} - R_\varepsilon + S_\varepsilon$$

(2. 13)

The k–ω Turbulence Models

The two-equation k-omega (k-ω) turbulence model is a popular tool in computational fluid dynamics for predicting mean flow characteristics under turbulent flow circumstances. Using two partial differential equations for two variables (k and ω), this two-equation model predicts and simulates turbulence (Somashekar, 2021). The production term of turbulent kinetic energy (k), and the frequency of dissipation (ω), determine the standard k-ω model. The two-equation turbulence model for kinetic energy and dissipation per unit turbulence kinetic energy was first proposed by Kolmogorov in 1941 (Weaver & Mišković, 2021). the $k - \omega$ model is suiTable to provides more accurate solutions in the near wall boundary regions(Kamal et al., 2021). The k-ω model, which replaced the transport equation for ε with a particular rate of turbulence dissipation, ω, was a major advancement in CFD (Gorman et al., 2021). The updated formulas are:

$$\rho\frac{\partial(u_i k)}{\partial x_i} = \rho P_k + \rho P_b - \rho\beta\omega k + \frac{\partial}{\partial x_i}[(\mu + \frac{\mu_t}{\sigma_k})\frac{\partial k}{\partial x_i}] \quad (2.\ 14)$$

And

$$\rho\frac{\partial(u_i \omega)}{\partial x_i} = \frac{\partial}{\partial x_i}\left[\left(\mu + \frac{\mu_t}{\sigma_\omega}\right)\frac{\partial \omega}{\partial x_i}\right] + \frac{\alpha\omega}{k}P_k - \beta\rho\omega^2 \quad (2.\ 15)$$

Applying a turbulent viscosity that is determined by: $\mu_t = \rho\frac{\kappa}{\omega}$

k–ω SST Turbulence Model

k–ω SST Turbulence model was created by Menter and solves the Reynolds stress equations and treats the wall function using some characteristics of the k-ω and k-ε models (Costa et al., 2022).The purpose of the k-ω SST a turbulence model is to employ the k-ω model in the near field because of its robustness, then switch to the k-ε model in the far field because of its efficacy (Weaver & Mišković, 2021).

$$\frac{\partial}{\partial t}(\rho k) + \frac{\partial}{\partial x_i}(\rho k u_i) = \frac{\partial}{\partial x_j}\left(\Gamma_k \frac{\partial k}{\partial x_j}\right) + G_k - Y_k + S_k \tag{2. 16}$$

And

$$\frac{\partial}{\partial t}(\rho \omega) + \frac{\partial}{\partial x_i}(\rho \omega u_i) = \frac{\partial}{\partial x_j}\left(\Gamma_\omega \frac{\partial \omega}{\partial x_j}\right) + G_\omega - Y_\omega + S_\omega \tag{2. 17}$$

Were $\Gamma_k = \mu + \frac{\mu_t}{\sigma_k}$ and $\Gamma_\omega = \mu + \frac{\mu_t}{\sigma_\omega}$

2.11.2 Large Eddy Simulation

Computational fluid dynamics (CFD) uses the Large Eddy Simulation (LES) mathematical model of turbulence. Joseph Smagorinsky first proposed it in 1963 to imitate atmospheric air currents. The main idea behind the technique is to separate large-scale turbulent formations from small-scale structures. Large-scale structures in LES are directly resolved, whilst subgrid-scale models are used to model the small-scale structures (Wilcox, 2006).

2.11.3 Direct numerical simulation

In computational fluid dynamics (CFD), a "direct numerical simulation" (DNS) is a numerical solution of the Navier-Stokes equations that does not require a turbulence model. For this to happen, the full spectrum of spatial and temporal scalar turbulence must be resolved (Wilcox, 2006).

2.12 Computational Fluid Dynamics (CFD)

Computational fluid dynamics is a subfield of fluid dynamics that offers an affordable way to simulate real flows by solving governing equation numerically (Sayma, 2009). The algorithms and numerical techniques are used to solve fluid dynamics problems (Zikanov, 2019). The numerical techniques for estimating solutions to problems involving fluid dynamics and heat transfer are collectively referred to as CFD. It involves applying a computational mesh to split continuous fluids in the real world into discrete sections. The characteristics of the close to interdependent sections are then taken into consideration as each section is handled independently using the fluid flow governing equations. This makes it possible to solve each part simultaneously until the entire flow field's solution is found. Modern computing advancements have made it possible to find solutions, which previously would have taken months to compute by hand, in seconds with just an ordinary desktop or laptop computer, without the significant computational power required (Leary, 2010).

2.13 Review Summary

Aerodynamic forces play a crucial role in determining the performance and safety of vehicles. One of the primary aerodynamic forces that impacts vehicles is drag, which refers to the resistance a vehicle faces while in motion through the air. Which describes the opposition a car encounters when moving through the air. Researchers can improve the vehicle's overall performance and fuel efficiency by improving its design to reduce drag. Lift is another important aerodynamic force that affects a vehicle's handling and stability, particularly at higher speeds. To build cars that are safe to drive and efficient, it is essential to understand and manage these forces. The design of vehicles, particularly their aerodynamic features, has a significant impact on the amount and distribution of aerodynamic forces.

As seen above, passive control devices have been significant in improving passenger car aerodynamics in a number of ways, as demonstrated above. Passive components, which don't rely on power sources are features that are specifically designed to regulate the airflow around a vehicle. By utilizing devices, like vortex generators, diffusers and spoilers it is possible to enhance the performance, fuel efficiency and safety of various objects. These devices play a role in improving a vehicles aerodynamics by optimizing airflow and reducing drag. Moreover, spoilers are particularly effective, in enhancing traction and stability at speeds by disrupting airflow and increasing downward force while minimizing lift. And the other one is active aerodynamic devices, which are mostly used in sport cars. They have movable components that adjust a vehicle's external shape to improve its aerodynamic efficiency. These devices are not applicable to passenger vehicles and there is a lack of research about their effects on passenger vehicles and how the controlling mechanism works.

2.14 Research Gap

Many researchers are focused on analyzing the effect of the aerodynamics of a passenger car by using computational fluid dynamics (CFD) with passive add-on devices. Their focus is either to reduce fuel consumption or improve stability. There is limited literature on the topic of reducing braking distance through the use of aerodynamic braking and active aerodynamics to achieve multiple goals, such as stability during higher acceleration and reducing braking distance during higher deceleration. Additionally, there is no development of automatic control mechanisms for adjustable spoilers on passenger cars.

CHAPTER THREE

MATERIALS AND METHODOLOGY

This chapter explains the materials used in this thesis and the methodology followed throughout the study.

3.1 Materials

The materials used to develop the prototype of the adjustable rear wing-spoiler system are shown in Table 3.1.

Table 3.1. Materials and specification

No	Item	Unit	Specification	Quantity
1	Arduino Uno microcontroller	Pcs	ATmega328P	1
2	Solid State Relay (SSR)	Pcs	5 V	1
3	Solenoid	Pcs	12 V	1
4	Breadboard	Pcs	Mini	1
5	Brake switch	Pcs	12 V	1
6	LM393 Infrared Speed Sensor	Pcs	LM393	1
7	16×2 LCD	Pcs	16×2	1
8	DC motor	Pcs	12 V	1
9	Mini DC motor PWM Speed Controller	pcs	supply voltage: 1.8V-35v DC	1
10	Jumper wire	Pcs		------

3.1.1 Arduino UNO Microcontroller

The Arduino UNO microcontroller is an open-source device that is simple to program, erase, and reprogrammed at any time. It was developed in 2005 to provide a simple and inexpensive way for professionals, students, and hobbyists to create devices that use sensors and actuators to interact with their environment. Building and programming electronic devices is possible with this open-source computing platform, which is built use basic microcontroller boards. Like other microcontrollers, it can also be used as a minicomputer, by receiving inputs and controlling outputs for various electronic devices (Louis, 2016). There is no need for extra hardware for the Arduino to upload new code to the board. You can simply use a USB cable. The Arduino software utilizes a simplified version of C++ (Stroustrup, 2013).

Elements of an Arduino board can be classified into two categories:

• Hardware

• Software

Hardware

The Arduino Development Board is made up of various components that work together to enable its operation. Below are some of the key component blocks that contribute to its functionality:

Microcontroller: This is the heart of the development board, functioning as a small computer capable of both receiving and transmitting information and instructions to the peripheral devices it is linked to. The specific microcontroller utilized varies between different boards and comes with its own set of specifications.

External Power Supply: This power supply is utilized to provide a consistent voltage of 9- 12 volts to the Arduino development board. The USB plug is a crucial port for uploading programs to the microcontroller using a USB cable and also supplies regulated power of 5V to the Arduino board when an external power supply is not available.

Internal Programmer: The software code that has been created can be transferred to the microcontroller using the USB port, eliminating the need for an external programmer.

Reset button: This board contains a button that is used to reset the Arduino microcontroller.

Analog Pins: There are typically several analog input pins labeled A0 to A7. These pins are utilized for analog input and output. The number of analog pins can differ between different boards.

Digital I/O Pins: There are typically 2 to 16 digital input pins available for digital input/output on various boards, with the number of pins varying between different boards.

Power and GND Pins: The development board has pins that supply 3.3 volts, 5 volts, and ground.

Software

The code created for Arduino is referred to as a sketch. The software used to create these sketches for an Arduino is commonly called the Arduino IDE. This IDE includes the following components:

Text editor: This is the place where you can write simplified code using a simplified form of the C++ programming language.

Message area: It shows an error message and provides information about saving and exporting the code.

Text: the console shows the text output from the Arduino environment, which includes error messages and additional information.

Console Toolbar: This toolbar includes different buttons such as Verify, Upload, New, Open, Save, and Serial Monitor. At the bottom right corner of the window, the development board and the currently used serial port are displayed. Figures 3.1 and 2.2, show labelled arduino board and lablled arduino IDEs, respectively.

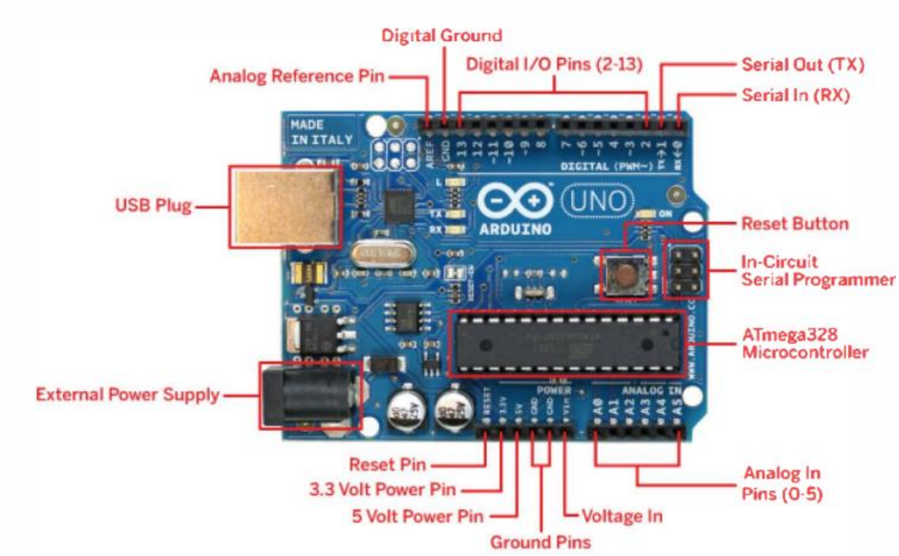

Figure 3.1. Labelled Arduino Board (Louis, 2016)

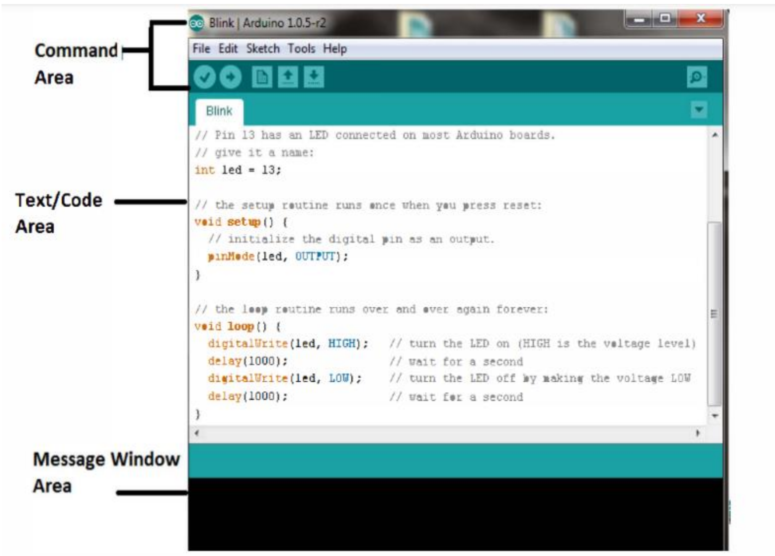

Figure 3.2. Labelled Arduino IDE (Louis, 2016)

3.1.2 Solid State Relay (SSR)

A solid state relay (SSR) is an electrical Switch that, different from an electromechanical relay, has no moving parts. The input and output components of an SSR are separated by an insulator. SSR can avoid splash and poor connection caused by porous contactors, which are common in conventional relay systems. SSR for work necessitates relatively low energy control, or vice versa. This control energy is significantly lower than the output power controlled by the relay at full load (power gain) (Hasibuan et al., 2021). When compared to electro-mechanical relays (EMRs), solid state relays (SSRs) perform the same circuit function. However, solid state relays have several advantages over EMRs, such as faster switching, no need to change the output on-state resistor, better anti-jamming capabilities, no generation of electrical noise or magnetic fields, longer electrical life expectancy, and higher reliability (Zhang et al., 2011).

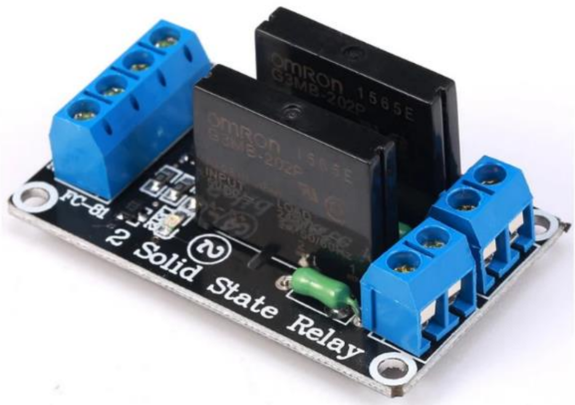

Figure 3.3. Solid State Relay (SSR) (Hasibuan et al., 2021)

3.1.3 LM393 Infrared Speed Sensor

The infrared LED and phototransistor that make up the speed sensor (mode: LM393 IC) are mounted on a tiny printed circuit board. An infrared (IR) beam is released by the LED when it is turned on. In the event that the blocker causes an IR beam disruption, the phototransistor will sense it and generate an electrical pulse. The blocker's RPM and pulses per second are directly correlated. The voltage range in which the speed sensor operates is 3.3 to 5 V. The output signal is low when the sensor detects a pulse and high otherwise. The DO output interface can be directly connected to a microcontroller IO port, if there is a block detection sensor, such as the speed of the motor encoder(Elwakeel et al., 2023). The LM393 Infrared Speed Sensor shown in Figure 3.4.

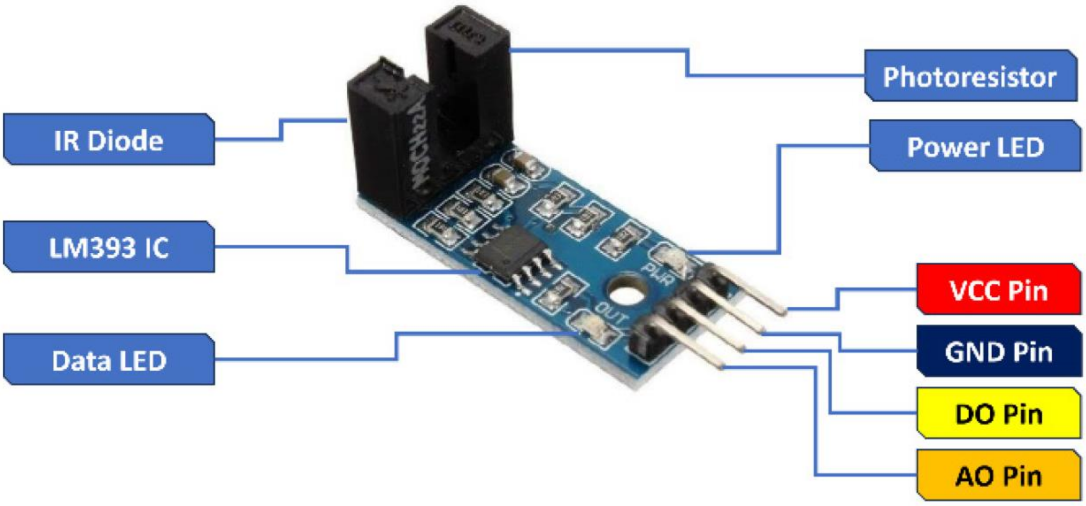

Figure 3.4. LM393 Infrared Speed Sensor (Elwakeel et al., 2023)

3.1.4 16×2 LCD

LCD (Liquid Crystal Display) screens are digital display modules with numerous applications in automation systems. A 16x2 LCD display uses two lines, each of which can hold 16 characters. The pixel matrix size used in this LCD to display each character is 5x7 (Parab & Prajapati, 2019). Operating voltage is between 4.7 and 5.3 volts, and current consumption is one milliamp. Both letters and numbers can be seen on the display. It can use an internal or external light source and runs in both four-bit and eight-bit modes. Its response time is between 100 and 300 milliseconds, and its temperature range is restricted to 0 to 60 degrees Celsius. The display's lifespan is gradually extending beyond 10,000+ hours, and the illumination source determines the color it generates. The 16×2 LCD is shown in Figure 3.5.

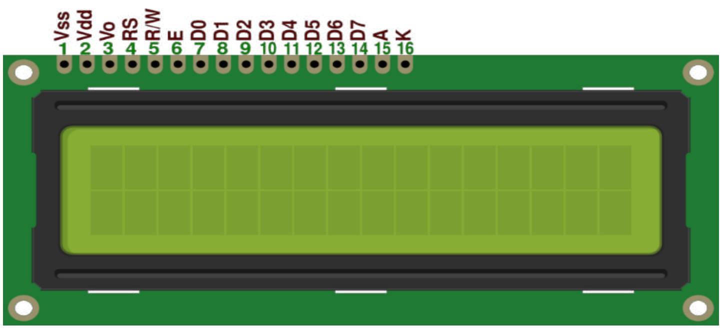

Figure 3.5. 16×2 LCD (Parab & Prajapati, 2019)

3.1.5 Solenoid

A solenoid is a kind of electromagnet that, when an electric current is passed through it, produces a magnetic field. They are usually composed of a coil of wire. Solenoids are frequently used to control the motion of mechanical components and are found in a wide range of applications, such as switches, relays and valves. In electronic locks, they are also frequently utilized to regulate the locking mechanism by producing a magnetic field that either attracts or repels a metal object. The solenoid is shown in Figure 3.6.

Figure 3.6. Solenoid (Samarasinghe, 2016)

3.1.6 Breadboard

The breadboard, also known as a plug board, features sets of small sockets arranged on a 0.1-inch grid. These sockets allow for manual inserting of component connections and tinned copper wire (TCW) linkages. The board has interconnected rows of contacts on both sides of its center line, where integrated circuits (ICs) are placed, providing multiple contacts for each IC pin. Long rows of common contacts on each side of the board are used for power supplies (Bates, 2011). With the rows and columns' numbers and letters printed on them (Nayyar & Puri, 2017). The breadboard shown in Figure 3.7.

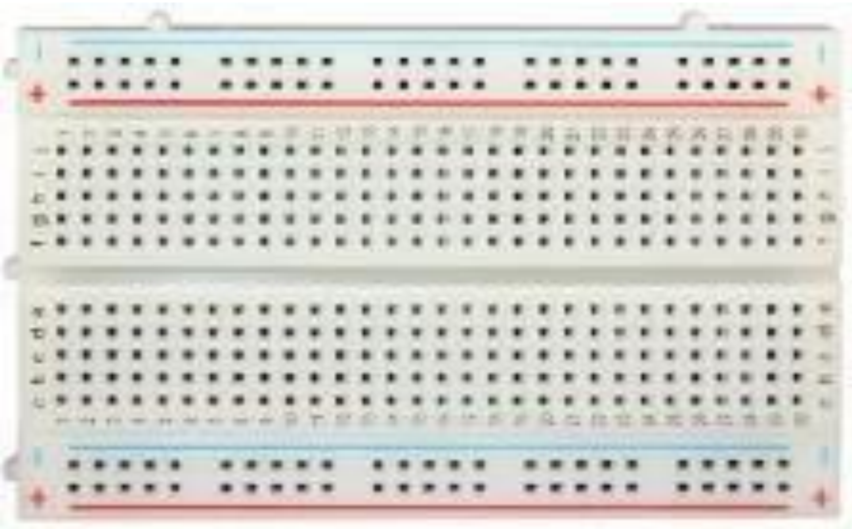

Figure 3.7. Breadboard (Nayyar & Puri, 2017)

3.1.7 Brake light switch

A brake light switch is a electrical switch that is connected to the brake pedal mechanism. When the brake pedal is pressed, the switch is activated and completes a circuit, turning on the brake lights at the rear of the vehicle. The brake light switch shown in Figure 3.8.

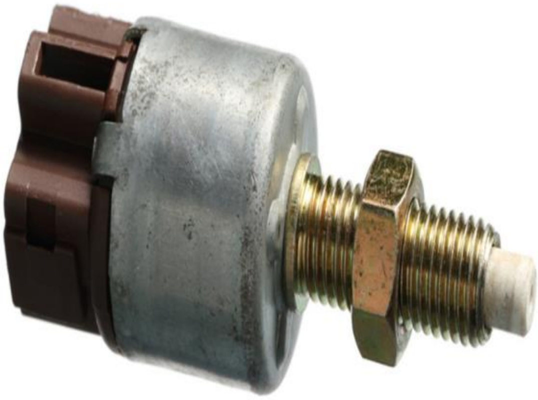

Figure 3.8. Brake light switch

3.1.8 Mini DC motor PWM Speed Controller

A small DC motor A PWM speed controller is a small device that uses pulse-width modulation (PWM) to control the speed of a DC motor. PWM is a method that quickly turns the motor's power on and off. The average power supplied to the motor is determined by the duty cycle of the PWM signal, which in turn regulates the motor's speed.Most of these controllers are incredibly compact and simple to operate. To change the motor's speed, they usually feature a knob or potentiometer that you may spin. Additionally, certain controllers could have an on/off switch. The brake light switch shown in Figure 3.9.

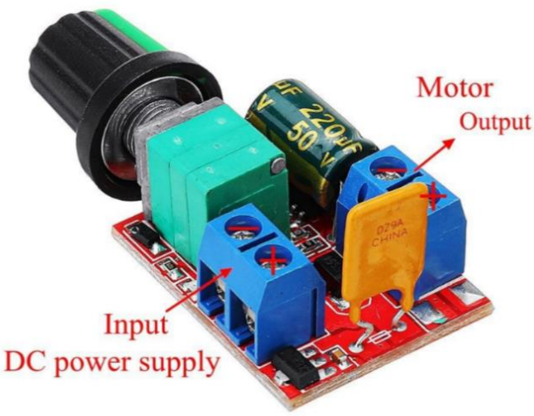

Figure 3.9. Mini DC motor PWM Speed Controller

3.1.9 12-volt DC motor

DC motors are rotary motors that have the ability to convert electrical energy into mechanical energy. They are advantageous in many applications due to their affordability, reliability, performance, operator friendliness and effectiveness. Because of its precise controllable torque across a broad range and its speed, DC motors are widely used as positioning devices (Haidar et al., 2011). The 12 volt DC motor shown in Figure 3.10.

Figure 3.10. 12-volt DC motor (Hasibuan et al., 2021)

3.1.10 Jumper wire

A jumper wire, also called jump wire or DuPont A wire is a conductor of electricity or a group of connected wires in a cable that has a connectors or pin on each end. It is typically used to connect the parts of a test circuit, prototype or breadboard together, either internally or with other component without using solder. The jumper wire shown in Figure 3.11.

Figure 3.11. Jumper wire (Chidhambaram et al., 2019)

3.2 Methodology

The work procedures outlined in this section, and the techniques for data collecting and analysis are all included in the methodology of this study.

3.2.1 Methodology flowchart

Figure 3.12 shows the methodology flowchart that was used as guidance to execute this study. It begins by identifying the problem and finding the research gap through a literature review. The baseline model car and spoiler were designed using SOLIDWORKS software. The baseline model and the baseline model with different angles of spoiler inclinations (at 0, 10, 20, 30, 40, 50, and 90 angles) were analyzed using ANSYS Fluent software at different speeds (80, 120, and 160 km/h). The CFD software allows for the simulation of the flow of air around the car and spoiler. This analysis was used to determine the aerodynamic forces acting on the car, such as drag and lift. After collecting and analyzing the results, the appropriate angle for the spoiler to achieve optimal performance in both high-speed acceleration and deceleration was determined. After that, prototypes were constructed to demonstrate the adjustable spoiler's functionality. The prototype had both software and hardware components. The software component is the code that runs on the hardware. The process of developing software involved writing a program, designing a circuit, and simulating, on the hardware components (including an Arduino UNO board, solid state relay, solenoid, breadboard, brake switch, infrared speed sensor, LCD, DC motor circuit wire and DC motor A PWM speed controller) that were assembled to create this prototype. Following that, testing and verification took place. Documentation was the last step, following discussion and conclusion.

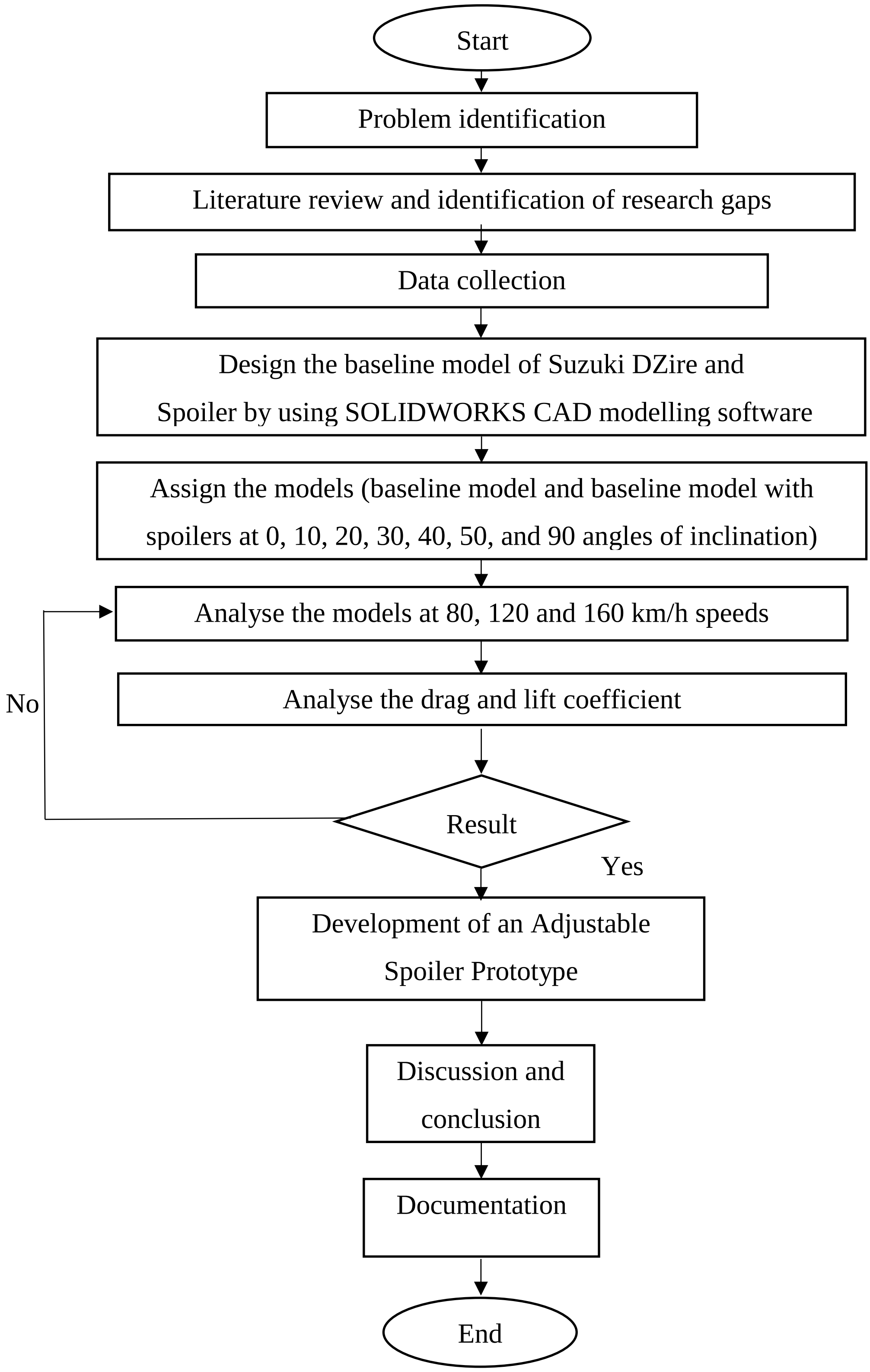

Figure 3.12. Methodology flowchart

3.2.2 Design of Geometric models

3.2.2.1 Design of the baseline model

For this work, a vehicle model of the Suzuki Dzire was used. The model is an exact replica of the passenger car in full scale. The model was built without side view mirrors, with an enclosed wheel well, a smooth underbody, and cooling openings. SOLIDWORKS 2023 was used to develop the model. The model of the car having 3995 mm long, 1735 mm wide, 2450 Wheelbase and height of 1515 mm is shown in Table 3.2.

Table 3.2.Basic dimension of Suzuki Dzire

Dimensions	in mm
Length	3995
Width	1735
Height	1515
Wheelbase	2450

The vehicle model chosen as the standard and the 3D CAD model of the baseline model are shown on Figure 3.13 and Figure 3.14.

Figure 3.13. Selected Passenger car (Suzuki Dzire)

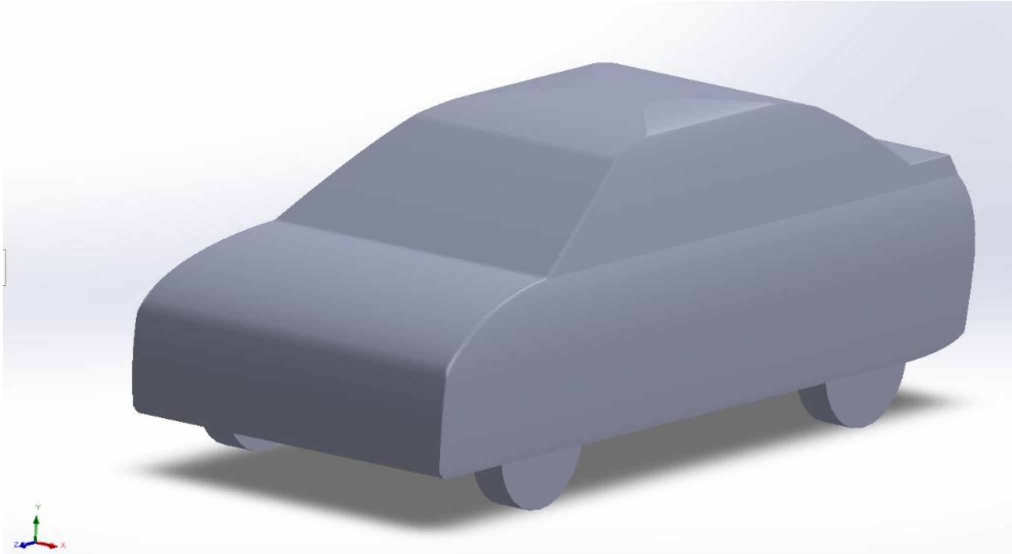

Figure 3.14. 3D CAD model of the baseline model

3.2.2.2 Design of rear wing type spoiler

The main purpose of an automobile's rear end wing type spoiler is to improve stability and grip on the road by reducing lift force and increase the down force. Increased stability resulted from this rear-positioned component creating a high-pressure area to replace the low-pressure area on the trunk. The NACA 0012 half section was used to choose the spoiler airfoil shape. The four-digit number assigned to NACA airfoils is unique. NACA airfoils are designated by a four-digit number. The first digit indicates the camber of the airfoil, which is the difference in the height of the upper and lower surfaces. The second and third digits indicate the maximum thickness of the airfoil, and the fourth digit indicates the location of the maximum thickness. Half-Section: This suggests that only one side of the airfoil will be used. The cord length and width of a spoiler are determined by the type of spoiler, the vehicle it is being installed on, and the desired effect. The vertical parts of the rear wing that are joined to the main wing are called endplates. Endplates reduce drag and turbulence by regulating airflow across the rear wing. The endplates also help to keep airflow from fleeing the wing's edges, which would reduce the wing's efficiency. The NACA 0012 airfoil was selected, and the coordinates were imported into SolidWorks 2023 for modeling. The modeled spoiler's chord length was 250 mm with a width of 1400 mm. The coordinates of the NACA 0012 airfoil with a 250-cord length are shown in Table 3.3.

Table 3.3. Coordinates of NACA 0012 airfoil

X(mm)	Y(mm)
250	0.315
237.5	2.0175

225	3.62
212.5	5.1325
200	6.5575
187.5	7.9
175	9.16
162.5	10.3325
150	11.4075
137.5	12.38
125	13.235
112.25	13.97
99.75	14.52
87.25	14.8775
74.75	15.005
68.75	15.12
62.5	15.21
56.25	15.25
50	15.2175
43.75	15.0825
37.5	14.81
31.25	14.35
25	13.635
20	12.8025
15	11.6375
12.5	10.8775
10	9.955
7.5	8.805
5	7.3125
2.5	5.185
1.25	3.595
0	0
1.25	-3.595
2.5	-5.185
5	-7.3125
7.5	-8.805
10	-9.955
12.5	-10.8775
15	-11.6375
20	-12.8025
25	-13.635
31.25	-14.35
37.5	-14.81
43.75	-15.0825
50	-15.2175
56.25	-15.25
62.5	-15.21
68.75	-15.12
74.75	-15.005
87.25	-14.8775
99.75	-14.52

112.25	-13.97
125	-13.235
137.5	-12.38
150	-11.4075
162.5	-10.3325
175	-9.16
187.5	-7.9
200	-6.5575
212.5	-5.1325
225	-3.62
237.5	-2.0175
250	-0.315

The 3D model of the half section NACA 0012 airfoil and endplates are shown on Figure 3.15

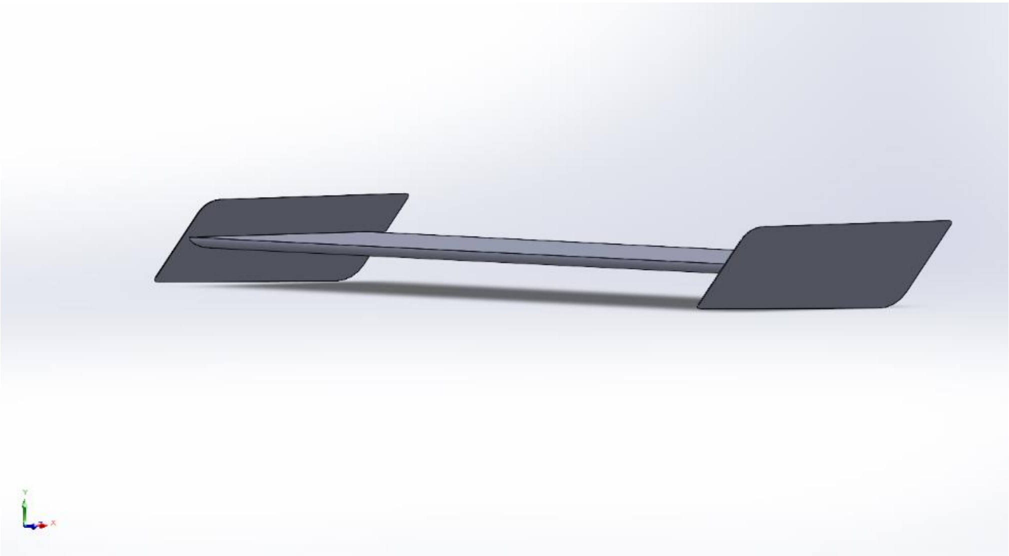

Figure 3.15. 3D model of the half section NACA 0012 airfoil and endplates

3.2.2.3 Design of Baseline model with a rear wing type spoiler

This study uses wing-type rear-end spoilers in multiple configurations. The spoilers are mounted on the vehicle's (truck) rear side at a height of 200 mm. Each configuration baseline model (with spoilers at 0, 10, 20, 30, 40, 50, and 90 angles of inclination) is assigned model one, model two, model three, model four, model five, model six and model seven, respectively. The model one (baseline model with spoiler inclined at a 0-degree angle) is shown on Figure 3.16.

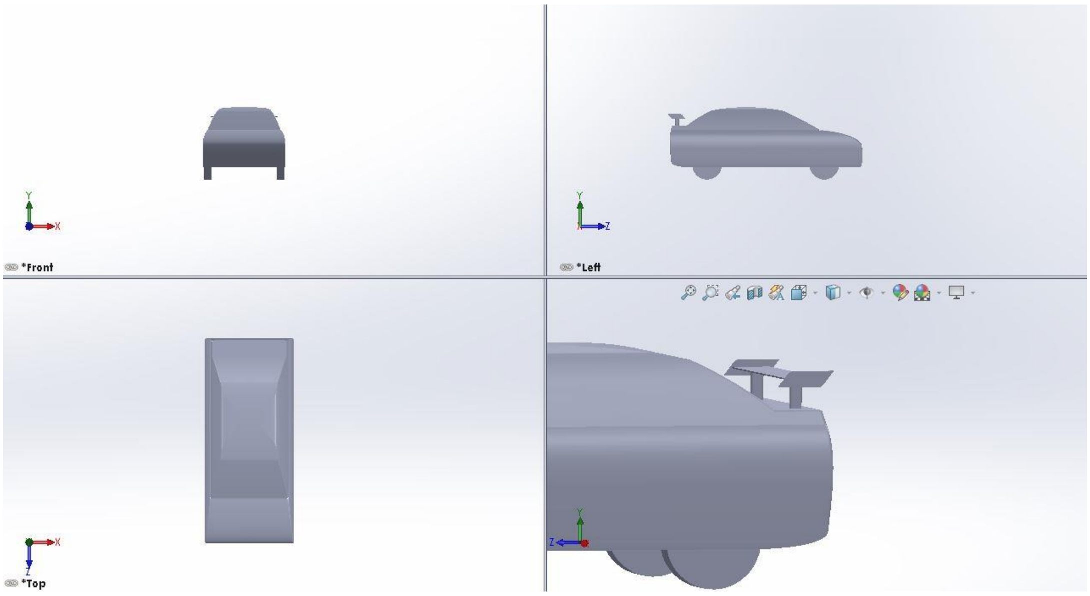

Figure 3.16. Model one (baseline model with spoiler inclined at a 0-degree angle)

The model two (baseline model with spoiler inclined at a 10-degree angle) is shown on Figure 3.17.

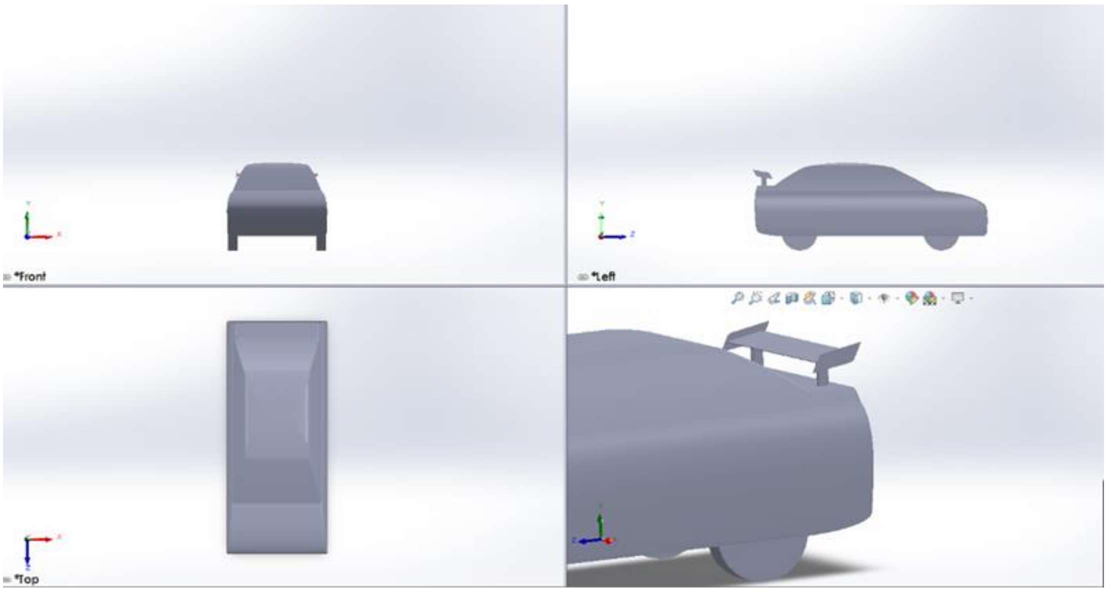

Figure 3.17. Model two (baseline model with spoiler inclined at a 10-degree angle)

The model three (baseline model with spoiler inclined at a 20-degree angle) is shown on Figure 3.18.

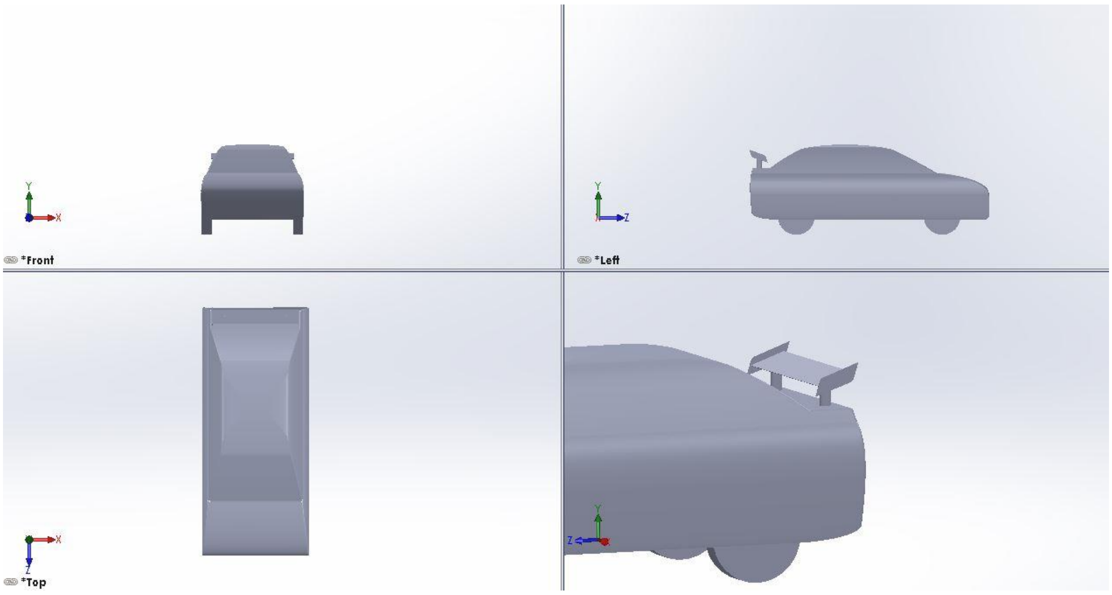

Figure 3.18. Model three (baseline model with spoiler inclined at a 20-degree angle)

The model four (baseline model with spoiler inclined at a 30-degree angle) is shown on Figure 3.19.

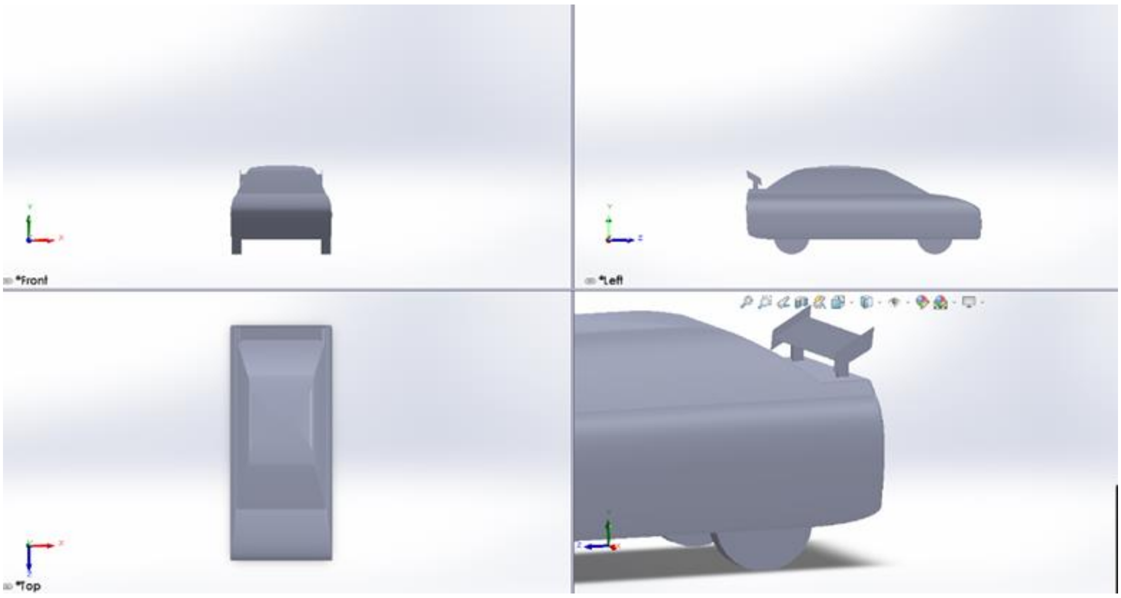

Figure 3.19. Model four (baseline model with spoiler inclined at a 30-degree angle)

The model five (baseline model with spoiler inclined at a 40-degree angle) is shown on Figure 3.20.

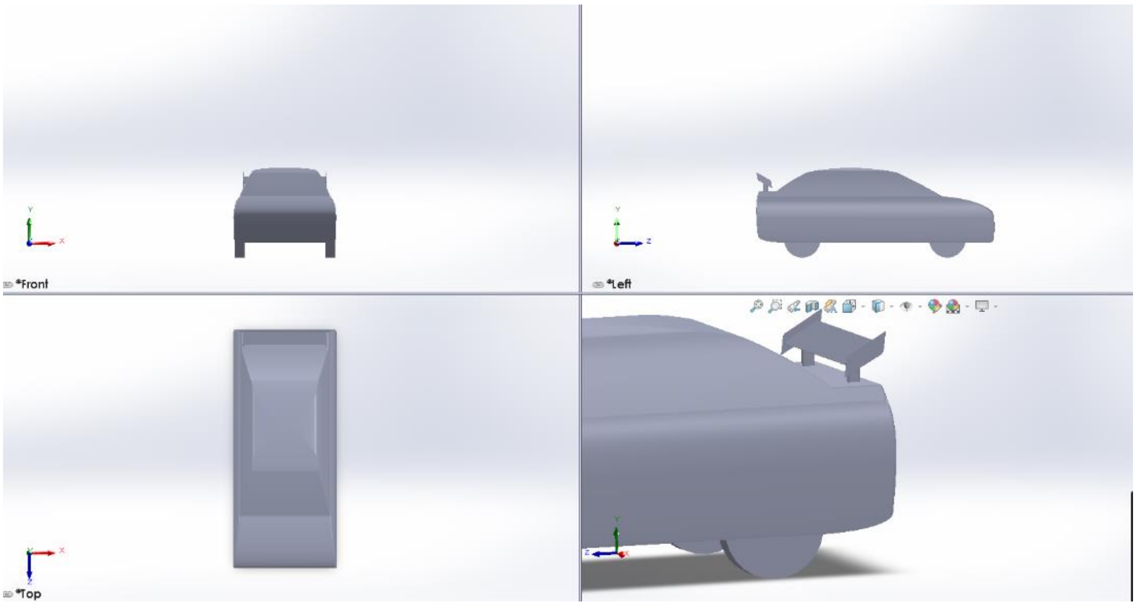

Figure 3.20. Model five (baseline model with spoiler inclined at a 40-degree angle)

The model six (baseline model with spoiler inclined at a 50-degree angle) is shown on Figure 3.21.

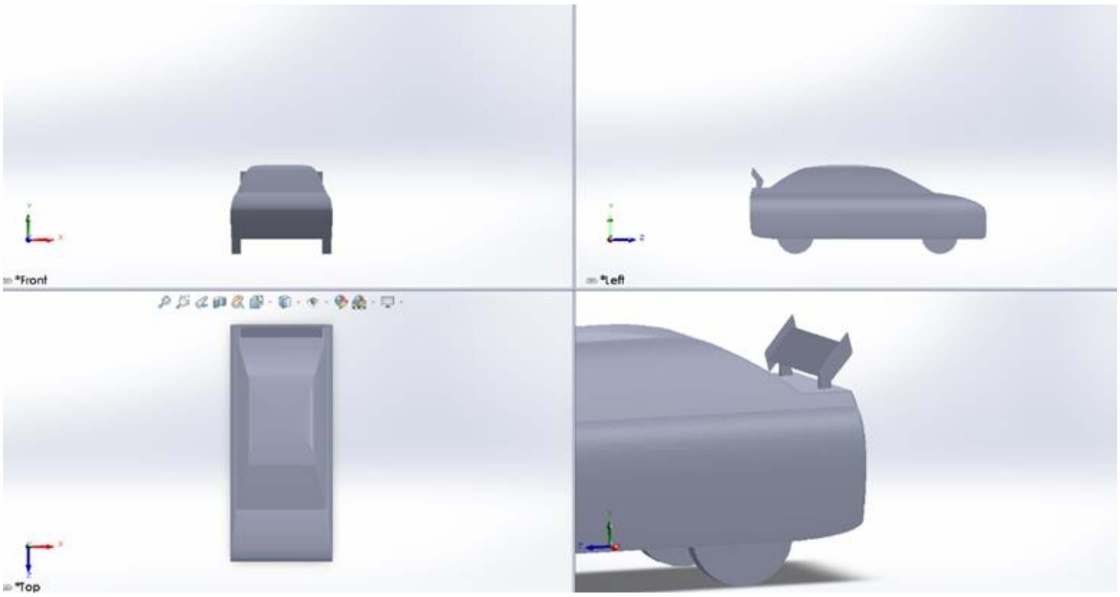

Figure 3.21. Model six (baseline model with spoiler inclined at a 50-degree angle)

The model seven (baseline model with spoiler inclined at a 90-degree angle) is shown on Figure 3.22.

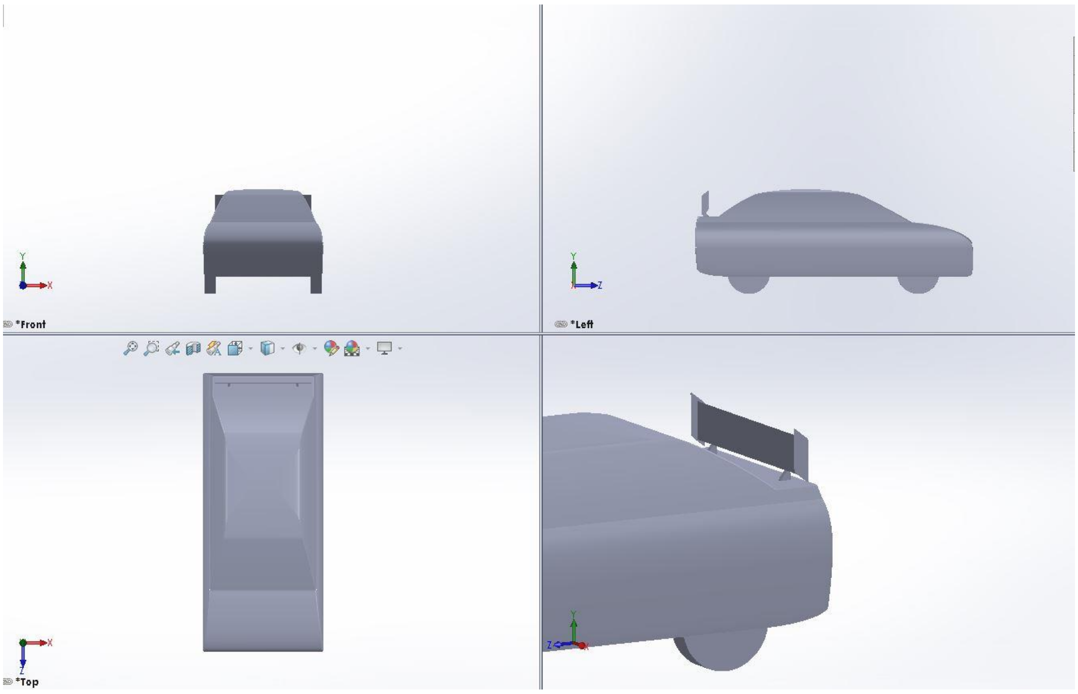

Figure 3. 22. Model seven (baseline model with spoiler inclined at a 90-degree angle)

3.2.3 Turbulence Modeling

Computational fluid dynamics (CFD) uses turbulence models to simulate turbulent flows. These models give closure to the governing equations of fluid flow, the Reynolds-averaged Naiver-Stokes (RANS) equations. Selecting the turbulence model requires taking into account the specific flow conditions and needed level of accuracy. The most widely used turbulence models in ANSYS Fluent are the k-omega and k-epsilon models. The SST (shear stress transport) k-ω turbulence model was applied in this study. Because the SST (Shear Stress Transport) k-omega turbulence model is an effective tool for simulating turbulent flows and SST k-omega turbulence model is preferred two-equation eddy-viscosity model for aerodynamic purposes. It integrates the advantages of two popular turbulence models: those are:

k-omega: it can resolve all the way down to the boundary layer, it works exceptionally well close to walls.

k-epsilon: less sensitive to turbulence when it is far from boundary.

The k-epsilon behavior in the free stream and the k-omega formulation near walls are smoothly transitioned using a mathematical function. This guarantees that the model makes use of the most advantageous features of both strategies in the relevant areas.

3.2.4 Developing an Adjustable Spoiler Prototype

This section covers all processes involved in developing both the software and hardware components of the prototype.

3.2.4.1 Programing Arduino UNO

The Arduino IDE is a software program that enables the creation of programs in a simple text editor, their compilation into machine code, and their download to all Arduino versions. The Arduino IDE software was used to program the Arduino UNO microcontroller. This software provides a wide range of libraries and is an easy-to-use platform for writing, compiling and uploading code to the Arduino UNO board. The C and C++ programming languages (embedded C) can be used to program microcontrollers using a standard API known as the Arduino programming language. The setup and loop functions in the Arduino IDE are essential building blocks for the code. The setup function is a fundamental part of any Arduino program. It operates just once at the start, immediately after uploading the code to Arduino, much like the initialization portion of the code. To initialize the board and get it ready for use, a few standard procedures are frequently carried out.

Common tasks performed in setup:

Library Initialization: Libraries in Arduino extend the fundamental Arduino features by providing additional functionality. To use these libraries in the software, initialization must be done within the setup function. Library initialization allows users to define settings, allocate resources, and create objects that are unique to the library's use. It ensures that the Arduino application is properly configured to interact with the libraries' enhanced functionality.

Initializing Variables: In Arduino programming, initializing variables is critical to a smooth-running sketch. There are two major approaches to accomplish this. The most usual way is to declare the variable's data type and name, as well as assign a starting value, all on one line during declaration. This ensures clarity and prevents any unexpected behavior. Alternatively, you can initialize variables within functions, particularly if the initial value is based on calculations or user input obtained within that function. This technique provides additional flexibility in dynamic settings. Regardless of the technique, initializing all variables before usage is critical for producing clean and dependable Arduino code.

Setting Pin Modes: Many Arduino projects require connection with the physical environment using sensors and actuators connected to the board's pins. Pin Mode is utilized to configure these pins. It specifies whether a pin will be an input or output. INPUT pins are set up to receive signals from sensors. When a sensor detects something, it transmits a signal to the Arduino via its input pin. OUTPUT pins are set up to send command signals to actuators. Based on the data it receives from the input pins and the code.

Serial Communication Setup: Setting up serial connection in Arduino functions as a gateway for data interchange with a computer. This allows for program monitoring, debugging, and even user engagement. There are two major approaches: hardware serial and software serial.

The loop function in Arduino is the heart of the program's continuous running. Loop continues to run as long as the Arduino is powered. This makes it perfect for repeatable activities. It organizes the execution of numerous tasks within the program, ensuring that each component fulfills its function at the appropriate time. Within the loop, the code can be written to:

Read Sensor Data: The loop function in for continuously collecting data from numerous sensors connected to the board. These sensors serve as the project's eyes and ears, providing critical information about the surrounding environment.

Respond to User Input: The loop function in Arduino allowing programs to react to user input, making projects more interactive and responsive to actions taken by users.

Control External Devices: It serves as the control center for external devices, allowing projects to interact with the physical environment and make ideas a reality.

Making Informed Decisions: The loop method is the foundation for developing interactive programs. It allows the Arduino to become an intelligent device that adapts and responds to its surroundings. This repeated loop converts static procedures into dynamic entities capable of sensing, responding to, and influencing the physical world. It serves as the foundation for leveraging Arduino's capability in a wide range of creative and inventive applications.

3.2.4.2 Circuit design and simulation

The Proteus software and Cirkit Designer used for circuit design and simulation. A set of tools for creating and simulating electronic circuits is provided by Proteus software. Before building physical prototypes, Proteus software can be used to model and analyze the behavior of circuits to make sure they operate as intended. Finally, Cirkit Designer was used to show a clear representation of the actual components and their wiring diagram.

3.2.4.3 Assemble electronic components

This is a process of connecting electronic components to do. It is related to building a device's skeleton and muscles, and providing it with real-world functionality. The Arduino UNO Board, solid state relay, solenoid, breadboard, brake switch, infrared speed sensor LCD, DC motor, circuit wire and Mini DC motor PWM Speed Controller are the parts that make up the hardware of the adjustable rear wing spoiler. Each contributes differently to the functionality of the device.

CHAPTER FOUR

SYSTEM MODELING AND ANALYSIS

4.1 ANSYS Fluent Setup and Procedure

A workhorse piece of software, ANSYS Fluent enables the use of computational fluid dynamics (CFD) to simulate and analyze fluid flow on a computer. This means that designs involving heat transfer, motion of fluids, and other related phenomena can be virtually tested and improved. It has advanced features to enhance your simulations. It provides a large collection of models that take heat transmission, turbulence, and other complexity into consideration. It also offers strong solvers to crunch the numbers and meshing tools to build a digital grid inside the flow domain. ANSYS fluent setup and process entail several basic elements to prepare and run a computational fluid dynamics (CFD) simulation. Those are:

Pre-processing: It is an essential first step in configuring a computational fluid dynamics (CFD) simulation in ANSYS Fluent. It entails making a 3D model of the object or environment where the fluid flow will occur and using it to define the geometry of the flow domain, either directly within the ANSYS Workbench or with the help of another CAD program, and setting up the mesh by discretizing the flow domain into tiny cells. The preparation process also includes defining the simulation's boundary conditions. For the simulation to be accurate and effective, preprocessing is essential.

Solving: The solver is a computational technique used to solve transport equations (Zafaruddin et al., 2023). In ANSYS Fluent, specify the details for the simulation during the setup and conditions phase after choosing your models. This entails defining boundary conditions, such as velocity, pressure, or temperature at inlets and outlets, at the boundaries of the flow domain. Walls can be classified as moving, immovable, or possessing certain qualities related to heat transfer. Problems involving symmetrical flow are solved using symmetry planes. Along with selecting the suitable solver type, it will also define material parameters for solids and fluids. To manage the solution process and identify the point at which a reliable and accurate result is attained, convergence criteria, under-relaxation factors, and residuals are defined. Lastly, to provide the simulation with a starting point, this initializes the flow variables within the domain. Recall that for an accurate result, these parameters need to match the actual situation you are attempting to replicate. can set up ANSYS Fluent to precisely and quickly solve your CFD problem by carefully defining these settings.

Post-processing: Analyzing and displaying the simulation's output is known as post-processing, and it is a crucial stage in the CFD simulation workflow. All ANSYS fluid dynamics products share ANSYS CFD-Post as a common post-processor, giving users a variety of tools to examine and understanding the outcomes once ANSYS Fluent has solved the problem. Here is where the unprocessed data gets turned into valuable insight. To make the findings more visually appealing, ANSYS Fluent provides a range of visualization tools. Pressure contours can be seen as color maps highlighting high and low pressure zones, temperature distributions displaying hot and cold areas, and velocity vectors as arrows indicating flow direction and amplitude.

4.1.1 Creating a virtual wind tunnel

ANSYS Fluent makes it possible to build a virtual wind tunnel and test designs virtually. Construct the wind tunnel, which is just an enclosure for the 3D model of the vehicle, and it has an entrance for entering air, an exit for outgoing air, as well as a possible larger domain to reduce the impact of the tunnel walls. To capture the wake region of the vehicle more precisely, the domain space behind the vehicle has been extended. The walls of the virtual wind tunnel have less of an impact on the flow when the domain behind the car is longer, especially around the wake zone. This guarantees that the wake that appears is mostly caused by the way the vehicle is built, instead of impacts from the tunnel walls being too close. For a simulation of the air flow toward the car body, a fluid volume box that will enclose the car as the air domain must be created by enclosing the car and removing the car body using the Boolean function. Only half of the domain was taken into consideration because of the car's symmetrical form. The dimensions of the enclosure were measured as three car lengths in the front, five car lengths between the rear of the vehicle and the end of the enclosure, and two car lengths on the sides (Abdellah & Wang, 2017). The car's length is 3.995 m. Table 4.1 gives the dimensions of the enclosure.

Table 4.1. Enclosure's dimensions

Upstream length (m)	Downstream length (m)	Width (m)	Height (m)
11.985	19.975	8.8575	9.505

Figure 4.1 below shows a computational model within a virtual wind tunnel.

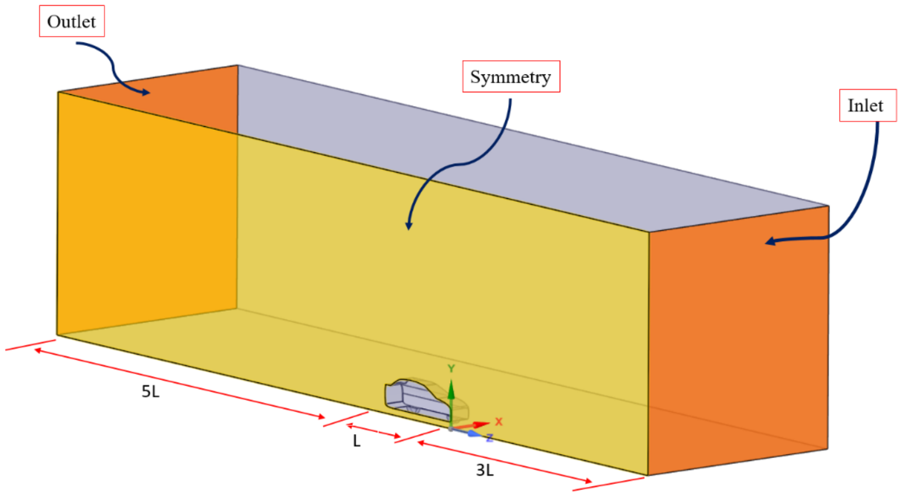

Figure 4.1. Baseline model in virtual wind tunnel (enclosure)

4.1.2 Meshing of the Model

Once the geometry is complete, a suitable mesh needs to be developed for the vehicle model. The Boolean operator was used to deduce the body volume from the control volume. By doing this, the mesh size is decreased without affecting the result. When creating the mesh, much attention should be paid to mesh refinement around critical surfaces such as the vehicle body and the spoiler. The goal should be to achieve the best possible balance between the attained level of fineness and the computational cost. In this study, polyhedral meshes were developed. Polyhedral mesh combines the benefits of tetrahedral cells, which are simple to create even in complex geometries such as the curved surfaces of the vehicle model, and hexahedral cells, which produce precise solutions and have low numerical diffusion. Polyhedral meshes could save about 95% of processing time without losing model accuracy when compared to the other two mesh types (tetrahedral and hexahedral) with almost identical grid numbers (Chen et al., 2022). The polyhedral mesh's CFD simulation findings are more consistent with experimental data than the tetrahedral mesh at the identical cell number (H. Zhang et al., 2020). The orthogonal quality and skewness should be taken into account while examining the meshing quality. Depending on what the fluid users guide mentions. The skewness value is less than 0.95 and the orthogonal quality value can be between 0 and 1. The term orthogonal quality describes how near to 90 degrees the angles between the mesh lines are and Skewness is a measure of a cell's distorted from a regular form. In ANSYS, boundary layers must be carefully taken into account in order to accurately represent the complex flow behavior close to walls during CFD simulations. The number of layers utilized is not predetermined more layers improve accuracy and resolution, they also raise computing costs. Figure 4.2 below shows the mesh of the baseline model.

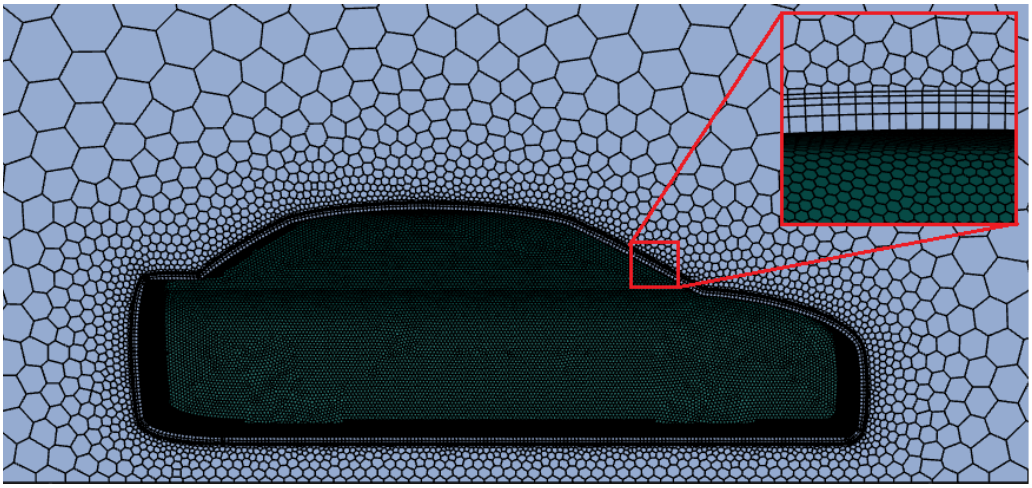

Figure 4.2. Mesh of baseline model

4.1.3 Grid independence test

In CFD (computational fluid dynamics) applications, a grid independence test, also referred to as a mesh independence test, is an essential procedure to guarantee simulation accuracy. It basically confirms that the particular mesh (grid) employed to discretize the computing domain has no noticeable effect on the results obtained. Grid dependence tests are crucial to CFD because they help to balance computational cost and accuracy while making the best use of available computational resources.

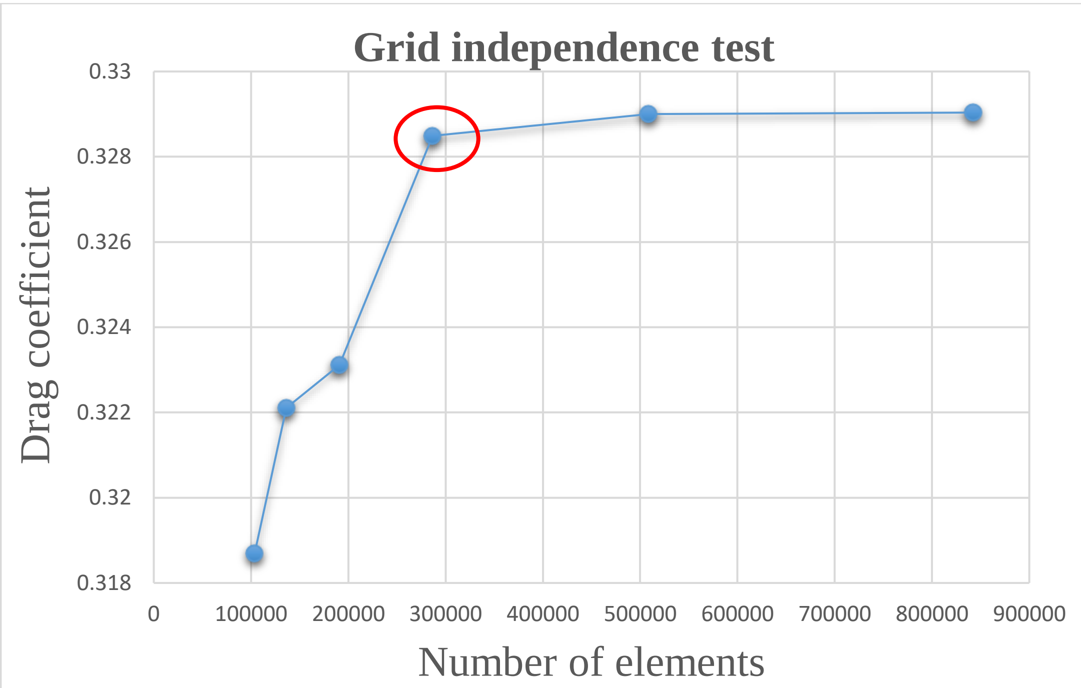

Figure 4.3. Grid independence test

A flat line indicates that there is minimal to no variation in the chosen parameter (commonly referred to as a convergence parameter) when the mesh is refined. The fluctuation of the drag coefficient is noticeable in relation to the mesh. Variations in the results are negligible beyond the indicated cell zone. Better results will be obtained in short time with this mesh size than with a finer mesh.

4.1.4 Grid convergence index

The grid convergence index (GCI) method is a generally recognized and advised technique for assessing discretization error. It was utilized to test the mesh sensitivity (Jiang et al., 2018).For discretization error estimates, ASME (American Society of Mechanical Engineer) And AIAA (American Institute of Aeronautics and Astronautics) both advice using the Richardson Extrapolation approach. A minimum of three systematic mesh refinements are necessary for the Grid Convergence Index (GCI) approach, and each one requires that the numerical solution fall within the asymptotic range (Baker et al., 2019; Lee et al., 2020).

In this analysis, the medium grid was found to have the optimal grid density, as determined by the grid independence test.

The grid refinement ratio (r) was computed using in order to get the GCI.

$$r = \left(\frac{\Delta_{\text{fine}}}{\Delta_{\text{coarse}}}\right)^{1/3} \tag{4. 1}$$

Where the number of grids in the fine grid condition is denoted by Δ_{fine}, and the number of grids in the coarse grid condition by Δ_{coarse}.

A value greater than 1.3 for the grid refinement ratio is advised in order to differentiate the discrete fault from other defects (Lee et al., 2020). Richardson's extrapolation was used to determine the GCI.

$$\text{GCI} = F_s \frac{\varepsilon}{r^p - 1} \tag{4. 2}$$

Where ε is the relative error among the two grid conditions in the simulation, p is the order of convergence, and Fs is the safety factor. When evaluating a minimum of three grids, the Fs value is 1.25. The following formula is used to determine p:

$$p = \frac{\ln |(f_{\text{coarse}} - f_{\text{medium}})/(f_{\text{medium}} - f_{\text{fine}})|}{\ln r} \tag{4. 3}$$

Were f_{coarse}, f_{medium}, f_{fine} represents as coarse, medium, and fine grid conditions respectively. ε represents the numerical solution error for every grid condition and is determined with

$$\varepsilon = \frac{f_{\text{coarse}} - f_{\text{fine}}}{f_{\text{fine}}} \tag{4. 4}$$

The Figure 4.4 below shows coarse ,medium and fine meshs

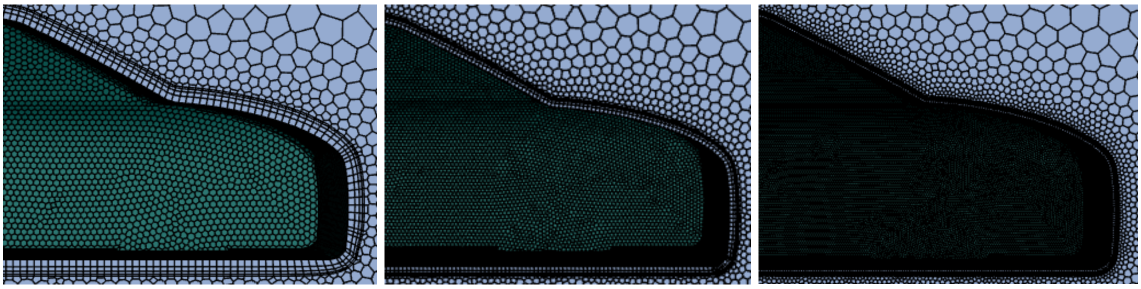

(a) (b) (c)

Figure 4.4. Mesh size (a) coarse (b) medium mesh (c) fine mesh

Table 4.2. Sizes of mesh with the parameters

Parameters	Coarse mesh (1)	Medium mesh (2)	Fine mesh (3)
Element number	103659	286661	842523
Drag coefficient	0.3187	0.3285	0.3290

Table 4.3. Refinement ratio (r)

r21	r32
1.404	1.432

Table 4.4. Grid independence index value

Order of convergence		Normal Error		Safety factor	Grid convergence index(GCI)	
P21	P32	ε21	ε32	*F*s	GCI 21%	GCI 32%
8.78E+00	8.29E+00	3.1E-02	1.5E-03	1.25	0.21%	0.01%

The GCI values decrease as the grid is refined further (i.e. GCI 32 < GCI 21). GCI 32 is lower, which shows that the numerical outcomes are becoming less influenced by cell size and that the solution is getting closer to achieving grid independence.

4.1.5 Boundary Conditions

An essential component of any computational fluid dynamics (CFD) simulation is boundary conditions. In essence, they provide an explanation of what occurs at the boundary of computational domain. The properties of the fluid entering the computational domain are mainly specified by the inlet boundaries. Flow velocity is the most often defined property. It specifies the absolute velocity values at the inlet. The analysis was carried out on no-slip moving roads, upper and sidewalls, at three varying speeds (80, 120, and 160 km/h). The fluid's exit from the computational domain is determined by the outlet boundary conditions. The pressure outlet boundary is selected, and the outlet gauge pressure is set to zero. Table 4.5 shows all boundary conditions in the analysis.

Table 4.5. Boundary conditions

Name	Boundary type	value
Inlet boundary condition	Velocity inlet	speed (V) =22.222m\s speed (V) =33.333m\s speed (V) =44.444 m\s
Outlet boundary condition	Pressure outlet	Gauge pressure = 0 Pa
wall boundary condition	Top wall	speed(V)=(22.222,33.333,44.444 m\s)
	Left side wall	speed(V)=(22.222,33.333,44.444 m\s)
	Road	speed(V)=(22.222,33.333,44.444 m\s)
	car	Stationary
Symmetry boundary condition	symmetry	

4.1.6 Solver Stage

In order to determine how the simulation will be solved and reach convergence, ANSYS Fluent's solver settings cover a number of important categories: solver type (2D or 3D), viscous model, boundary conditions, and solution controls. In this study, 3D pressure-based type solver, absolute velocity, and steady time were chosen for the solution. The boundary condition was then built, with the Inlet (Velocity Inlet) set at various speeds for this study (80, 120, and 160 km/h), and the Outlet set as a Pressure Outlet with zero gauge pressure. Following the creation of the boundary condition, the reference value was taken from the inlet. Under the viscous model the chosen turbulent model was RANS with k-ω SST for all models. For the velocity inlet, the turbulence intensity was lowered to 1%. The root-mean-square of the velocity fluctuations over the mean flow velocity is the definition of turbulence intensity. Assuming that the flow is quite laminar at the control volume's inlet, a 1% turbulence intensity is relatively low, indicating constant airflow and very little turbulence from the velocity added to the simulation. The pressure-velocity coupling approach was used, with the coupled scheme being utilized for a robust solution of the pressure and velocity fields. Under discretization schemes the second order was chosen for pressure, and the second order upstream was utilized under discretization schemes for turbulent kinetic energy, momentum, and turbulent dissipation rate. The relaxation factors were set at 0.2 for pressure and momentum and 0.8 for the specific dissipation rate and turbulent kinetic energy. During the first few iterations, relaxation factors can aid in stabilizing the solution. Before the simulation began, the hybrid initialization was utilized to set initial values for all the pertinent variables (such as temperature, pressure, and velocity) in the computational domain. The drag and lift coefficient reports were defined in the report definition option. The value of residual set to 1e-03 in Monitor option for increased solution accuracy. The default timescale factor of one second was chosen for the calculation, and 800 iterations were set.

The outlet boundary condition remains fixed during the whole research state, while the intake boundary conditions were adjusted based on the fluid flow velocity.

Table 4.6. Solver setting

solver	
Type	3D pressure based
Time	Steady
Velocity formation	Absolute
Viscous model	SST k-omega turbulence model
Solution methods	
Pressure-Velocity Coupling scheme	Coupled
Pressure	Second Order
Momentum	Second Order Upwind
Turbulent Kinetic Energy	Second Order Upwind
Turbulent Dissipation Rate	Second Order Upwind
Number of iterations	800

CHAPTER FIVE

RESULTS AND DISCUSSIONS

This section discusses the results of CFD simulations performed on various models using ANSYS FLUENT, including the baseline model, Models one, model two, model three, model four, model five, model six, and model seven. Figures, plots, and Tables are used throughout the investigation to show and evaluate the computational effects of each model.

5.1 Baseline model

5.1.1 Scaled Residual Convergence

In the virtual wind tunnel model, three inlet velocity speeds were used: 80 km/h, 120 km/h, and 160 km/h. 800 iterations of the simulation were run for each case until the convergence requirements were met. According to the simulations that were run, the scaled residuals for all models were below 1e-2. Figure 5.1 shows the plots of scaled residuals.

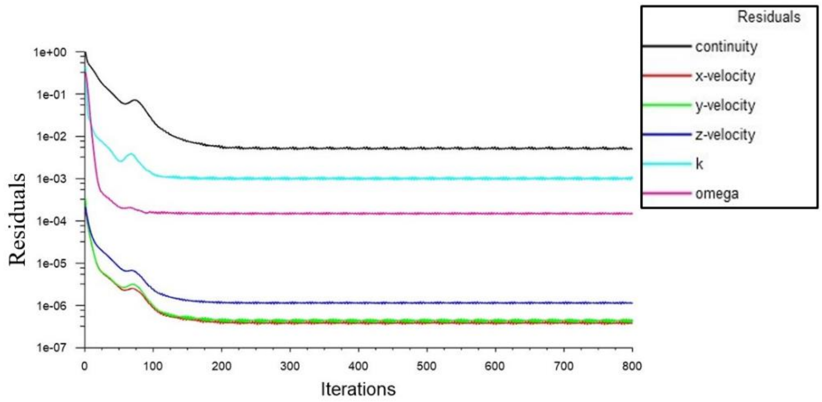

Figure 5.1. Scaled residuals convergence history for baseline model

5.1.2 Drag and Lift Coefficients

The convergence history of the drag and lift coefficients for the baseline model at three different speeds (80, 115, and 160 km/h) is shown in Figures 5.2–5.7.

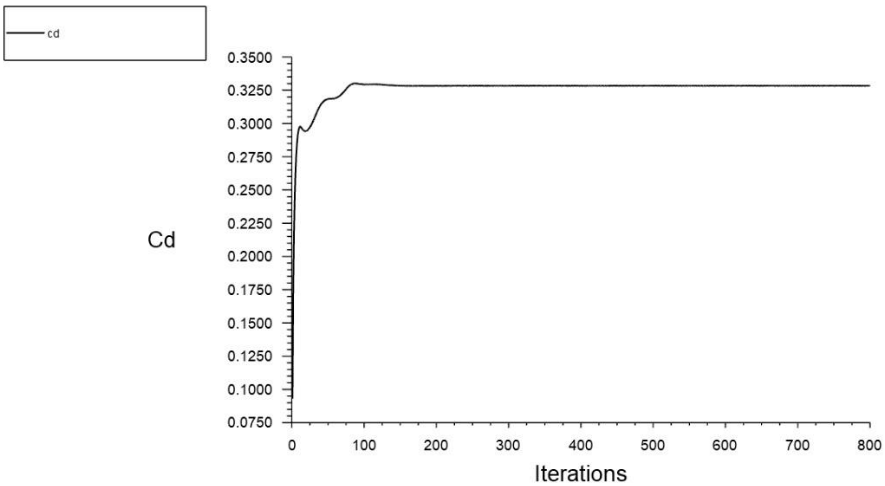

Figure 5.2. Drag coefficient convergence history of base line model at 80 km/h

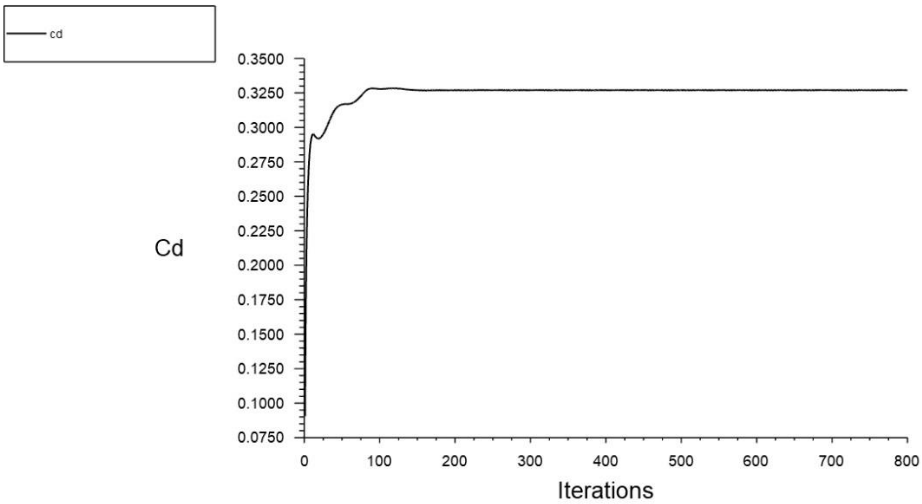

Figure 5.3. Drag coefficient convergence history of base line model at 120 km/h

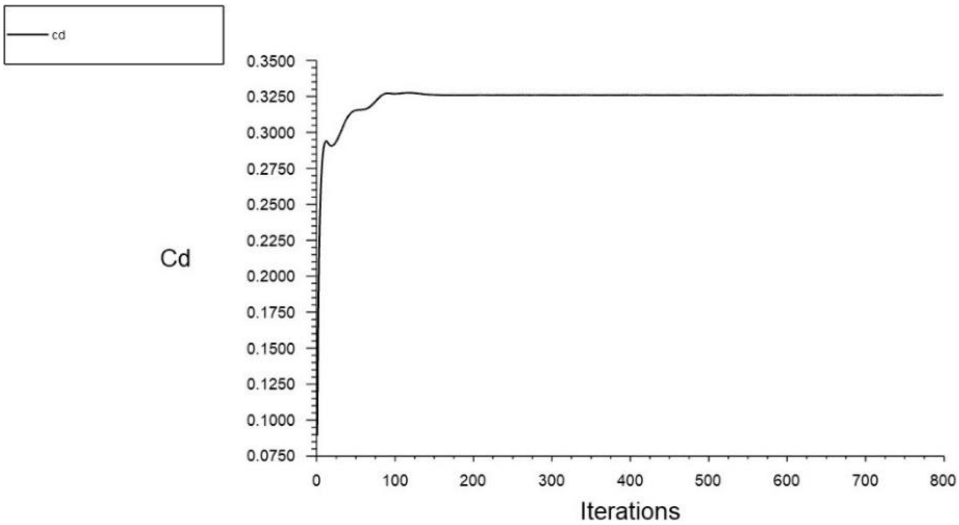

Figure 5.4. Drag coefficient convergence history of base line model at 160 km/h

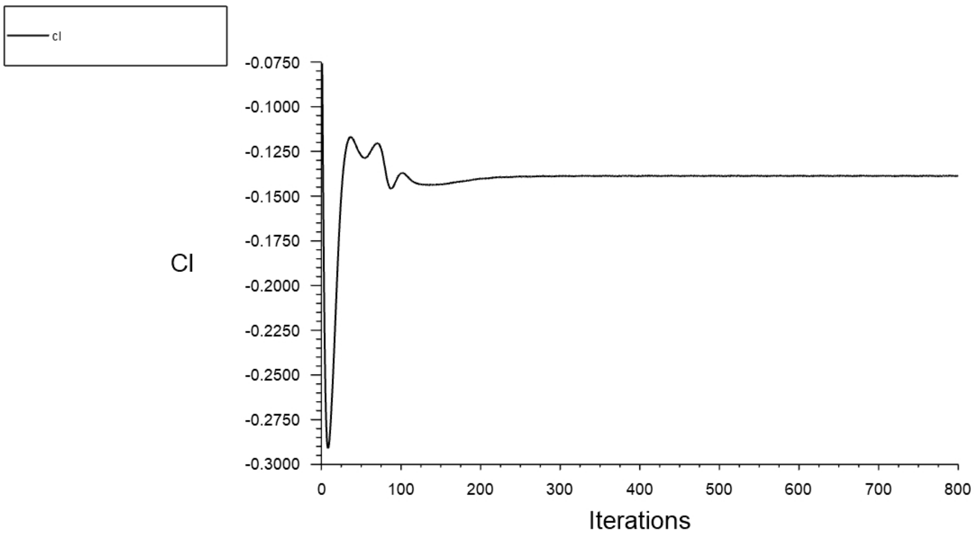

Figure 5.5. Lift coefficient convergence history of base line model at 80 km/h

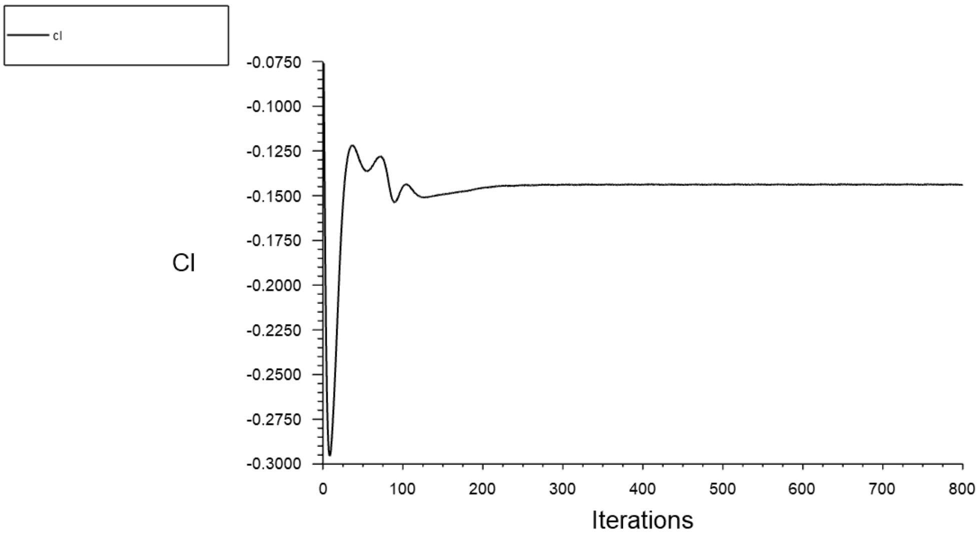

Figure 5.6. Lift coefficient convergence history of base line model at 120 km/h

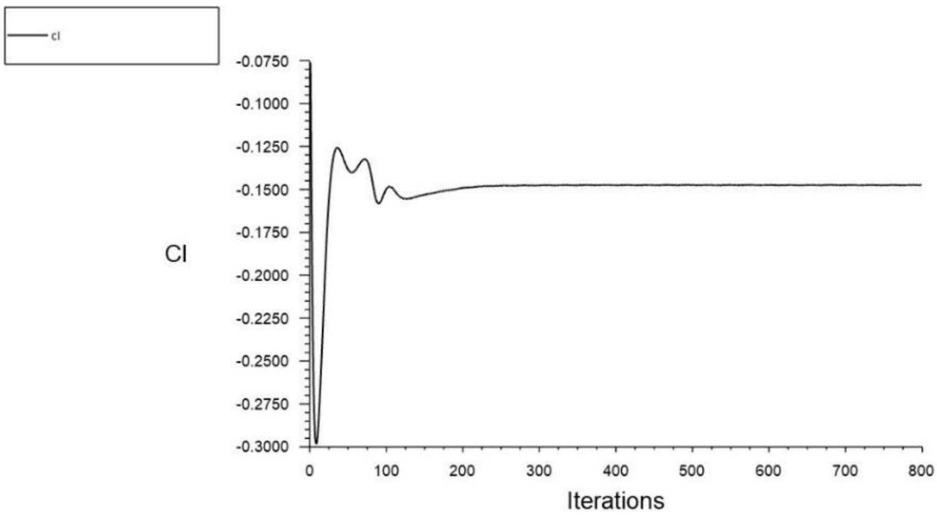

Figure 5.7. Lift coefficient convergence history of base line model at 160 km/h

The drag and lift coefficient convergence histories in Figures 5.2–5.7 above show that both parameters converged well before the 800th iteration.

Table 5.1. Drag and lift coefficient of the baseline model at various speeds

Model	Speed		C_d	C_l
	km/h	m/s		
Baseline model	80	22.222	0.3283	-0.1390
	120	33.333	0.3270	-0.1441
	160	44.444	0.3256	-0.1477

The drag and lift coefficients of a baseline model examined at different speeds are summarized in Table 5.1 above. It allows the comparison of the changes in the aerodynamic force coefficients of the model with increasing velocity. The drag coefficient of the baseline model decreased with increasing speed, suggesting decreasing aerodynamic resistance. While the lift coefficient was lowered, this leads to increased vehicle stability at high speeds.

5.1.3 Pressure contour

Figures 5.8–5.10 show the pressure contour on the symmetry plane and on the body of the baseline model at three different velocities (80, 120, and 160 km/h).

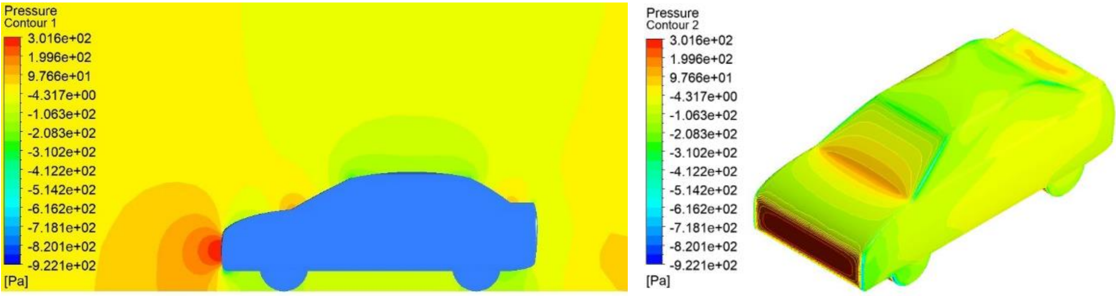

(a) (b)

Figure 5.8. Pressure contour (a) on symmetry plane (b) on body of baseline model at 80 km/h

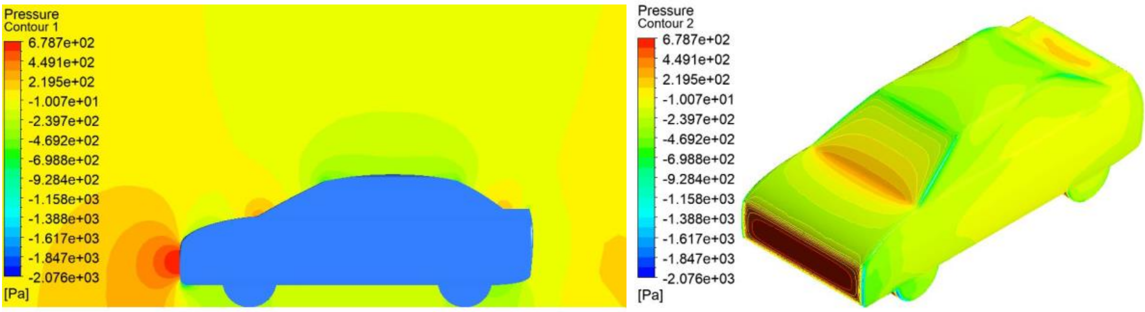

(a) (b)

Figure 5.9. Pressure contour (a) on symmetry plane (b) on body of baseline model at 120 km/h

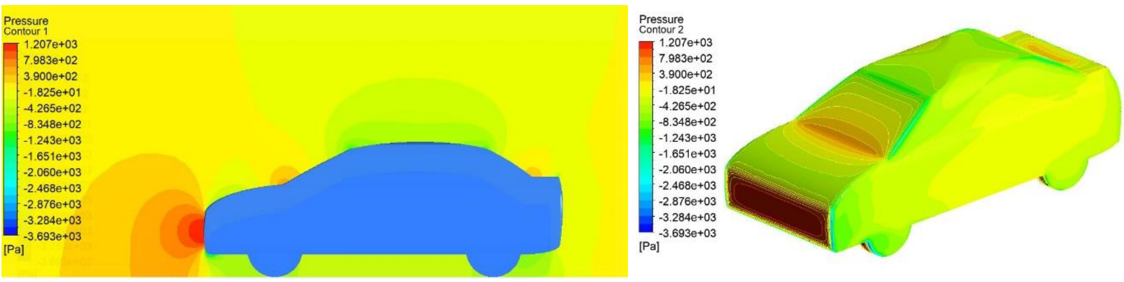

(a) (b)

Figure 5.10. Pressure contour (a) on symmetry plane (b) on body of baseline model at 160 km/h

The level of pressure influence on the car's surface is shown in Figures 5.8–5.10, indicated by the contour of the static pressure distribution. The contour of the pressure distribution in Figures 5.8–5.10 clearly indicates three regions with positive pressure, and the maximum pressure increased as speed increased. The first is at the front of the baseline model with the highest pressure, which represents the initial force applied to the car's surface where the air meets it, is known as stagnation pressure. Additionally, notice that the wheels that are predominantly red receive a significant amount of pressure. The second one is located between the front hood and windshield. The third is between the rear windshield and the trunk area. The blue zone is low pressure, where the air must curve around the bend, the front wheel arches, the A pillars, the roof, and so on, due to Bernoulli's principle, which indicates that pressure decreases with increasing air speed.

5.1.4 Velocity contour and streamline

Figures 5.11–5.13 show the velocity contour and streamline flow of a baseline model at three different velocities (80, 120, and 160 km/h) on the symmetry plane.

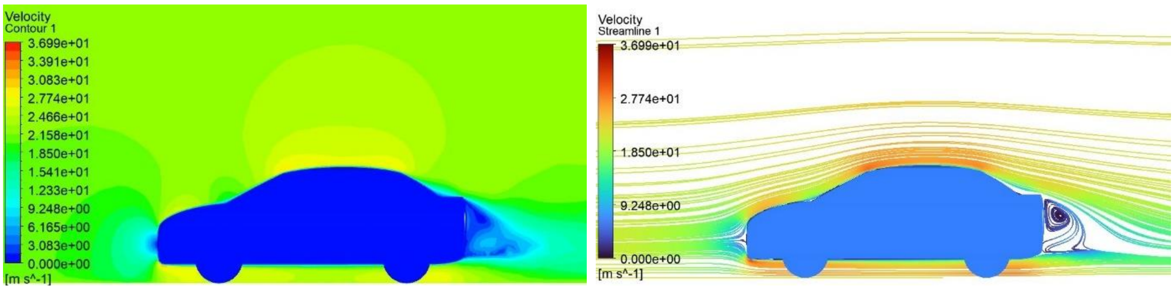

(a) (b)

Figure 5.11. (a) Velocity contour and (b) Streamline of the baseline model at 80 km/h

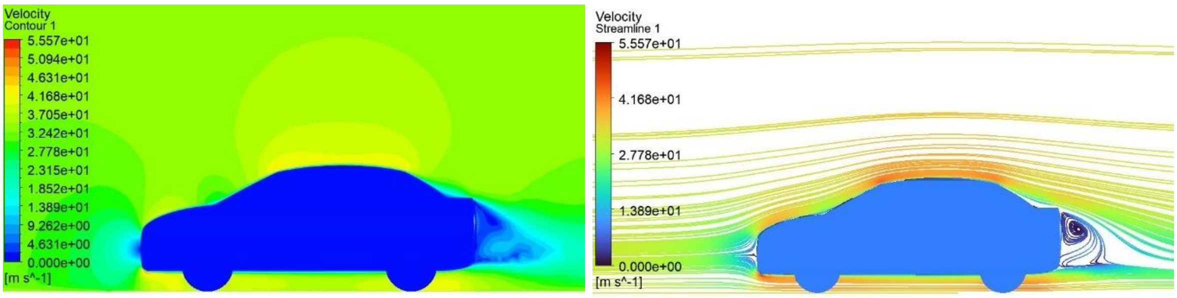

(a) (b)

Figure 5.12. (a) Velocity contour and (b) Streamline of baseline model at 120 km/h

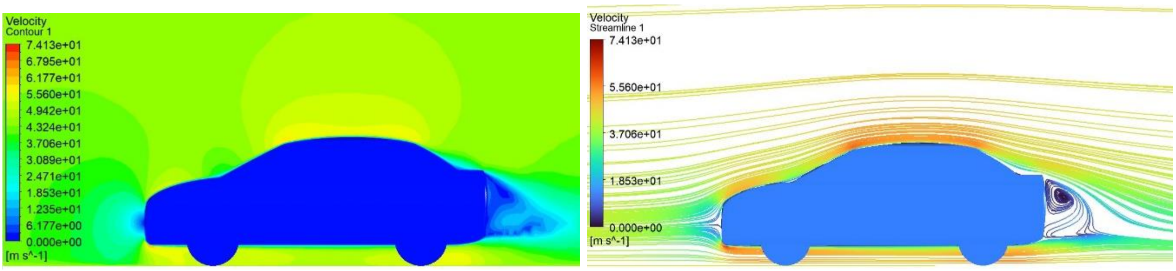

(a) (b)

Figure 5.13. (a) Velocity contour and (b) Streamline of baseline model at 160 km/h

The flow of air over the car body causes a velocity distribution, leading to aerodynamic loads on the body of the baseline model. The velocity distribution shows the amount of velocity at various region of the baseline model. Due to the airflow separation seen in Figures 5.11–5.13, the airflow becomes turbulent, resulting in the formation of a lower pressure area toward the rear of the vehicle. From Figures 5.11 (b)–5.13 (b) also can see, streamlines plot shows the airflow that travels through the body's upper and lower sections was isolated from the vehicle's body. The area of circulation is seen behind the vehicle. The lower the circulation zone, the less turbulence is formed. The amount of turbulence behind the car, known as the wake, determines the drag force. Maximum turbulence produces maximum drag force.

5.2 Validation of Model

The process of verifying computational fluid flow models includes evaluating the precision and dependability of the results by contrasting them with prior research (Nagappan et al., 2023). The findings of earlier research were used to validate this study (Malik & Parshad, 2023). The results from (Malik & Parshad, 2023) and the current study were compared in terms of pressure contour and velocity contour on symmetry, as shown in the Figures (5.14–5.17).

Figure 5.14. Pressure contour on symmetry (Malik & Parshad, 2023)

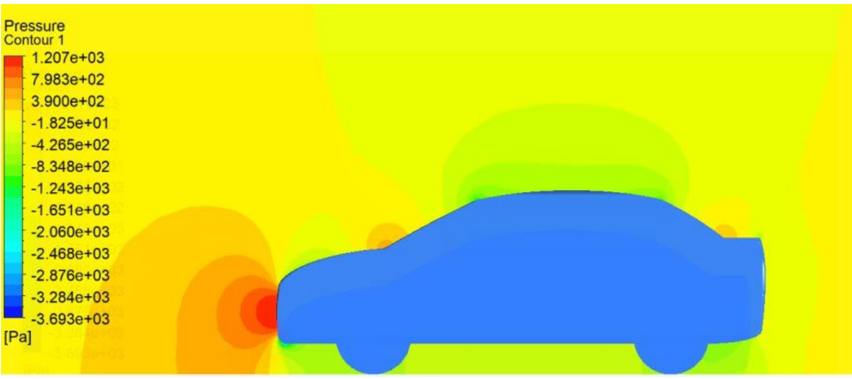

Figure 5.15. Pressure contour on symmetry

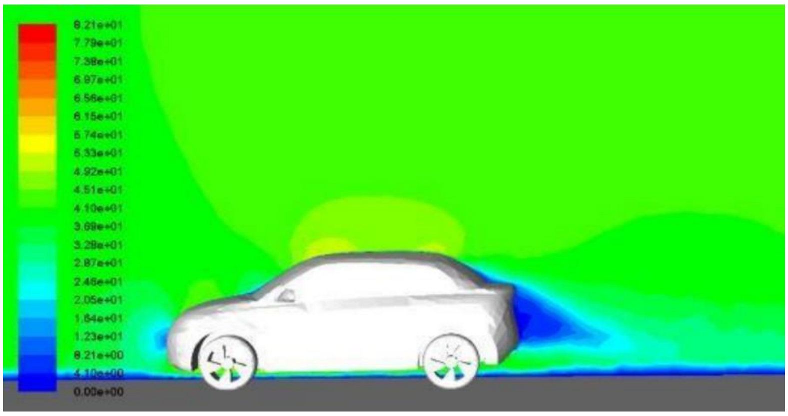

Figure 5.16. Velocity contour on symmetry (Malik & Parshad, 2023)

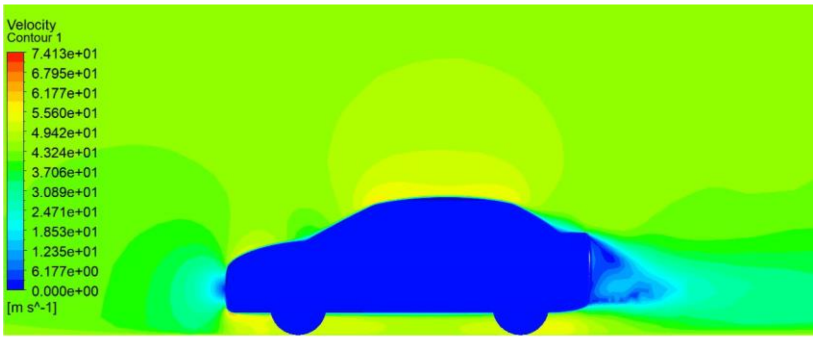

Figure 5.17. Velocity contour on symmetry

The behavior of pressure distribution and Velocity contour on symmetry design of the sedan vehicle from (Malik & Parshad, 2023) and the current study are almost identical as can be seen from the above Figures 5.14–5.17. As reported in several articles listed in Table 5.2, the drag coefficient of a sedan car is around 0.25–0.35. Therefore, the drag coefficient obtained in this simulation falls within this range.

Table 5.2. Numerically simulated mean drag coefficients obtained for the sedan car model

Parameter	Result of this study	Reported result in several articles					
		(Maji & Mustaffa, 2022)	(Selvaraju et al., 2015)	(Ismail et al., 2022)	(Paul et al., 2020)	(Socrates et al., 2018)	(Saleh & Ali, 2020)
c_d	0.327	0.259	0.312	0.313	0.324	0.325	0.34

5.3 Model one (Baseline model with a 0-degree spoiler inclination)

5.3.1 Drag and Lift Coefficients

The convergence history of the drag and lift coefficients for the model one (baseline model with rear wing type spoiler at 0-degree angle of inclination) at three different speeds (80, 120, and 160 km/h) is shown in Figures 5.18–5.23.

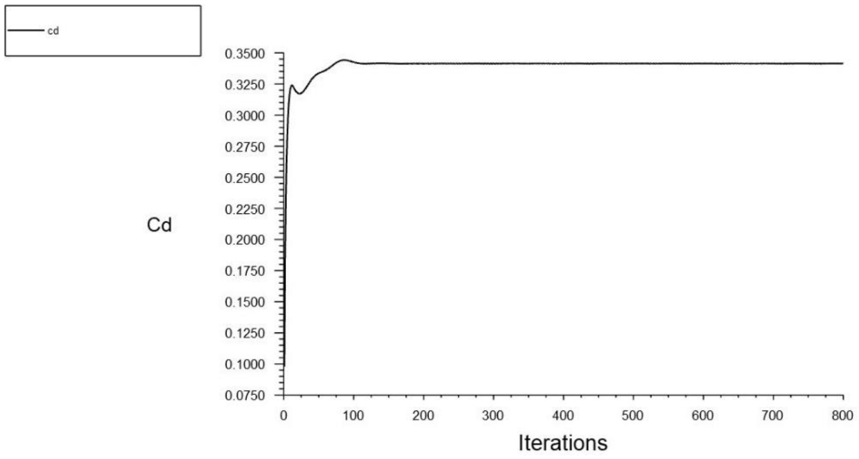

Figure 5.18. Drag coefficient convergence history of model one at 80 km/h

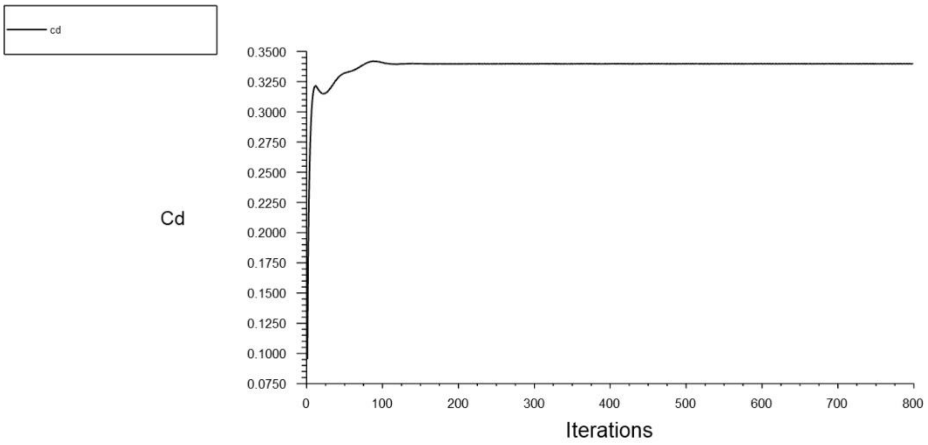

Figure 5.19.Drag coefficient convergence history of model one at 120 km/h

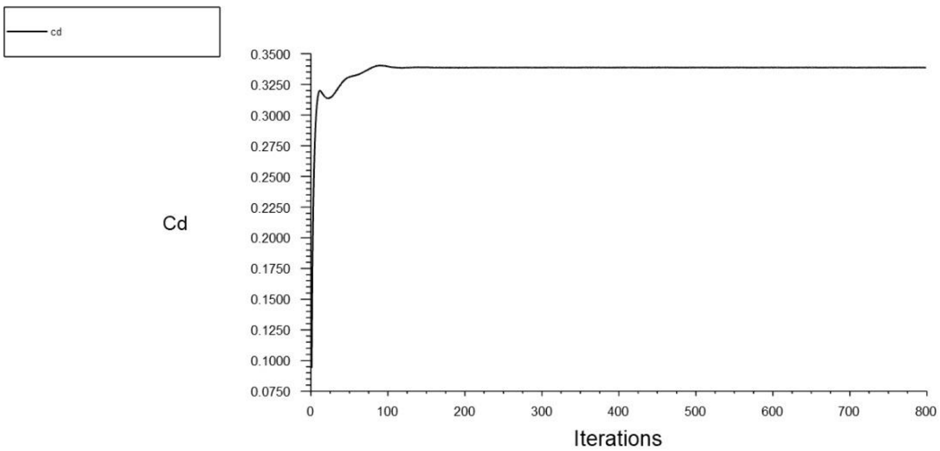

Figure 5.20. Drag coefficient convergence history of model one at 160 km/h

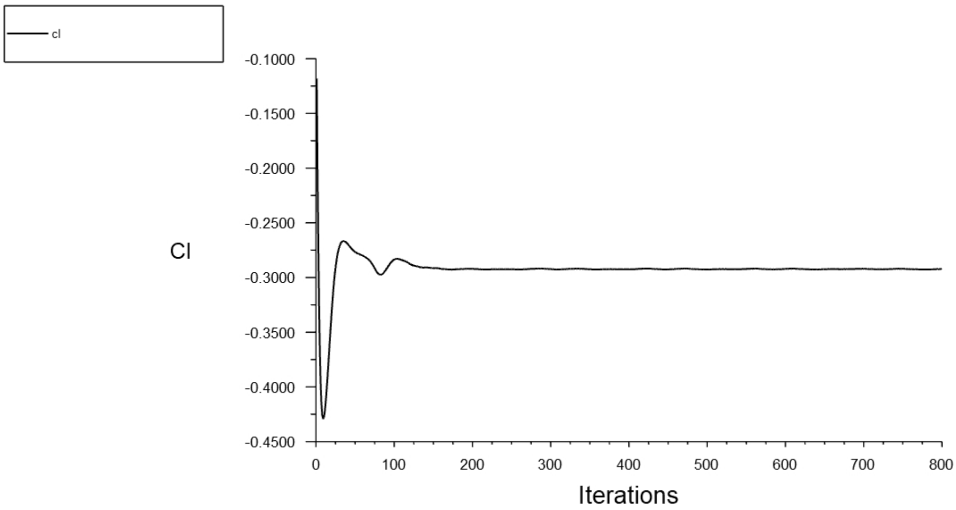

Figure 5.21. Lift coefficient convergence history of model one at 80 km/h

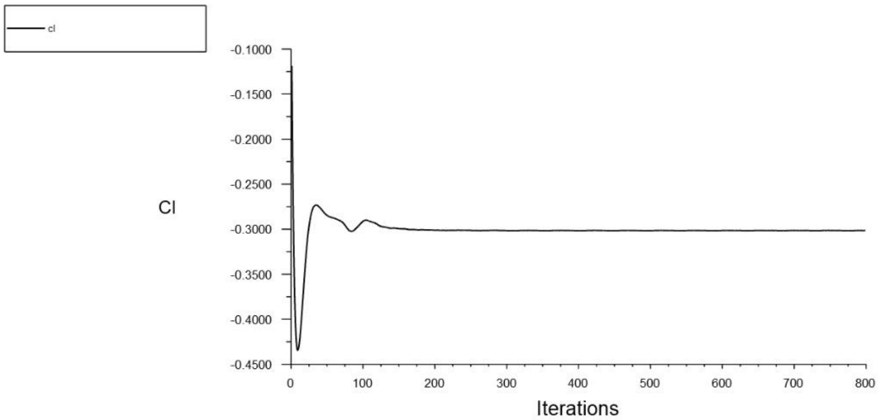

Figure 5.22. Lift coefficient convergence history of model one at 120 km/h

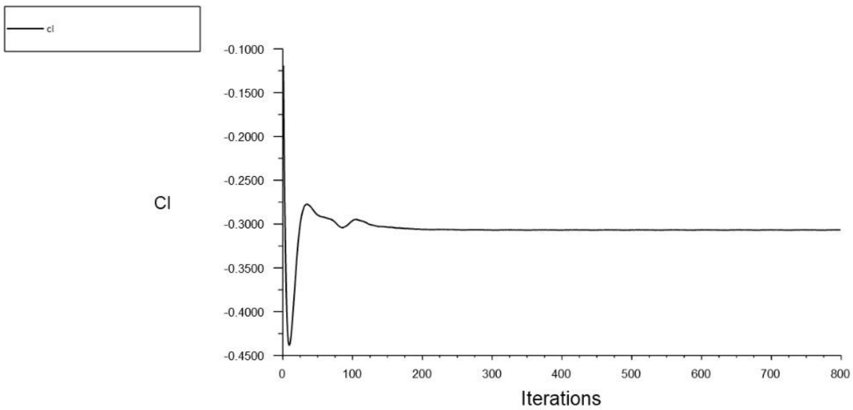

Figure 5.23. Lift coefficient convergence history of model one at 160 km/h

The drag and lift coefficient convergence histories in Figures 4.18–4.23 above show that both parameters converged well before the 800th iteration.

Table 5.3. Drag and lift coefficient of model one at various speeds

Model	Speed		C_d	C_l
	Km/h	m/s		
Model one	80	22.222	0.3414	-0.2923
	120	33.333	0.3397	-0.3013
	160	44.444	0.3387	-0.3066

The drag and lift coefficients of a model one examined at different speeds are summarized in Table 5.3 above. It allows the comparison of the changes in the aerodynamic force coefficients of the model one with increasing velocity. The drag coefficient of model one decreased with increasing speed, suggesting decreasing aerodynamic resistance. While the lift coefficient was lowered, this leads to increased vehicle stability at high speeds.

5.3.2 Pressure contour

Figures 5.24–5.26 show the pressure contour on the symmetry plane and on the body of the model one at three different velocities (80, 120, and 160 km/h).

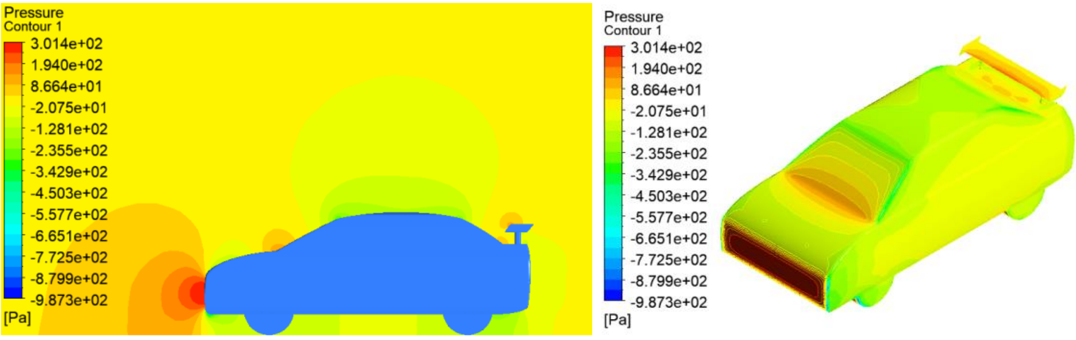

(a) (b)

Figure 5.24. Pressure contour (a) on symmetry plane (b) on body of model one at 80 km/h

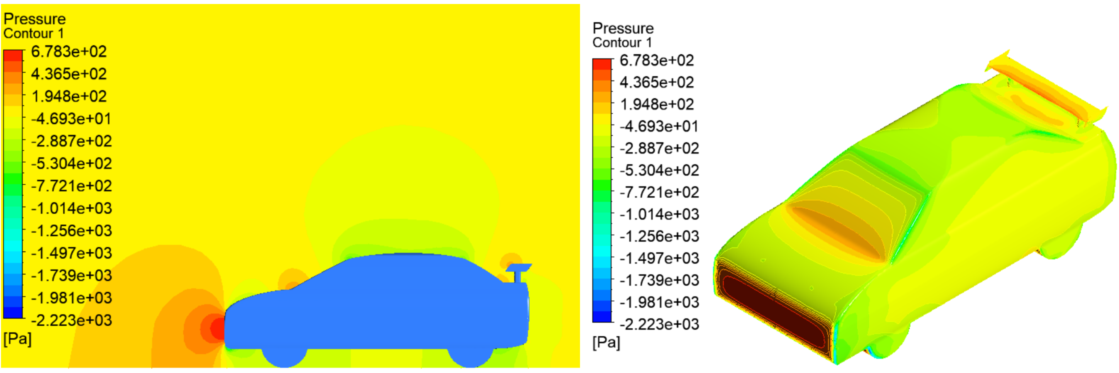

(a) (b)

Figure 5.25. Pressure contour (a) on symmetry plane (b) on body of model one at 120 km/h

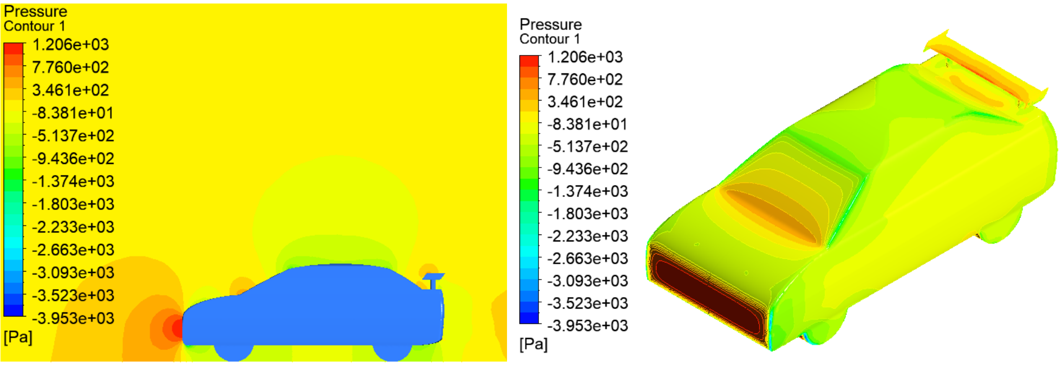

(a) (b)

Figure 5.26. Pressure contour (a) on symmetry plane (b) on body of model one at 160 km/h

The level of pressure influence on the car's surface is shown in Figures 5.24–5.26, indicated by the contour of the static pressure distribution. The contour of the pressure distribution in Figures 5.24–5.26 is more similar to the baseline model. However, when the rear wing-type spoiler is mounted on the vehicle, the region of positive pressure around the rear wing-type spoiler increases. This increases the vehicle's negative lift coefficient by applying additional pressure to the upper half of the vehicle, and it increases as speed increases.

5.3.3 Velocity contour and streamline

Figures 5.27–5.29 show the velocity contour and streamline flow of a model one at three different velocities (80, 120, and 160 km/h) on the symmetry plane.

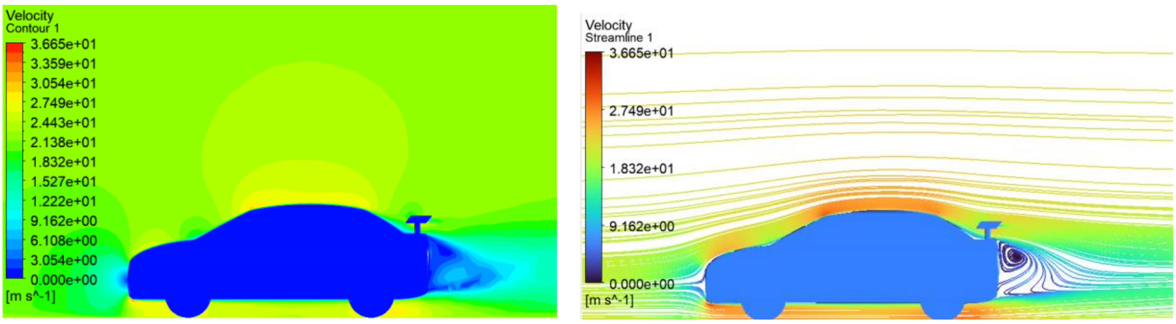

(a) (b)

Figure 5.27. (a) Velocity contour and (b) Streamline of model one at 80 km/h

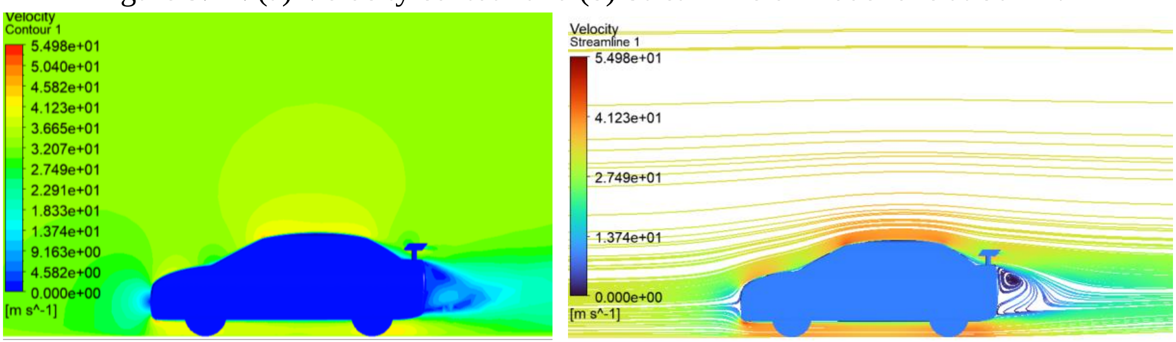

(a) (b)

Figure 5.28. (a) Velocity contour and (b) Streamline of model one at 120 km/h

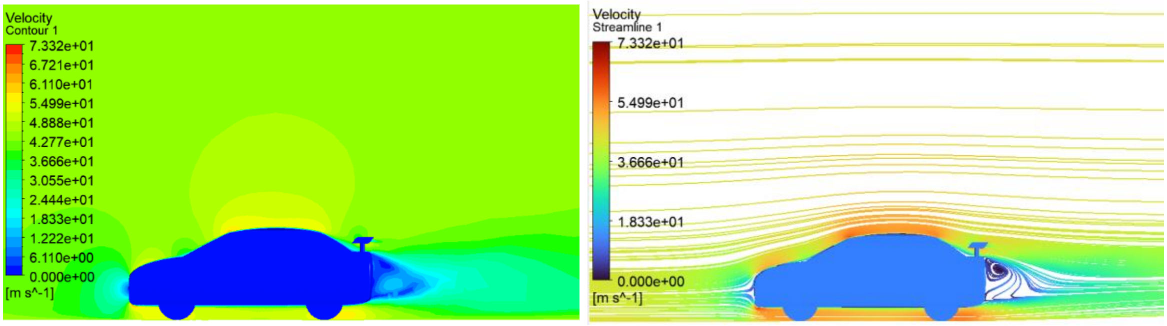

(a) (b)

Figure 5.29. (a) Velocity contour and (b) Streamline of model one at 160 km/h

The flow of air over the car body causes a velocity distribution, leading to aerodynamic loads on the body of the model one. The velocity distribution shows the amount of velocity at various region of the model one. Due to the airflow separation seen in Figures 5.27–5.29, the airflow becomes turbulent, resulting in the formation of a lower pressure area toward the rear of the vehicle. Because of the difference in air speed on the upper and lower sides of the spoiler, there is a low-pressure zone below it and a high-pressure zone above it. Downforce occurs when the pressure differential forces the trunk downward.

Table 5.4. Comparison between the baseline model and model one

Models	Speed (Km/h)	C_d	Average c_d value	C_d % change	C_l	Average c_l value	C_l % change
Baseline model	80	0.3283	0.3270	-	-0.1390	-0.1436	-
	120	0.3270			-0.1441		
	160	0.3256			-0.1477		
Model one	80	0.3414	0.3399	+3.95	-0.2923	-0.3	-108.9
	120	0.3397			-0.3013		
	160	0.3387			-0.3066		

As shown in Table 5.4, the comparison shows when adding a rear-end wing-type spoiler increases the drag coefficient but reduces lift. This indicates that while drag may increase slightly by 3.95% and the lift decreases significantly by 108.9%, it enhances stability and handling during acceleration. Therefore, at a 0-degree angle of attack, an increase in downforce can be achieved.

5.4 Model two (Baseline model with a 10-degree spoiler inclination)

5.4.1 Drag and Lift Coefficients

The convergence history of the drag and lift coefficients for model two (baseline model with rear wing type spoiler at 10-degree angle of inclination) at three different speeds (80, 120, and 160 km/h) is shown in Figures 5.30–5.35.

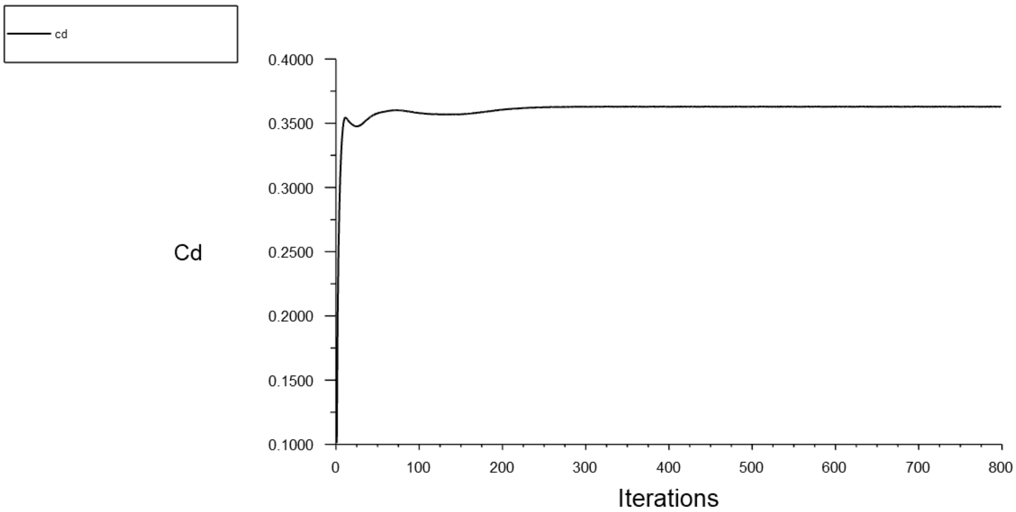

Figure 5.30. Drag coefficient convergence history of model two at 80 km/h

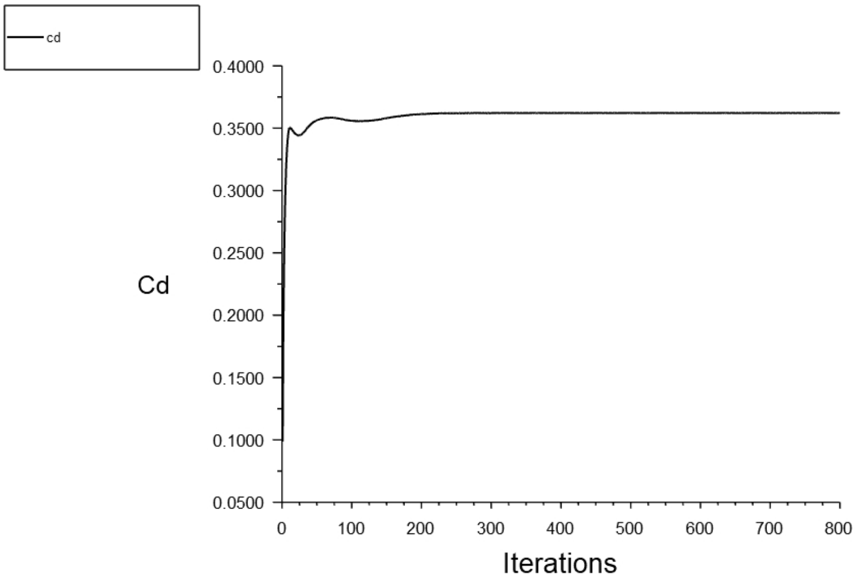

Figure 5.31. Drag coefficient convergence history of model two at 120 km/h

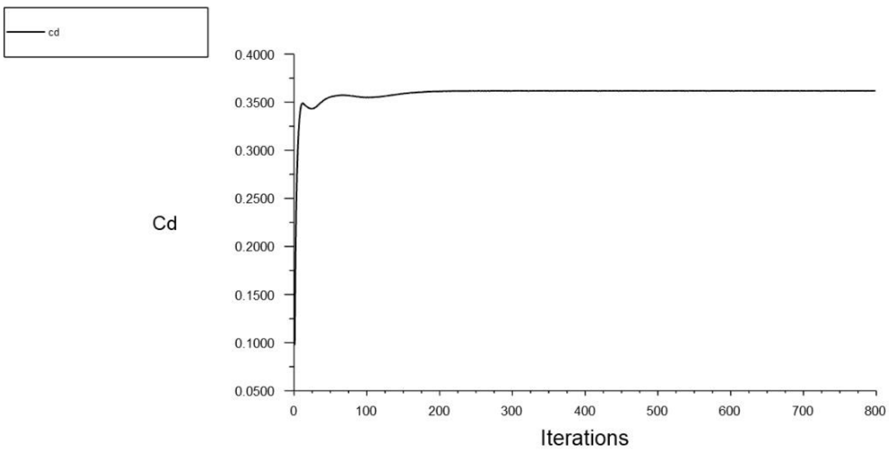

Figure 5.32. Drag coefficient convergence history of model two at160 km/h

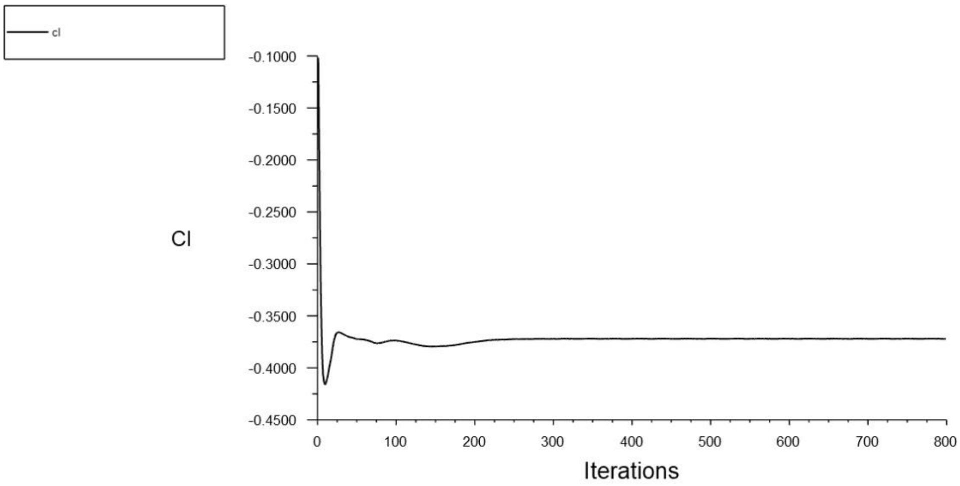

Figure 5. 33. Lift coefficient convergence history of model two at 80 km/h

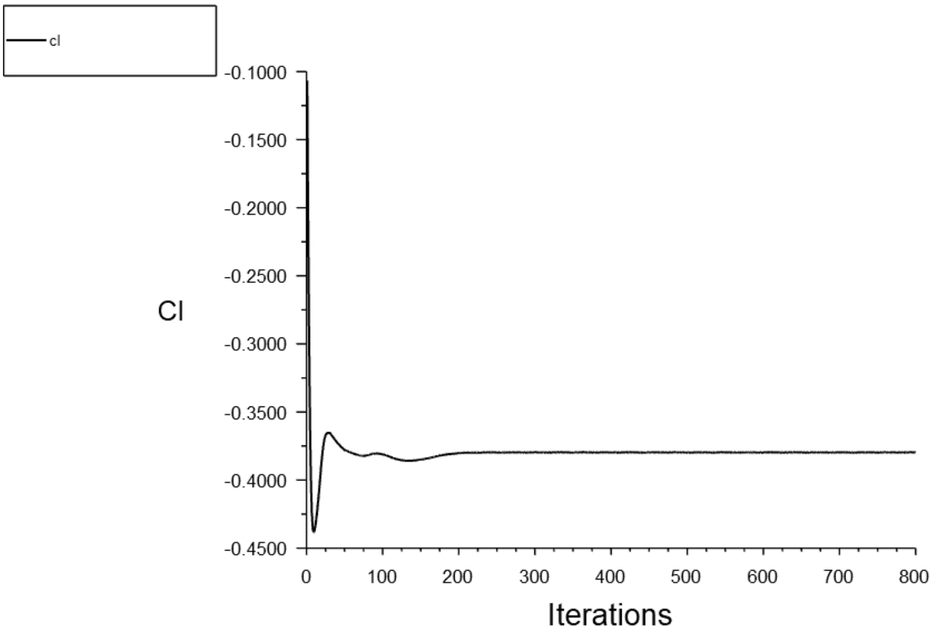

Figure 5.34. Lift coefficient convergence history of model two at 120 km/h

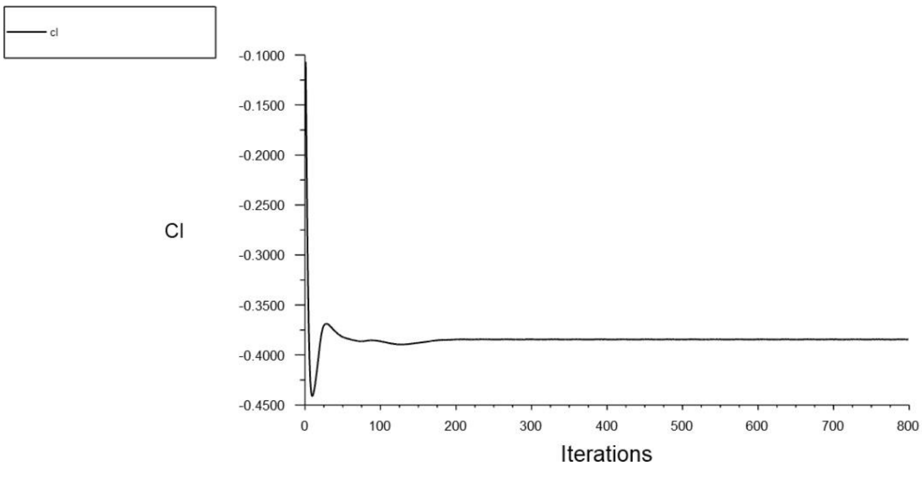

Figure 5.35. Lift coefficient convergence history of model two at 160 km/h

The drag and lift coefficient convergence histories in Figures 4.30–4.35 above show that both parameters converged well before the 800th iteration.

Table 5.5. Drag and lift coefficient of the model two at various speeds

	Speed		C_d	C_l
	Km/h	m/s		
Model two	80	22.222	0.3629	-0.3722
	120	33.333	0.3622	-0.3797
	160	44.444	0.3618	-0.3846

The drag and lift coefficients of the model two examined at different speeds are summarized in Table 5.5 above. The drag coefficient and lift coefficient of model two decreased with increasing speed. It suggesting decreasing aerodynamic resistance and increased vehicle stability at high speeds.

5.4.2 Pressure contour

Figures 5.36–5.38 show the pressure contour on the symmetry plane and on the body of the model two at three different velocities (80, 120, and 160 km/h).

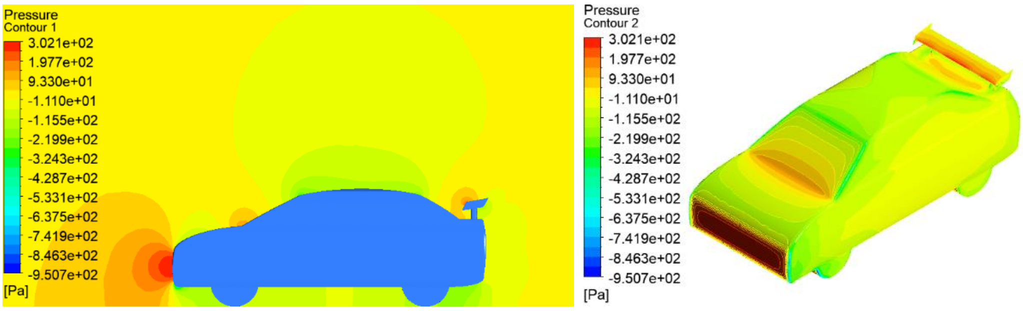

(a) (b)

Figure 5.36. Pressure contour (a) on symmetry plane (b) on body of model two at 80 km/h

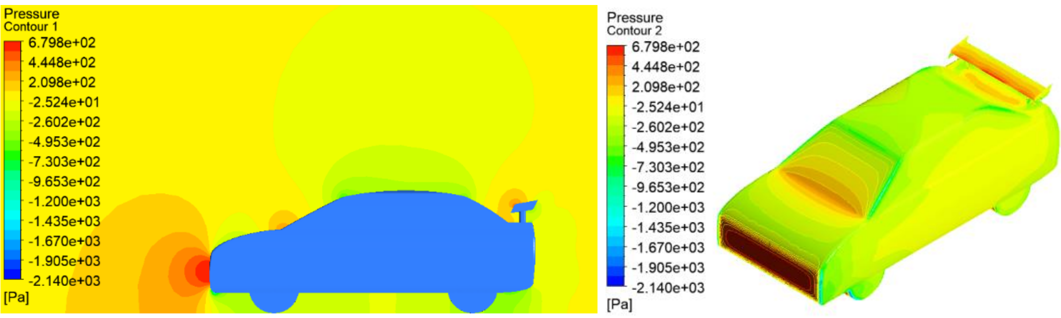

(a) (b)

Figure 5.37. Pressure contour (a) on symmetry plane (b) on body of model two at 120 km/h

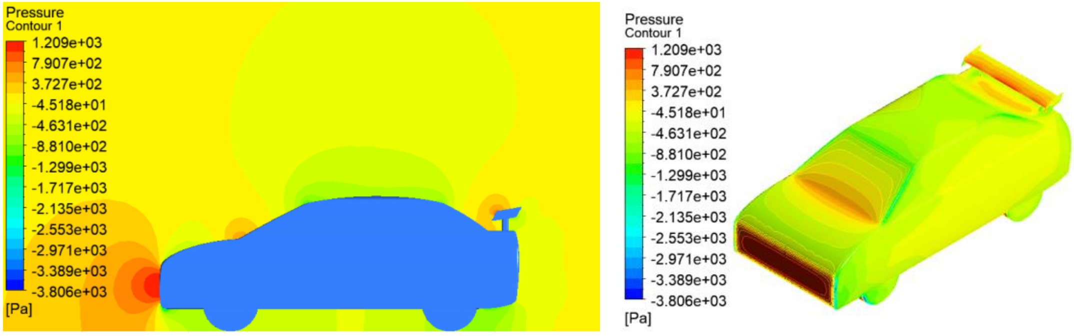

(a) (b)

Figure 5.38. Pressure contour (a) on symmetry plane (b) on body of model two at 160 km/h

The level of pressure influence on the car's surface is shown in Figures 5.36–5.38, indicated by the contour of the static pressure distribution. The contour of the pressure distribution in Figures 5.36–5.38 is more similar to model one. However, we can see that the pressure around the rear wing-type spoiler increased due to an increase in its angle of inclination. When the speed of a vehicle increases, the maximum pressure also increases on the vehicle body and around the rear wing-type spoiler.

5.4.3 Velocity contour and streamline

Figures 5.39–5.41 show the velocity contour and streamline flow of a model two at three different velocities (80, 120, and 160 km/h) on the symmetry plane.

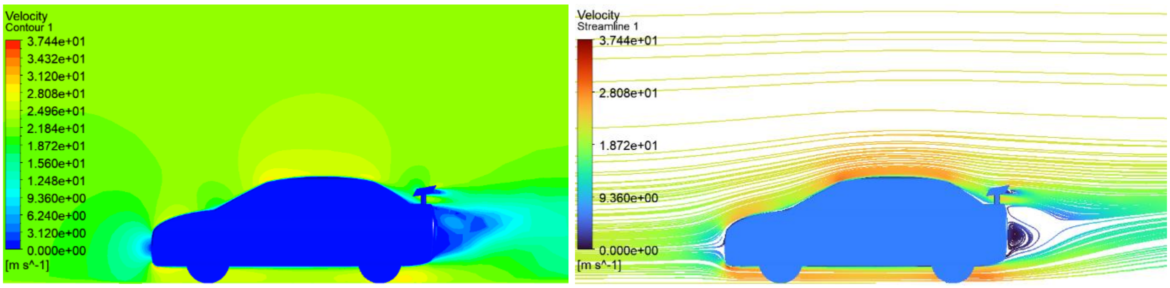

(a) (b)

Figure 5.39. (a) Velocity contour and (b) Streamline of model two at 80 km/h

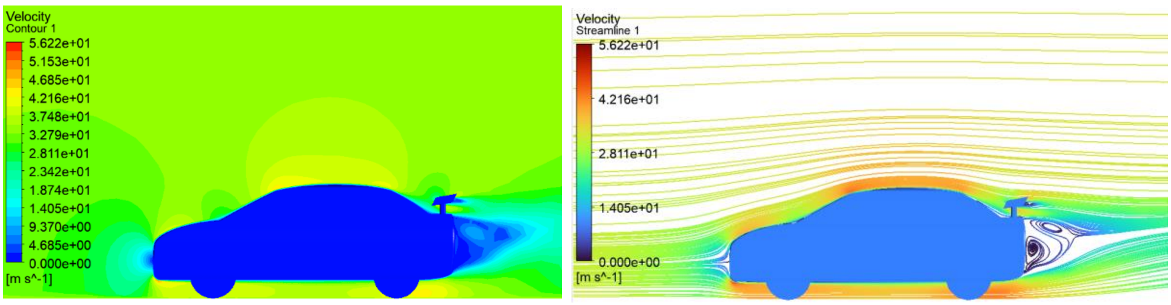

(a) (b)

Figure 5.40. (a) Velocity contour and (b) Streamline of model two at 120 km/h

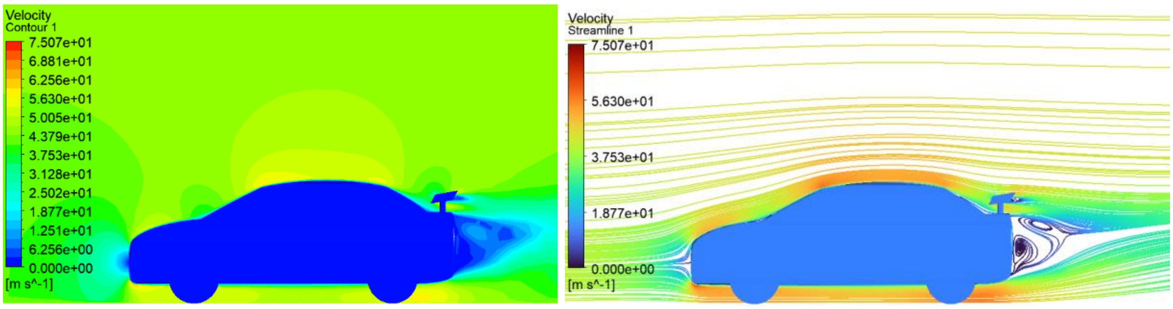

(a) (b)

Figure 5. 41. (a) Velocity contour and (b) Streamline of model two at 160 km/h

The flow of air over the car body causes a velocity distribution, leading to aerodynamic loads on the body of the model two. The velocity distribution in Figure 5.39–5.41 shows the amount of velocity at various region of the model two.

5.5 Model three (Baseline model with a 20-degree spoiler inclination)

5.5.1 Drag and Lift Coefficients

The convergence history of the drag and lift coefficients for model three (baseline model with rear wing type spoiler at 20 degree angle of inclination) at three different speeds (80, 120, and 160 km/h) is shown in Figures 5.42–5.47.

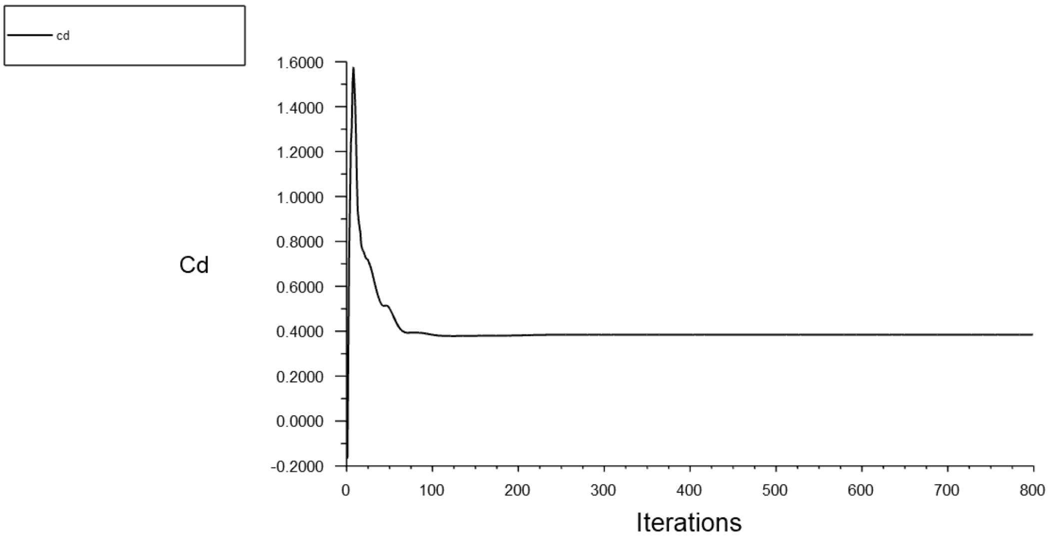

Figure 5.42. Drag coefficient convergence history of model three at 80 km/h

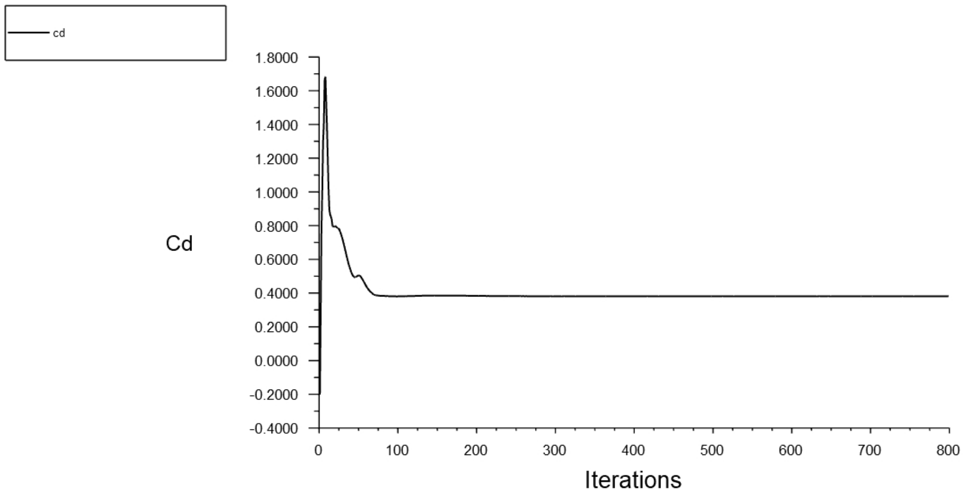

Figure 5.43. Drag coefficient convergence history of model three at 120 km/h

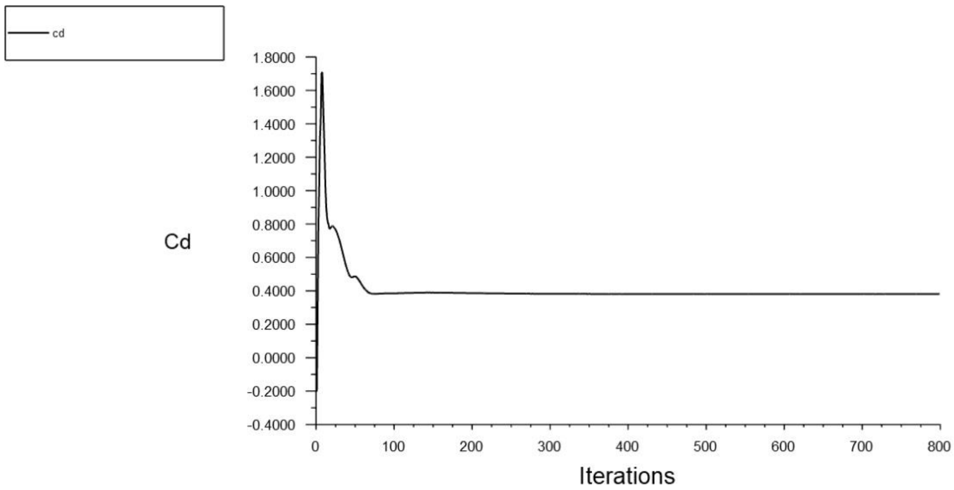

Figure 5.44. Drag coefficient convergence history of model three at 160 km/h

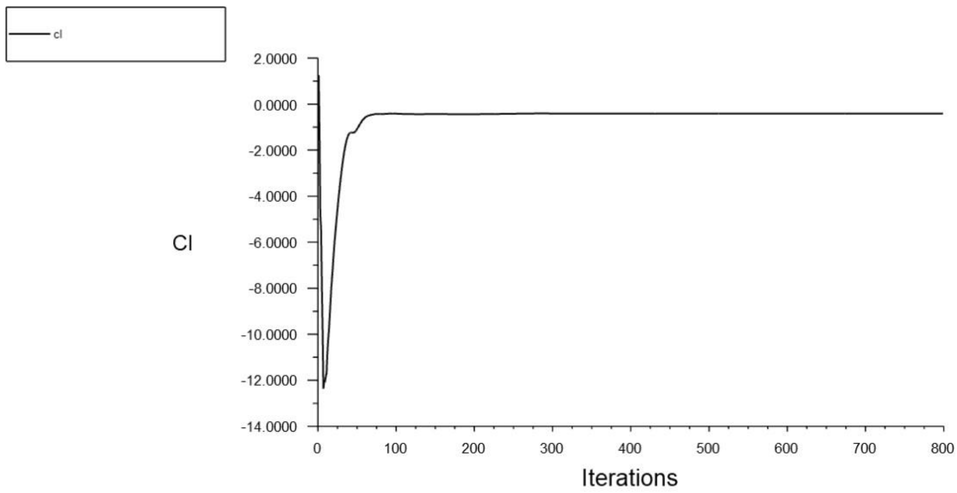

Figure 5.45. Lift coefficient convergence history of model three at 80 km/h

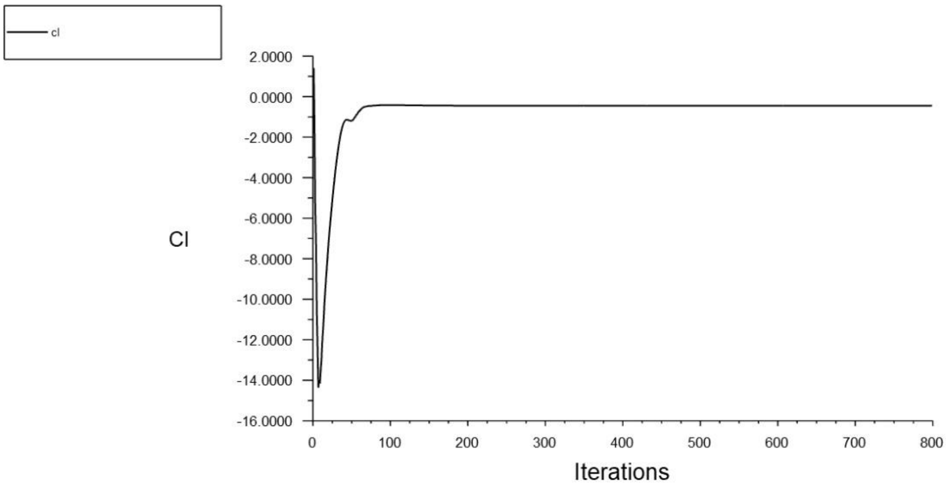

Figure 5.46. Lift coefficient convergence history of model three at 120 km/h

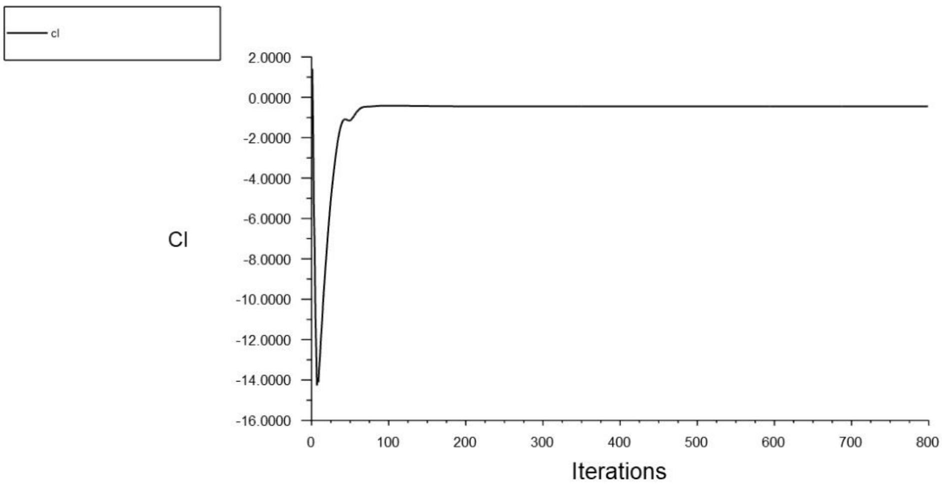

Figure 5.47. Lift coefficient convergence history of model three at 160 km/h

The drag and lift coefficient convergence histories in Figures 5.42–5.47 above show that both parameters converged well before the 800th iteration.

Table 5.6. Drag and lift coefficient of the model three at various speeds

Model	Speed		C_d	C_l
	Km/h	m/s		
Model three	80	22.222	0.3845	-0.4072
	120	33.333	0.3808	-0.4495
	160	44.444	0.3813	-0.4546

The drag and lift coefficients of the model three examined at different speeds are summarized in Table 5.6 above. The drag coefficient and lift coefficient of model three decreased with increasing speed. It suggesting decreasing aerodynamic resistance and increased vehicle stability at high speeds.

5.5.2 Pressure contour

Figures 5.48–5.50 show the pressure contour on the symmetry plane and on the body of the model three at three different velocities (80, 120, and 160 km/h).

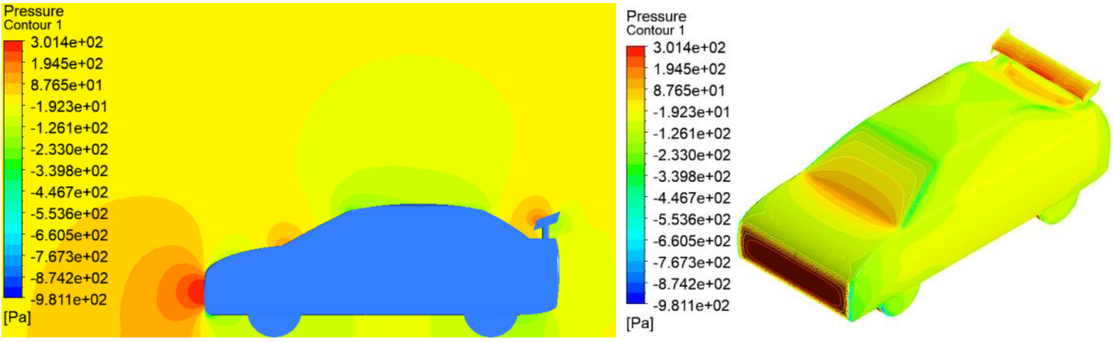

(a) (b)

Figure 5.48. Pressure contour (a) on symmetry plane (b) on body of model three at 80 km/h

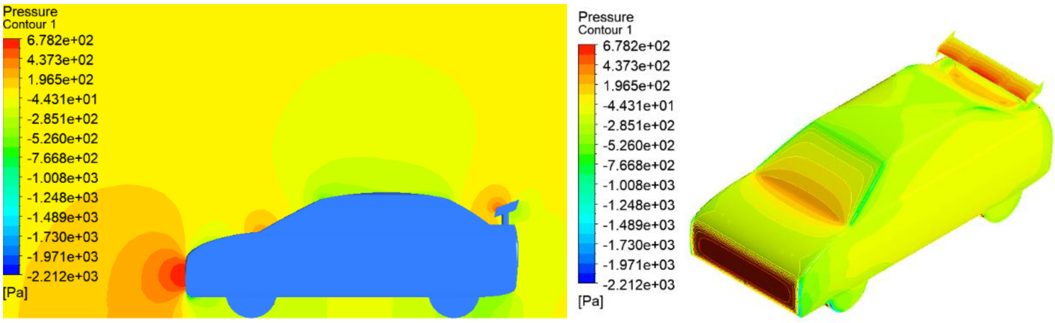

(a) (b)

Figure 5.49. Pressure contour (a) on symmetry plane (b) on body of model three at 120 km/h

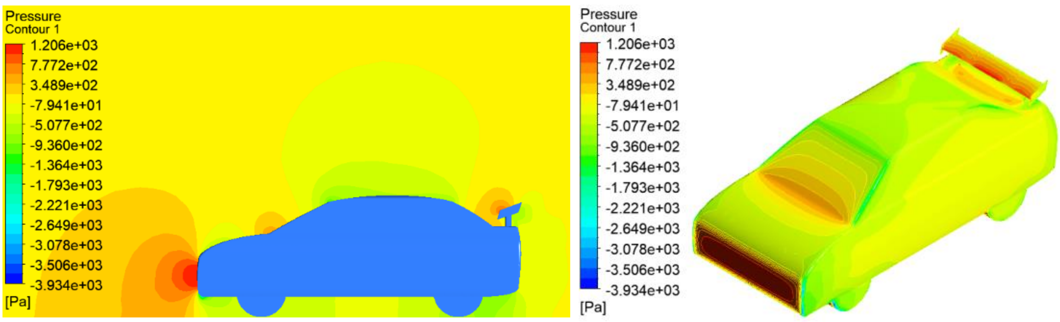

(a) (b)

Figure 5.50. Pressure contour (a) on symmetry plane (b) on body of model three at 160 km/h

The level of pressure influence on the car's surface is shown in Figures 4.48–4.50, indicated by the contour of the static pressure distribution. The contour of the pressure distribution in Figures 5.48–5.50 is more similar to model one and model two. However, we can see that the pressure around the rear wing-type spoiler increased due to an increase in its angle of inclination. When the speed of a vehicle increases, the maximum pressure also increases on the vehicle body and around the rear wing-type spoiler.

5.5.3 Velocity contour and streamline

Figures 5.51–5.53 show the velocity contour and streamline flow of a model three at three different velocities (80, 120, and 160 km/h) on the symmetry plane.

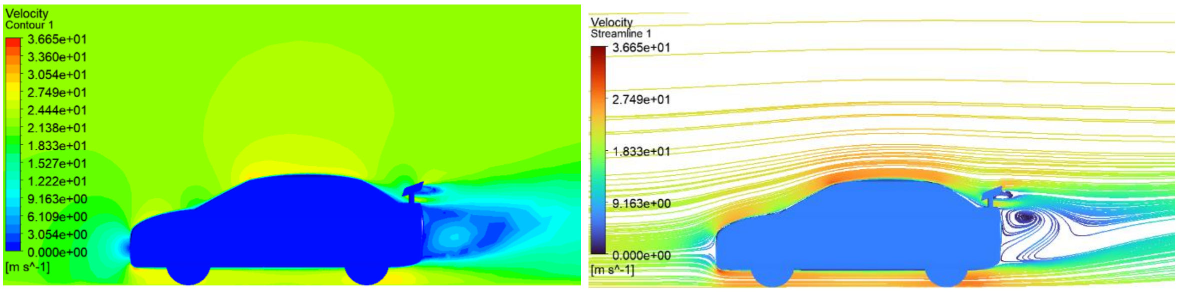

(a) (b)

Figure 5.51. (a) Velocity contour and (b) Streamline of model three at 80 km/h

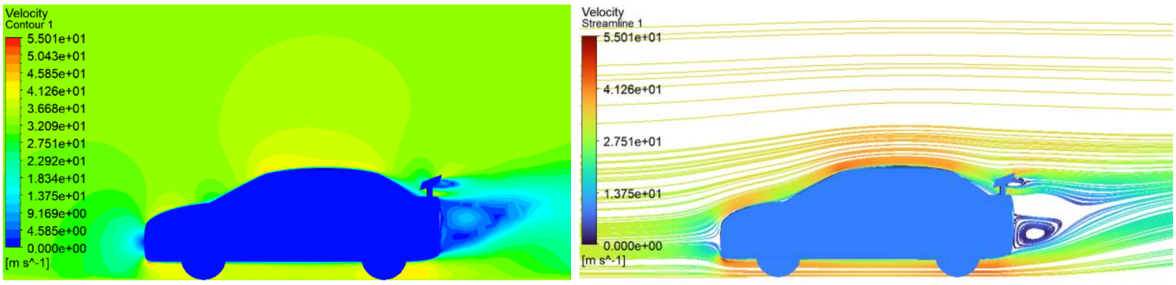

(a) (b)

Figure 5.52. (a) Velocity contour and (b) Streamline of model three at 115 km/h

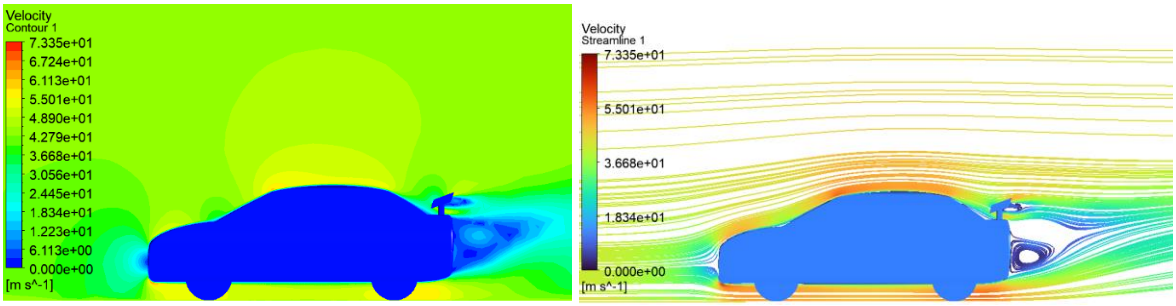

(a) (b)

Figure 5.53. (a) Velocity contour and (b) Streamline of model three at 160 km/h

The flow of air over the car body causes a velocity distribution, leading to aerodynamic loads on the body of the model three as shown in Figure 5.51–5.53.

5.6 Model four (Baseline model with a 30-degree spoiler inclination)

5.6.1 Drag and Lift Coefficients

The convergence history of the drag and lift coefficients for model four (baseline model with rear wing type spoiler at 30 degree angle of inclination) at three different speeds (80, 120, and 160 km/h) is shown in Figures 5.54–5.59.

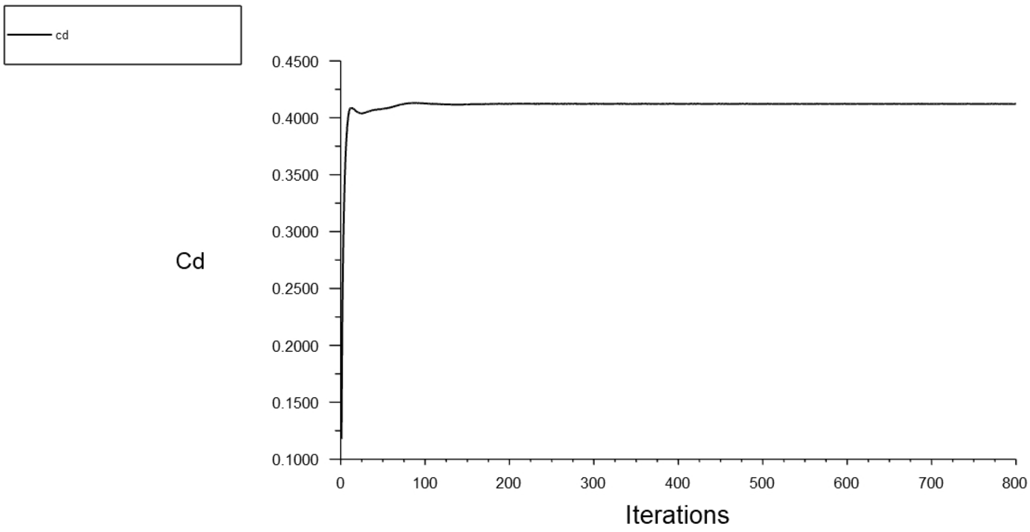

Figure 5.54. Drag coefficient convergence history of model four at 80 km/h

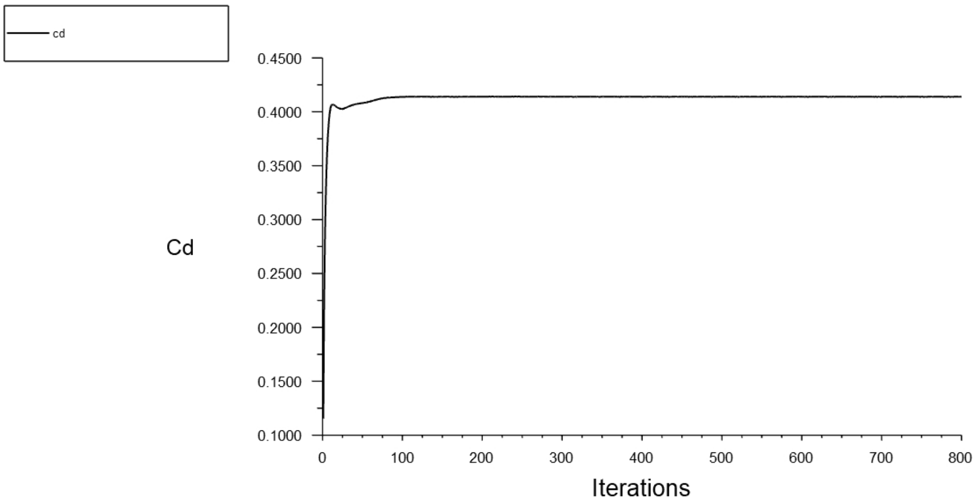

Figure 5.55. Drag coefficient convergence history of model four at 120 km/h

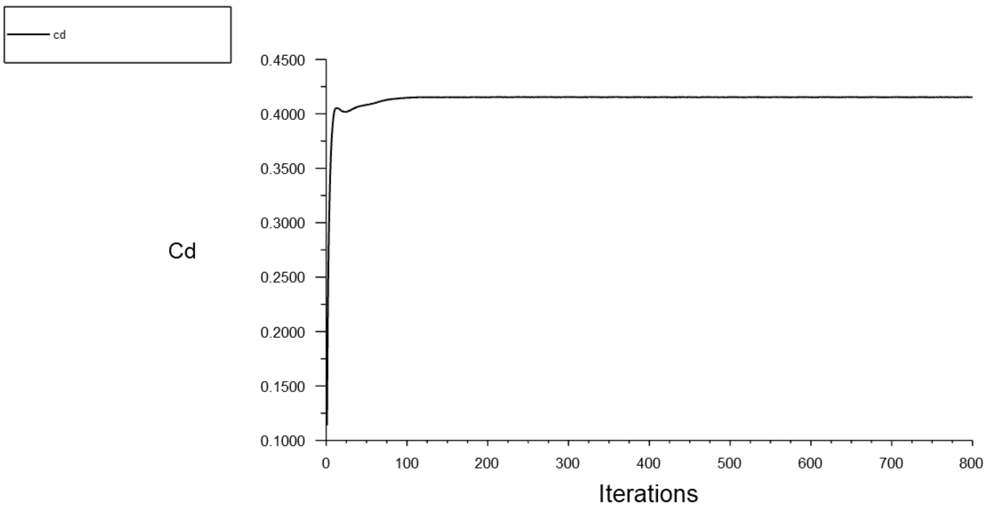

Figure 5.56. Drag coefficient convergence history of model four at 160 km/h

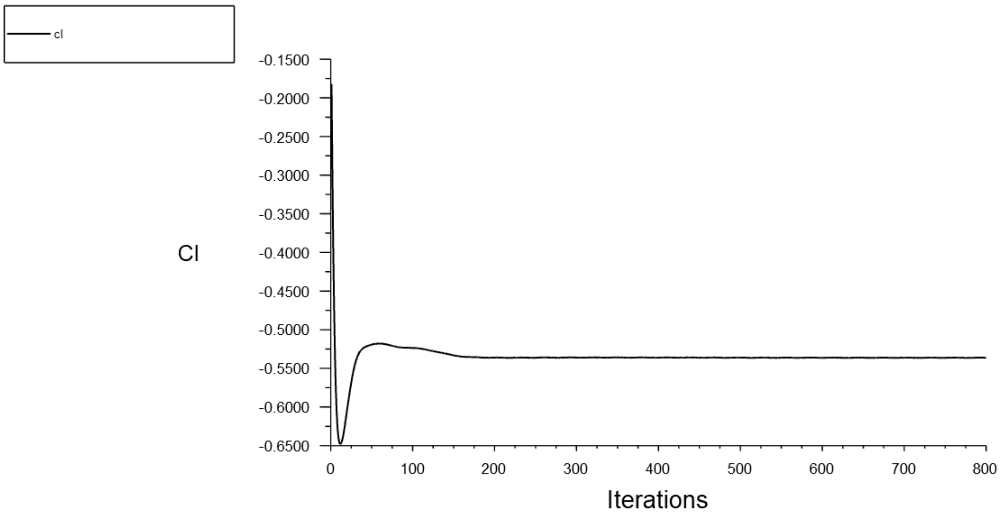

Figure 5.57. Lift coefficient convergence history of model four at 80 km/h

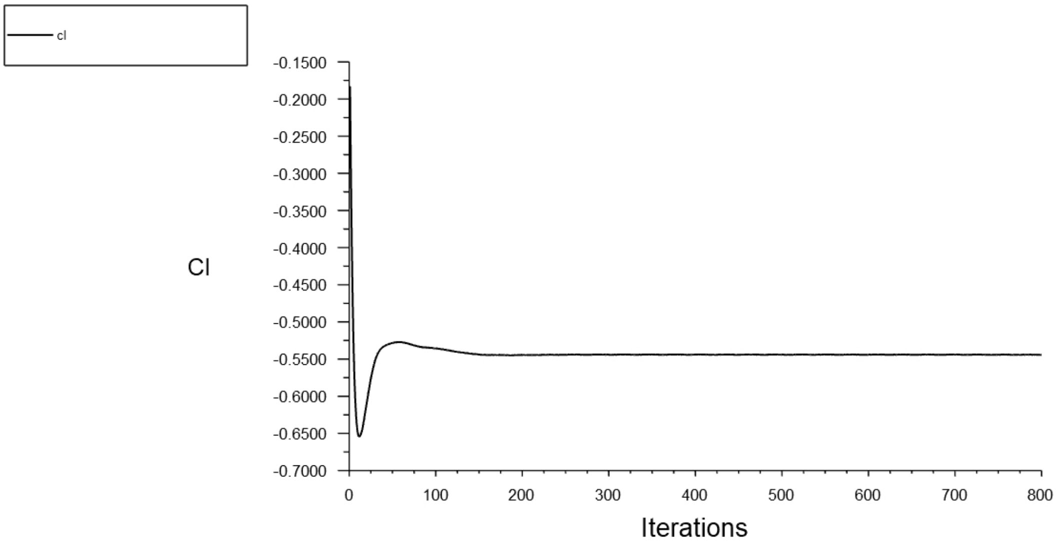

Figure 5.58. Lift coefficient convergence history of model four at 120 km/h

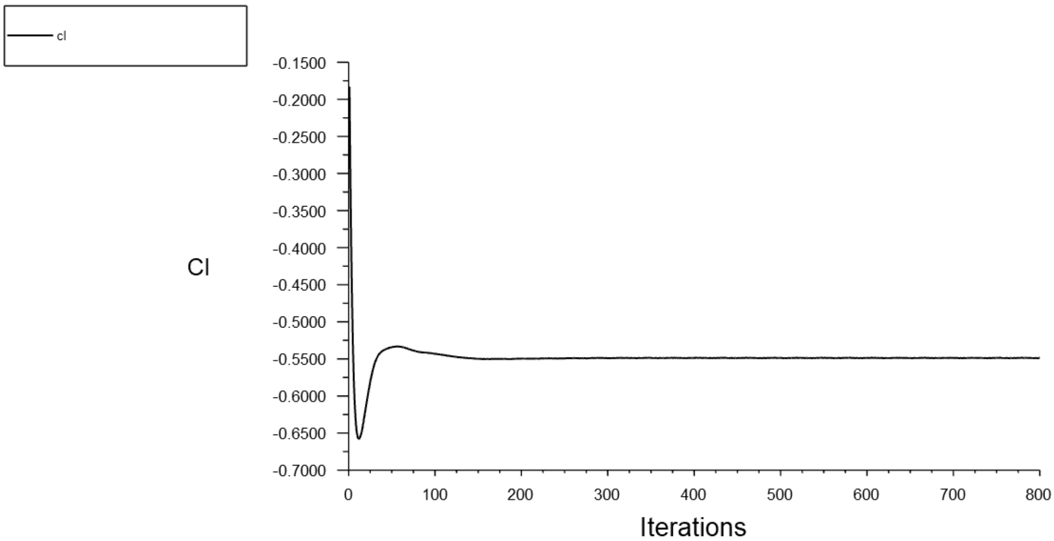

Figure 5.59. Lift coefficient convergence history of model four at 160 km/h

The drag and lift coefficient convergence histories in Figures 5.54–5.59 above show that both parameters converged well before the 800th iteration.

Table 5. 7. Drag and lift coefficient of the model four at various speeds

Model	Speed		C_d	C_l
	Km/h	m/s		
Model four	80	22.222	0.4123	-0.5362
	120	33.333	0.4140	-0.5442
	160	44.444	0.4153	-0.5488

The drag and lift coefficients of the model four examined at different speeds are summarized in Table 5.7 above. The drag coefficient of model four increased with increasing speed, suggesting increased aerodynamic resistance. While the lift coefficient decreased, this led to increased vehicle stability at high speeds.

5.6.2 Pressure contour

Figures 5.60–5.62 show the pressure contour on the symmetry plane and on the body of the model four at three different velocities (80, 120, and 160 km/h).

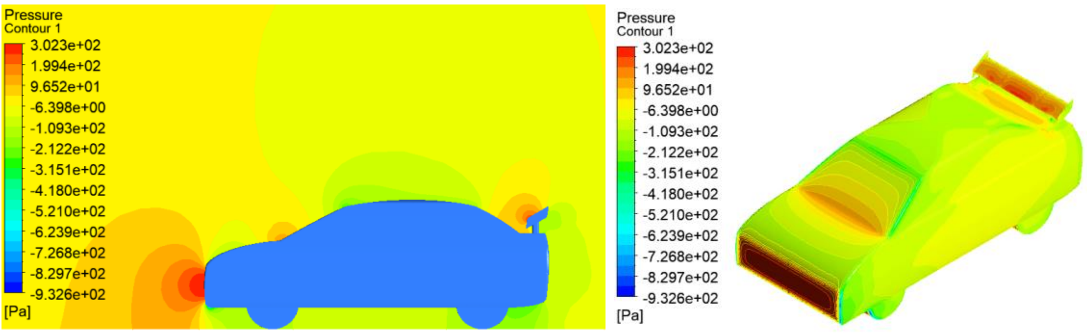

(a) (b)

Figure 5.60. Pressure contour (a) on symmetry plane (b) on body of model four at 80 km/h

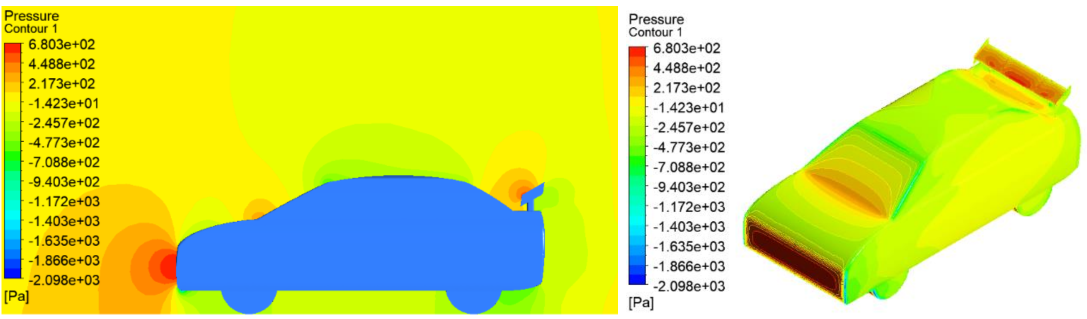

(a) (b)

Figure 5.61. Pressure contour (a) on symmetry plane (b) on body of model four at 120 km/h

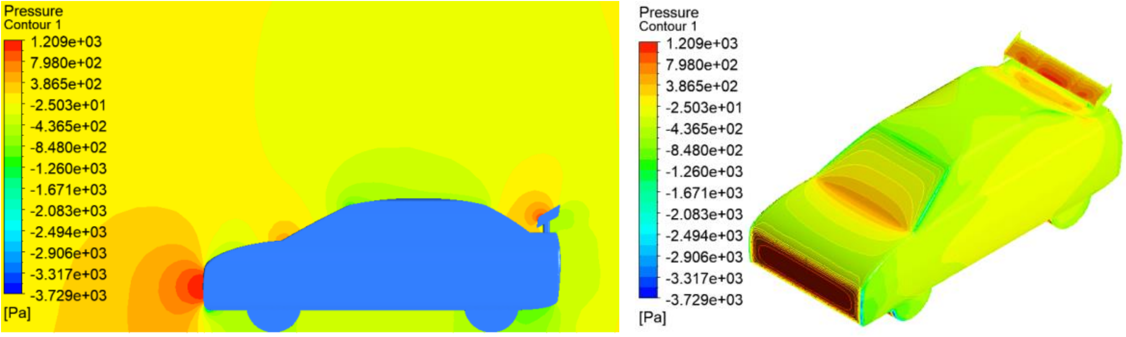

(a) (b)

Figure 5.62. Pressure contour (a) on symmetry plane (b) on body of model four at 160 km/h

The level of pressure influence on the car's surface is shown in Figures 5.60–5.62, indicated by the contour of the static pressure distribution. The contour of the pressure distribution in Figures 5.60–5.62 is more similar to the above models. However, we can see that the pressure around the rear wing-type spoiler increased due to an increase in its angle of inclination. When the speed of a vehicle increases, the maximum pressure also increases on the vehicle body and around the rear wing-type spoiler.

5.6.3 Velocity contour and streamline

Figures 5.63–5.65 show the velocity contour and streamline flow of a model four at three different velocities (80, 120, and 160 km/h) on the symmetry plane.

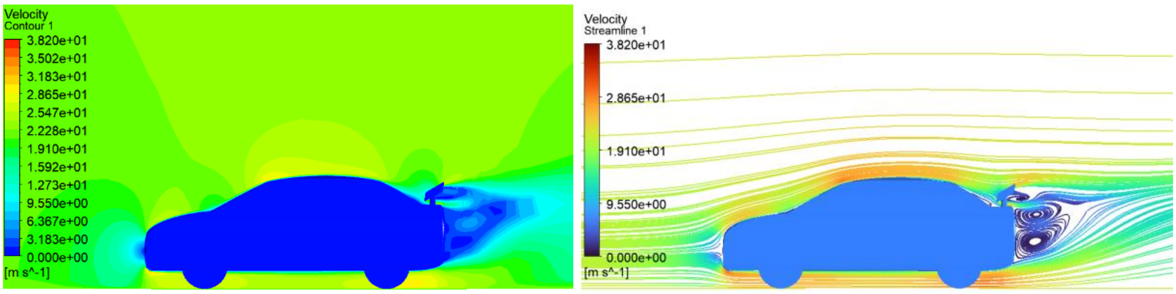

(a) (b)

Figure 5.63. (a) Velocity contour and (b) Streamline of model four at 80 km/h

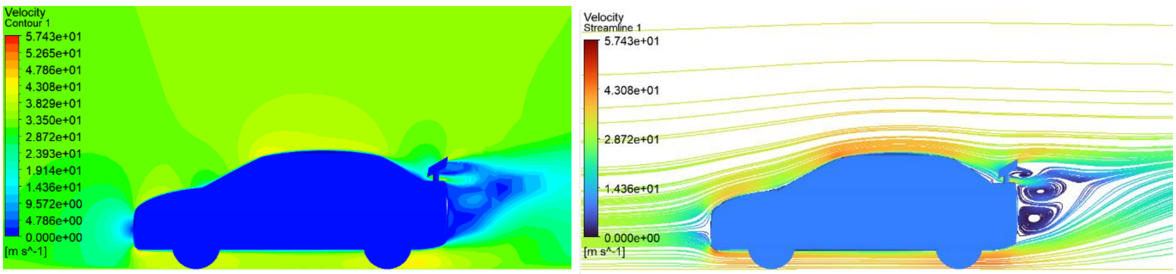

(a) (b)

Figure 5.64. (a) Velocity contour and (b) Streamline of model four at 120 km/h

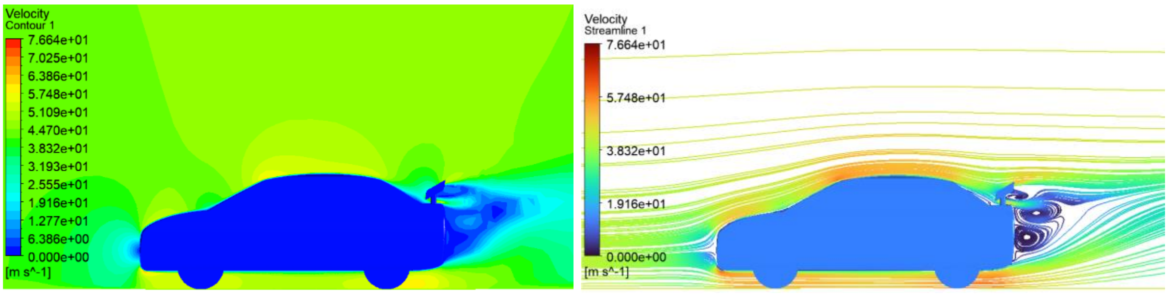

(a) (b)

Figure 5.65. (a) Velocity contour and (b) Streamline of model four at 160 km/h

The flow of air over the car body causes a velocity distribution, leading to aerodynamic loads on the body of the model four. The velocity distribution in Figure 5.63–5.65 shows the amount of velocity at various region of the model four.

5.7 Model five (Baseline model with a 40-degree spoiler inclination)

5.7.1 Drag and Lift Coefficients

The convergence history of the drag and lift coefficients for model five (baseline model with rear wing type spoiler at 40 degree angle of inclination) at three different speeds (80, 120, and 160 km/h) is shown in Figures 5.66–5.71.

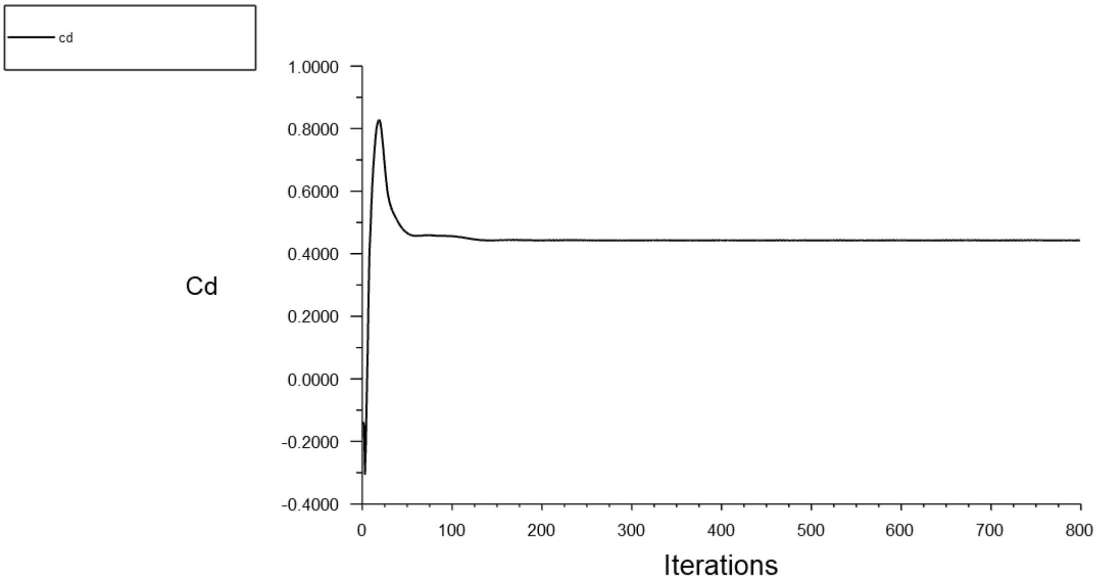

Figure 5.66. Drag coefficient convergence history of model five at 80 km/h

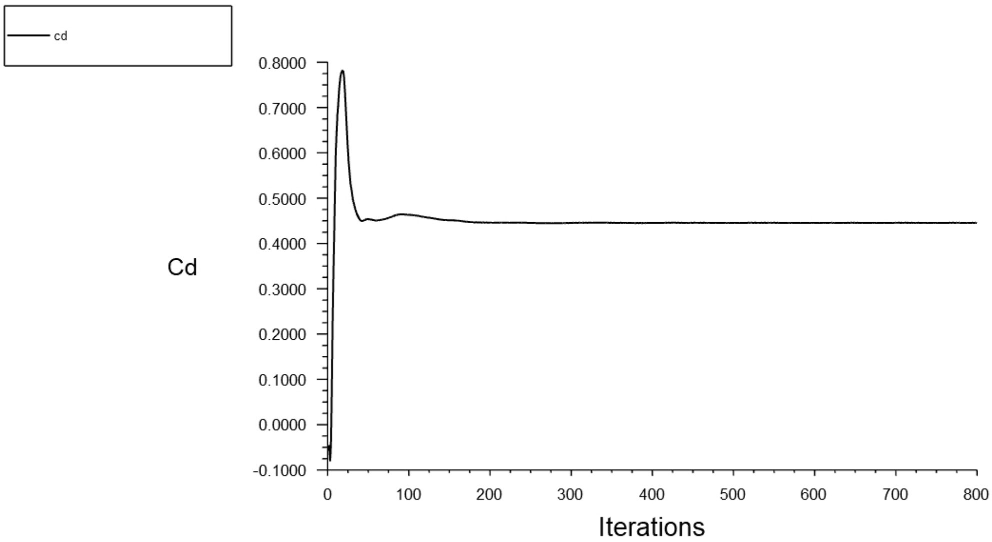

Figure 5.67. Drag coefficient convergence history of model five at 120 km/h

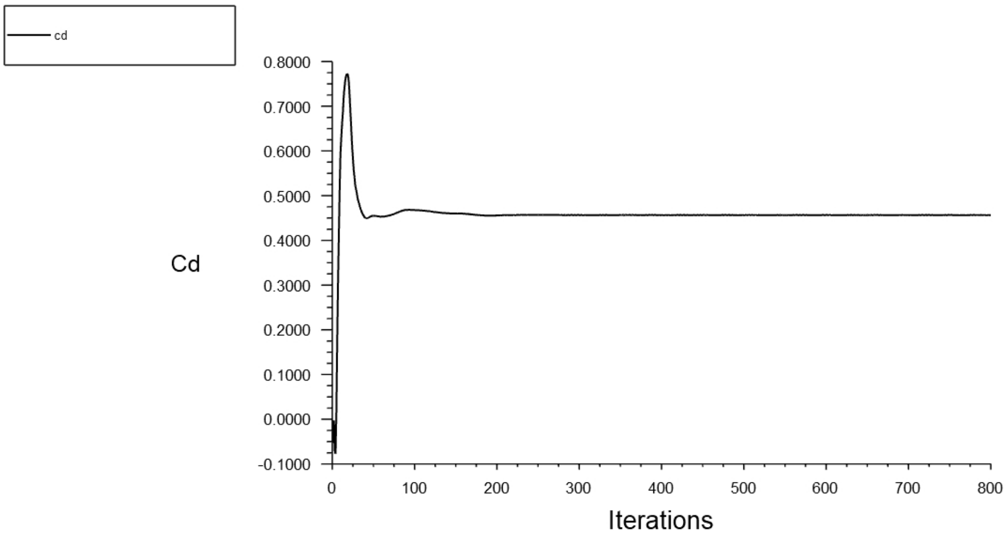

Figure 5.68. Drag coefficient convergence history of model five at 160 km/h

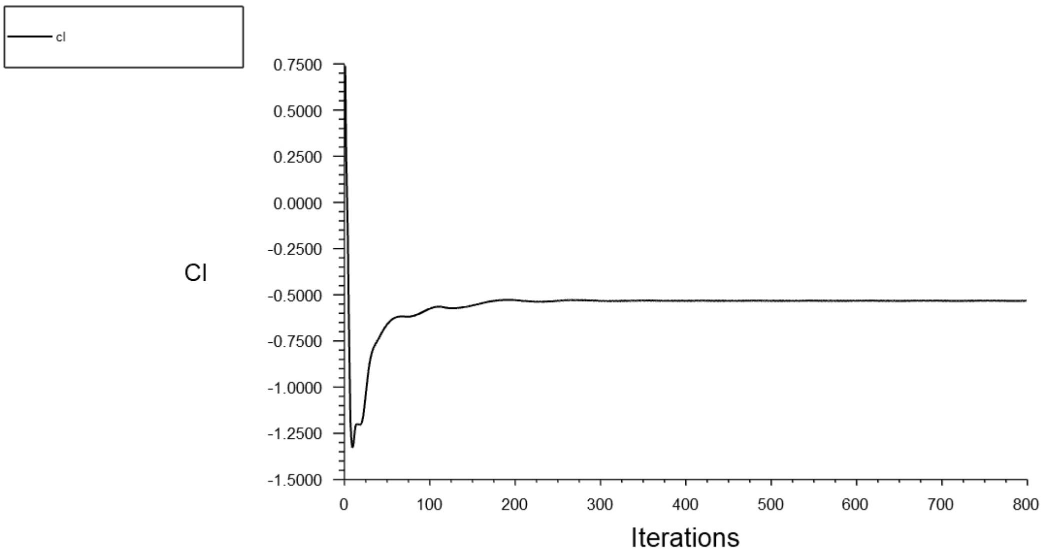

Figure 5.69. Lift coefficient convergence history of model five at 80 km/h

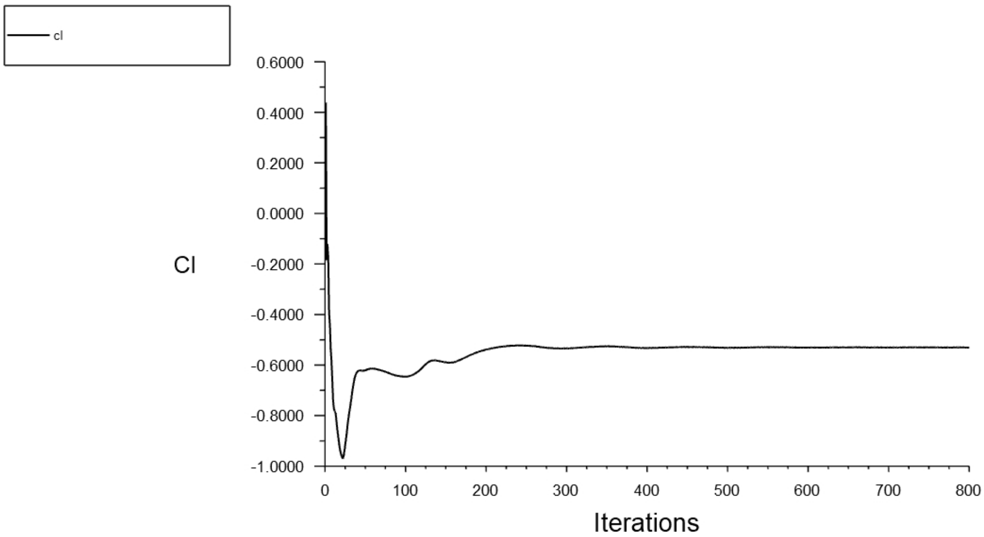

Figure 5.70. Lift coefficient convergence history of model five at 120 km/h

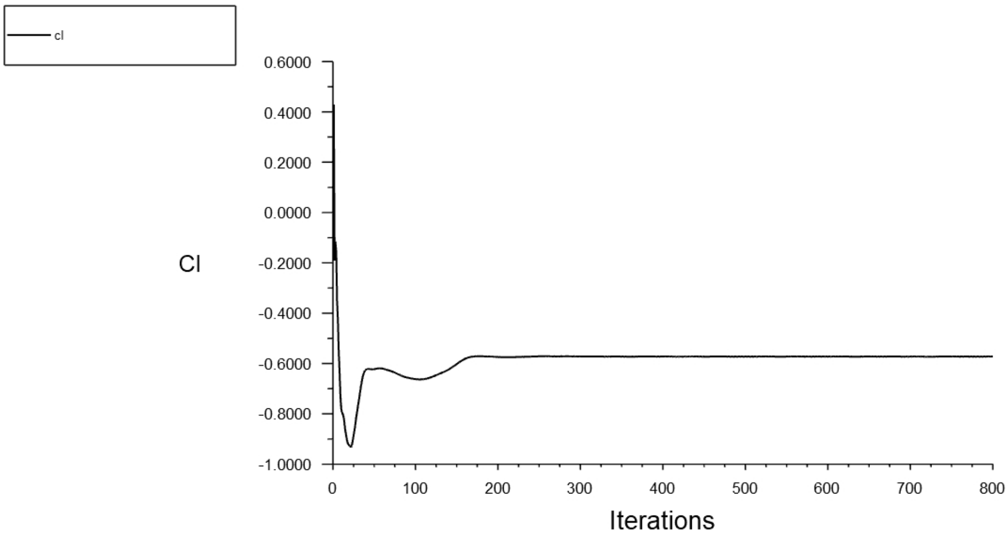

Figure 5.71. Lift coefficient convergence history of model five at 160 km/h

The drag and lift coefficient convergence histories in Figures 5.66–5.71 above show that both parameters converged well before the 800th iteration.

Table 5.8. Drag and lift coefficient of the model five at various speeds

Model	Speed		C_d	C_l
	Km/h	m/s		
Model five	80	22.222	0.4432	-0.5332
	120	33.333	0.4454	-0.5304
	160	44.444	0.4565	-0.5723

The drag and lift coefficients of a model five examined at different speeds are summarized in Table 5.8 above. The drag coefficient of model five increased with increasing speed, suggesting increased aerodynamic resistance. While the lift coefficient decreased, this led to increased vehicle stability at high speeds.

5.7.2 Pressure contour

Figures 5.72–5.74 show the pressure contour on the symmetry plane and on the body of the model five at three different velocities (80, 120, and 160 km/h).

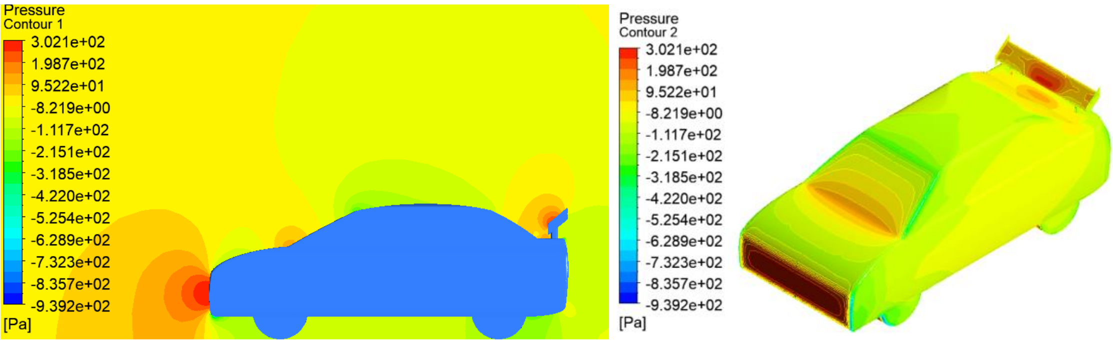

(a) (b)

Figure 5.72. Pressure contour (a) on symmetry plane (b) on body of model five at 80 km/h

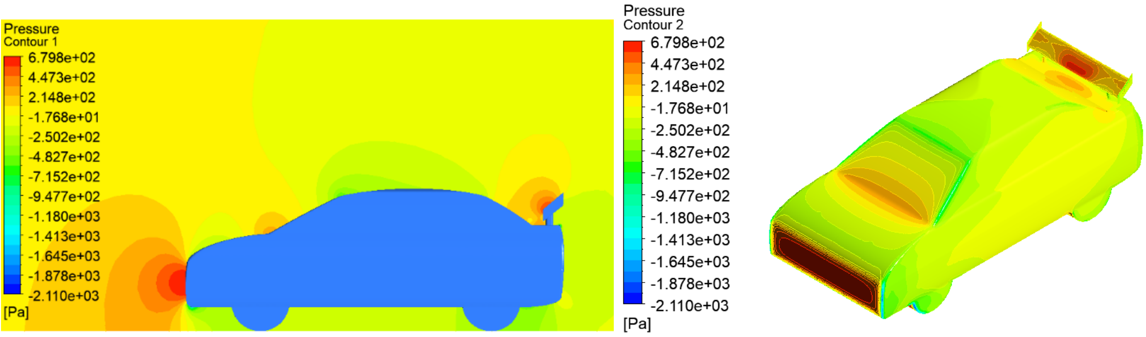

(a) (b)

Figure 5.73. Pressure contour (a) on symmetry plane (b) on body of model five at 120 km/h

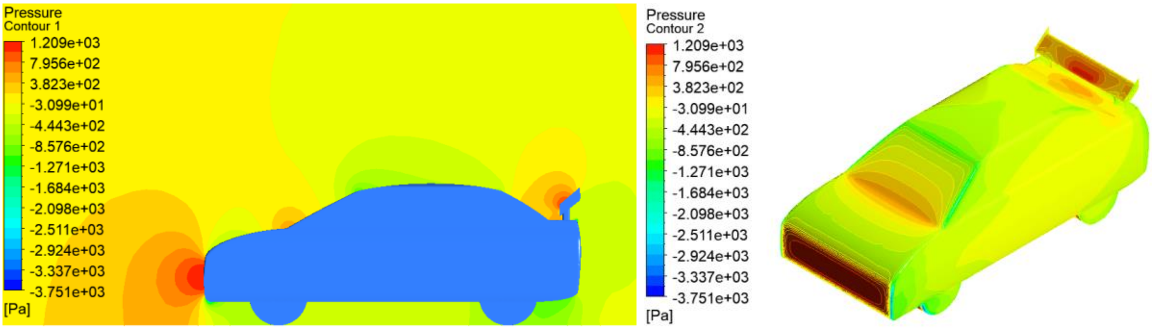

(a) (b)

Figure 5.74. Pressure contour (a) on symmetry plane (b) on body of model five at 160 km/h

The level of pressure influence on the car's surface is shown in Figures 5.72–5.74, indicated by the contour of the static pressure distribution. The contour of the pressure distribution in Figures 5.72–5.74 is more similar to the above models. However, we can see that the pressure around the rear wing-type spoiler increased due to an increase in its angle of inclination. When the speed of a vehicle increases, the maximum pressure also increases on the vehicle body and around the rear wing-type spoiler.

5.7.3 Velocity contour and streamline

Figures 5.75–5.77 show the velocity contour and streamline flow of a model five at three different velocities (80, 120, and 160 km/h) on the symmetry plane.

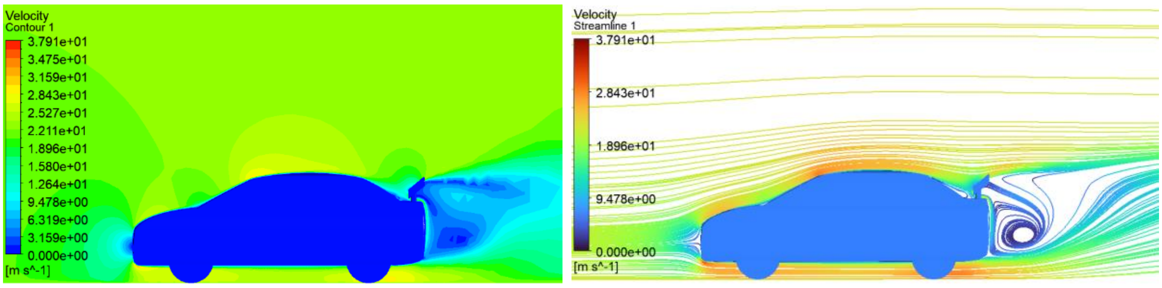

(a) (b)

Figure 5.75. (a) Velocity contour and (b) Streamline of model five at 80 km/h

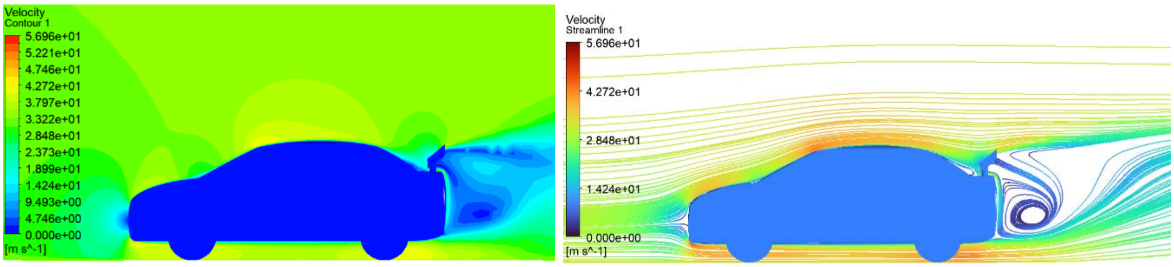

(a) (b)

Figure 5.76. (a) Velocity contour and (b) Streamline of model five at 120 km/h

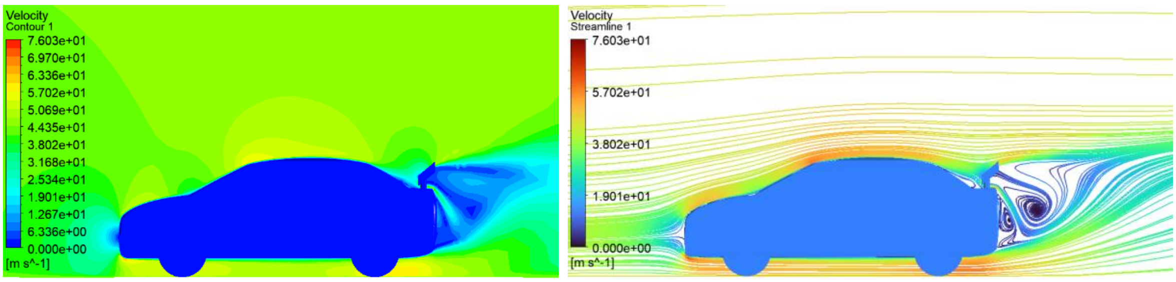

(a) (b)

Figure 5.77. (a) Velocity contour and (b) Streamline of model five at 160 km/h

The flow of air over the car body causes a velocity distribution, leading to aerodynamic loads on the body of the model five. The velocity distribution in Figure 5.75–5.77 shows the amount of velocity at various region of the model five.

5.8 Model six (Baseline model with a 50-degree spoiler inclination)

5.8.1 Drag and Lift Coefficients

The convergence history of the drag and lift coefficients for model six (baseline model with rear wing type spoiler at 50 degree angle of inclination) at three different speeds (80, 120, and 160 km/h) is shown in Figures 5.78–5.83.

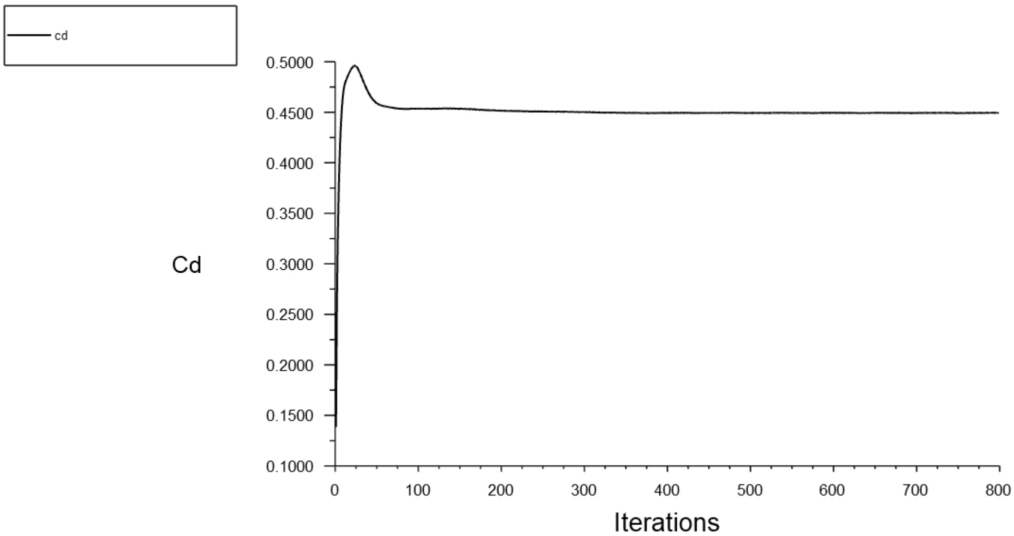

Figure 5.78. Drag coefficient convergence history of model six at 80 km/h

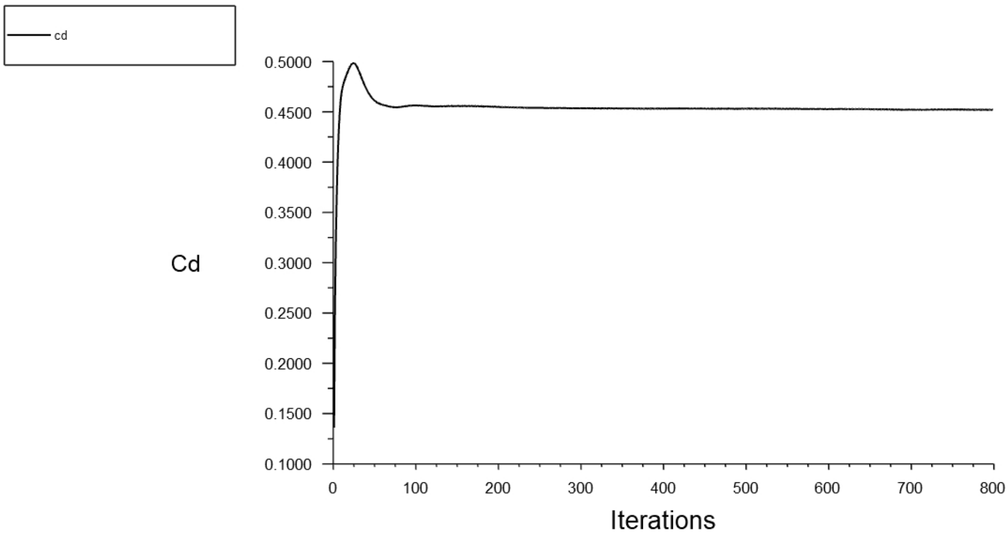

Figure 5.79. Drag coefficient convergence history of mode six at 120 km/h

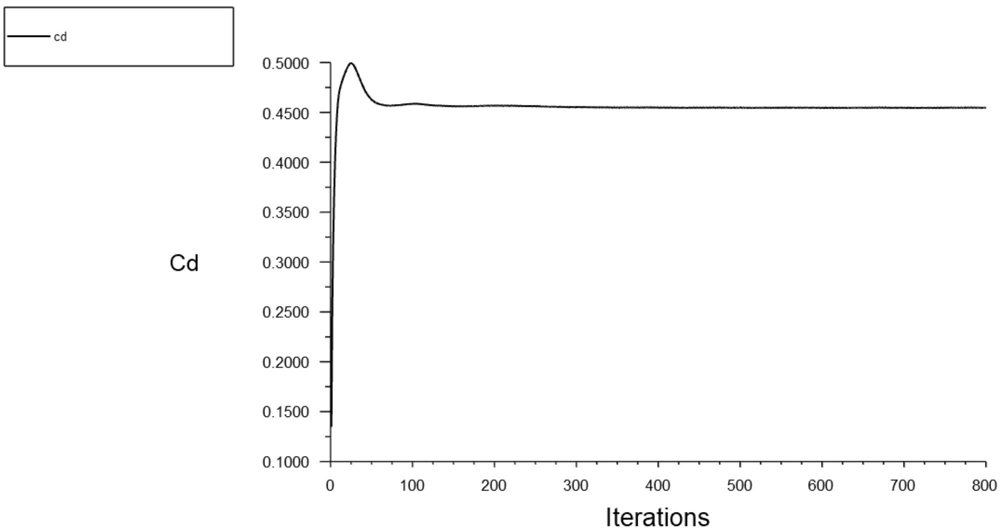

Figure 5.80. Drag coefficient convergence history of model six at 160 km/h

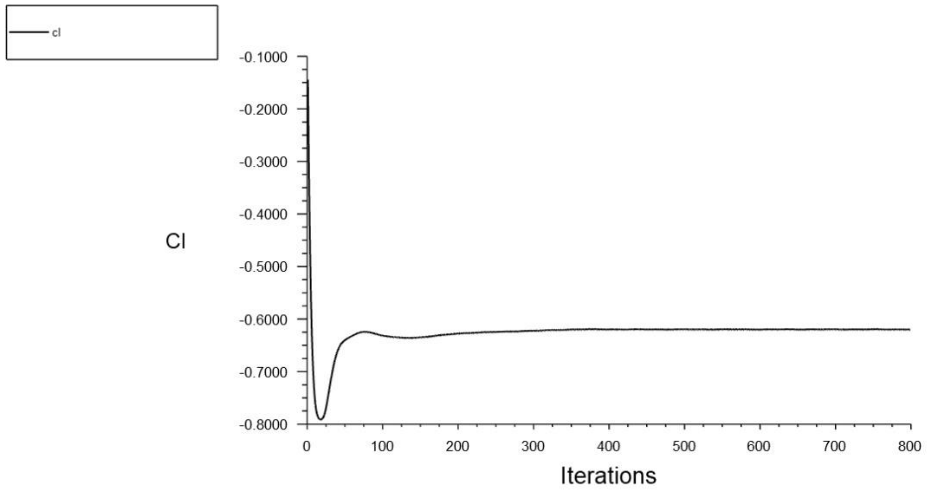

Figure 5.81. Lift coefficient convergence history of model six at 80 km/h

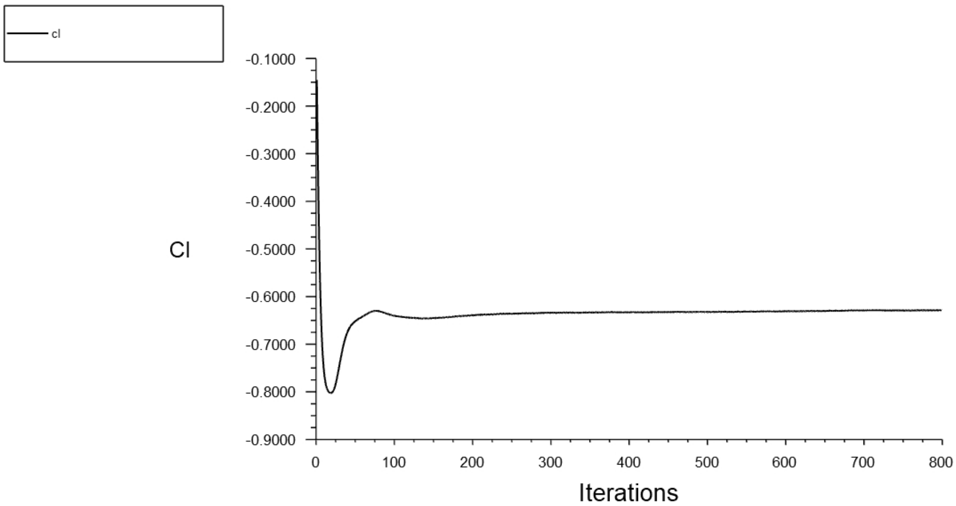

Figure 5.82. Lift coefficient convergence history of model six at 120 km/h

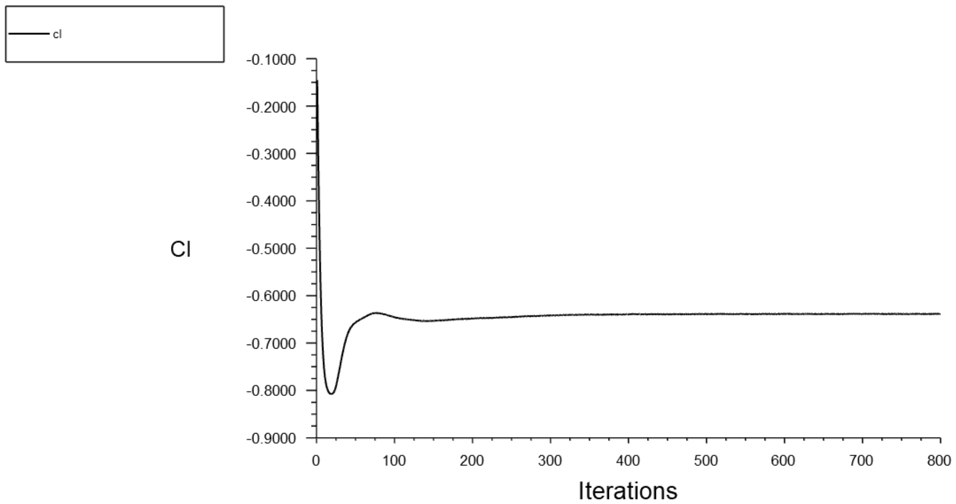

Figure 5.83. Lift coefficient convergence history of model six at 160 km/h

The drag and lift coefficient convergence histories in Figures 5.78–5.83 above show that both parameters converged well before the 800th iteration.

The drag and lift coefficients of a model six examined at different speeds are summarized in Table 5.9. The drag coefficient of model six increased with increasing speed, suggesting increased aerodynamic resistance. While the lift coefficient decreased, this led to increased vehicle stability at high speeds.

Table 5.9. Drag and lift coefficient of the model six at various speeds

Model	Speed		C_d	C_l
	Km/h	m/s		
Model six	80	22.222	0.4493	-0.6194
	120	33.333	0.4518	-0.6290
	160	44.444	0.4544	-0.6387

5.8.2 Pressure contour

Figures 5.84–5.86 show the pressure contour on the symmetry plane and on the body of the model six at three different velocities (80, 120, and 160 km/h).

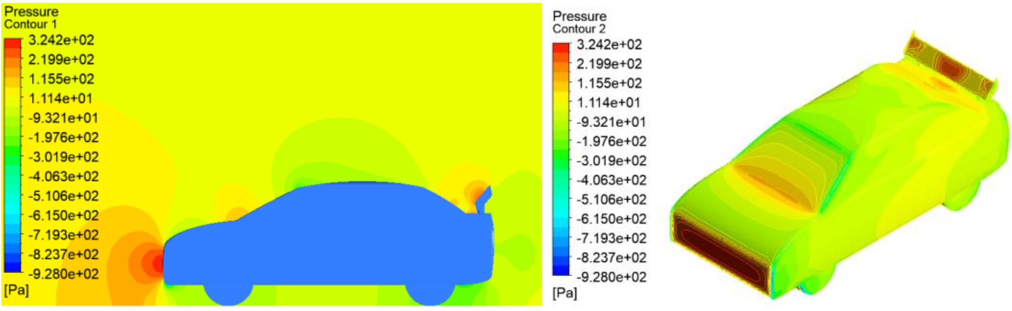

(a) (b)

Figure 5.84. Pressure contour (a) on symmetry plane (b) on body of model six at 80 km/h

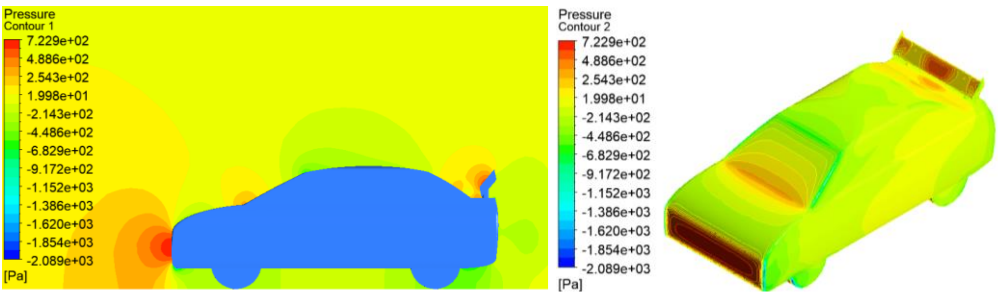

(a) (b)

Figure 5.85. Pressure contour (a) on symmetry plane (b) on body of model six at 120 km/h

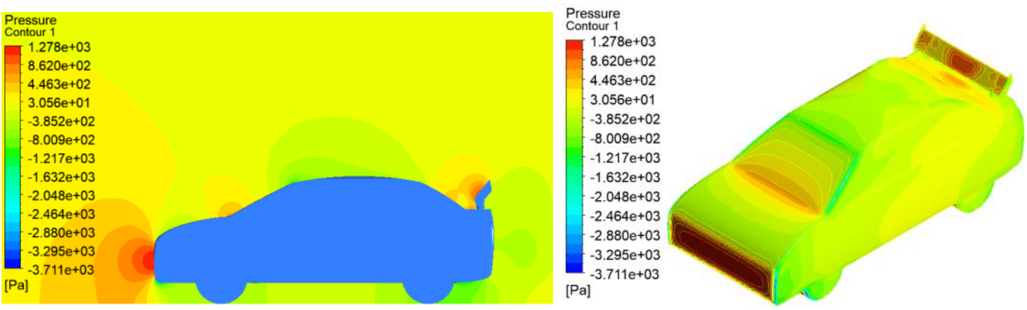

(a) (b)

Figure 5.86. Pressure contour (a) on symmetry plane (b) on body of model six at 160 km/h

The level of pressure influence on the car's surface is shown in Figures 5.84–5.86, indicated by the contour of the static pressure distribution. The contour of the pressure distribution in Figures 5.84–5.86 is more similar to the above models. However, we can see that the pressure around the rear wing-type spoiler increased due to an increase in its angle of inclination. When the speed of a vehicle increases, the maximum pressure also increases on the vehicle body and around the rear wing-type spoiler.

5.8.3 Velocity contour and streamline

Figures 5.87–5.89 show the velocity contour and streamline flow of a model six at three different velocities (80, 120, and 160 km/h) on the symmetry plane.

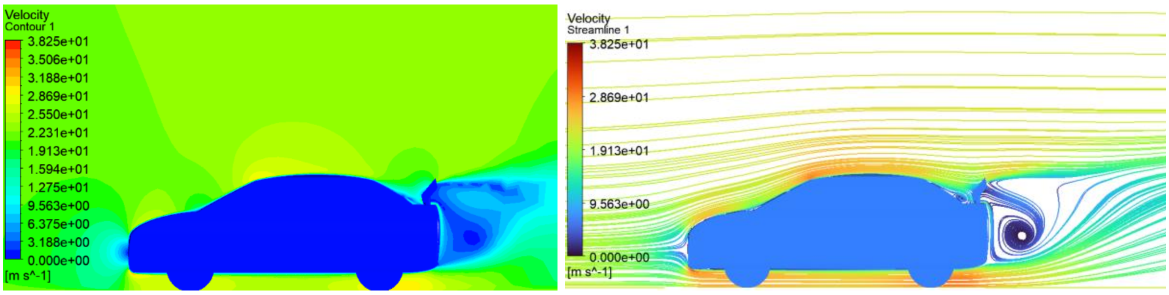

(a) (b)

Figure 5.87. (a) Velocity contour and (b) Streamline of model six at 80 km/h

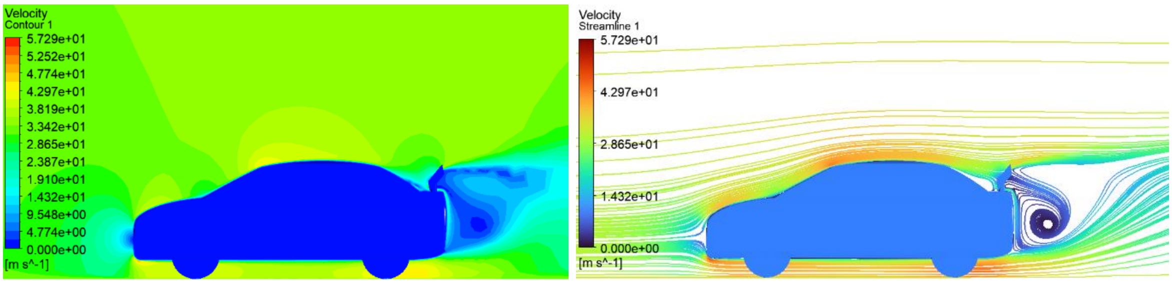

(a) (b)

Figure 5.88. (a) Velocity contour and (b) Streamline of model six at 120 km/h

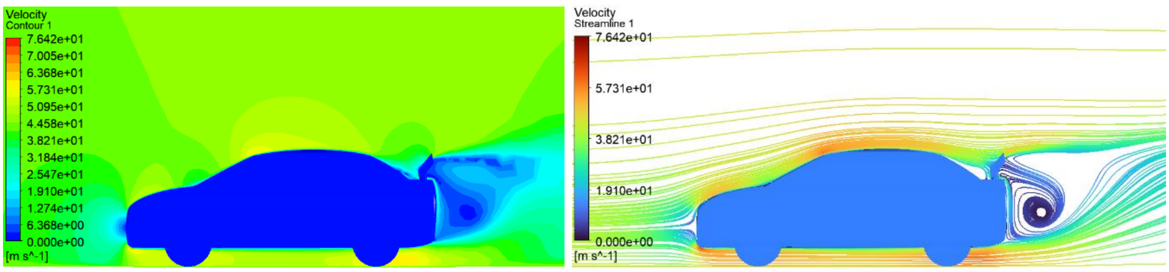

(a) (b)

Figure 5.89. (a) Velocity contour and (b) Streamline of model six at 160 km/h

The flow of air over the car body causes a velocity distribution, leading to aerodynamic loads on the body of the model six. The velocity distribution in Figure 5.87–5.89 shows the amount of velocity at various region of the model six.

5.9 Model seven (Baseline model with a 90-degree spoiler inclination)

5.9.1 Drag and Lift Coefficients

The convergence history of the drag and lift coefficients for model seven (baseline model with rear wing type spoiler at 90 degree angle of inclination) at three different speeds (80, 120, and 160 km/h) is shown in Figures 5.90–5.96.

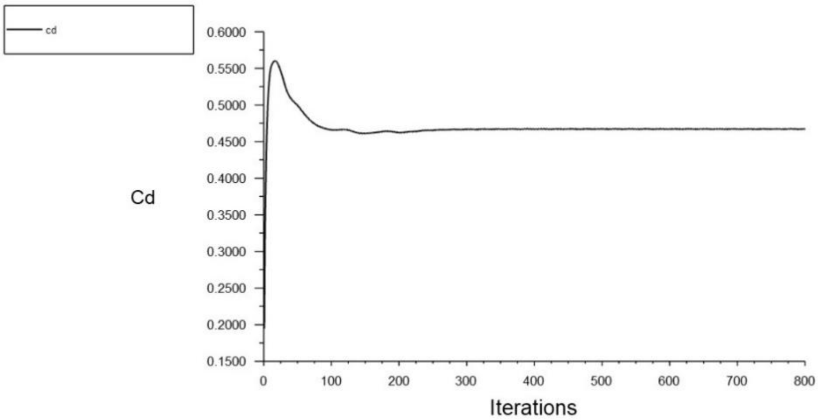

Figure 5.90. Drag coefficient convergence history of model seven at 80 km/h

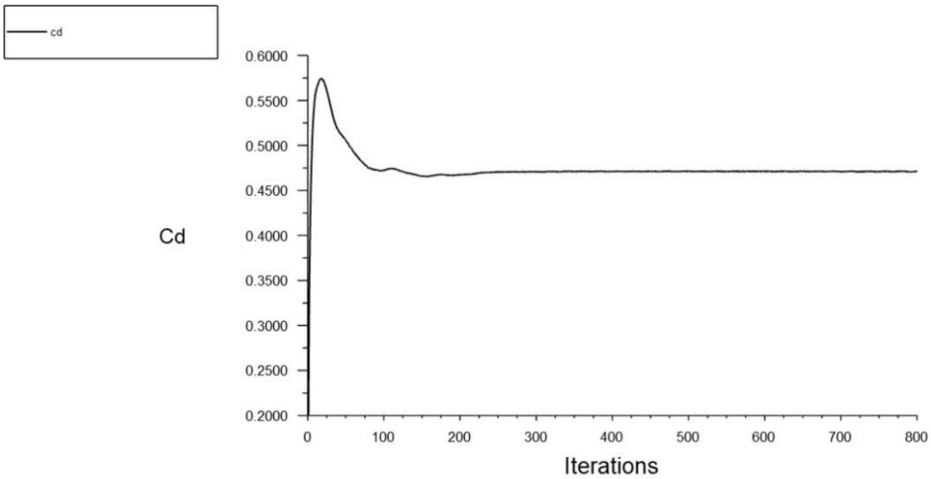

Figure 5.91. Drag coefficient convergence history of model seven at 120 km/h

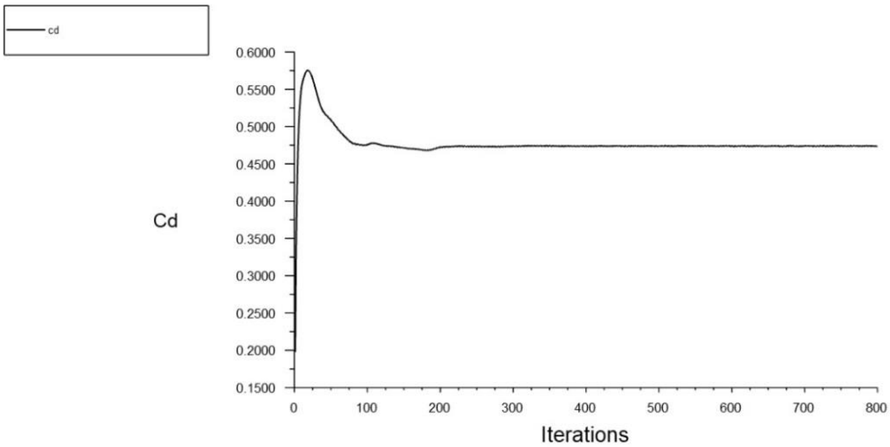

Figure 5.92. Drag coefficient convergence history of model seven at 160 km/h

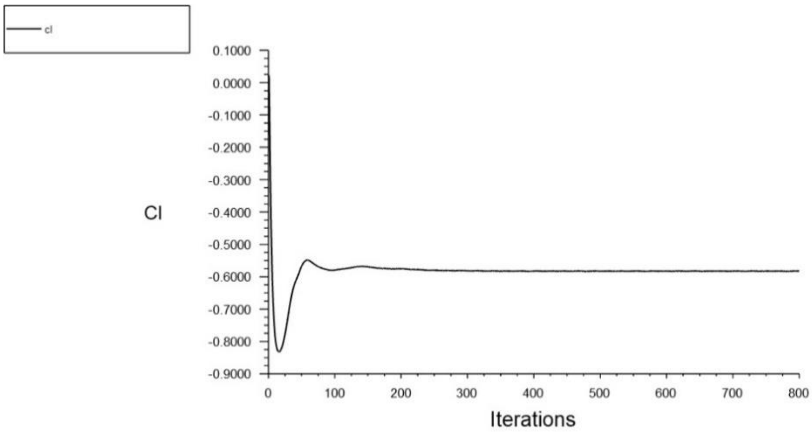

Figure 5. 93. Lift coefficient convergence history of model seven at 80 km/h

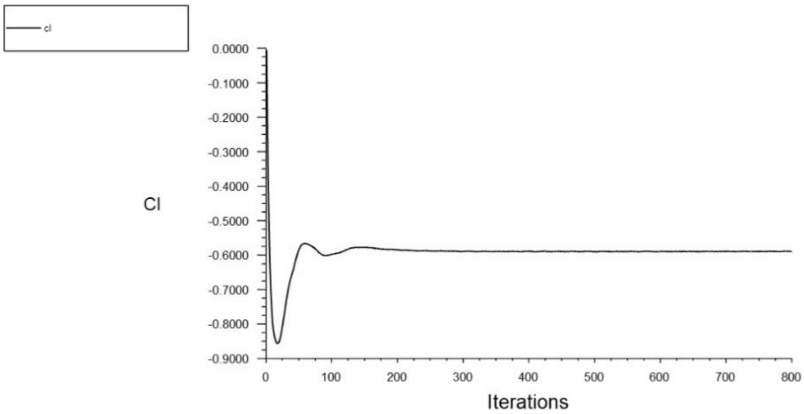

Figure 5. 94. Lift coefficient convergence history of model seven at 120 km/h

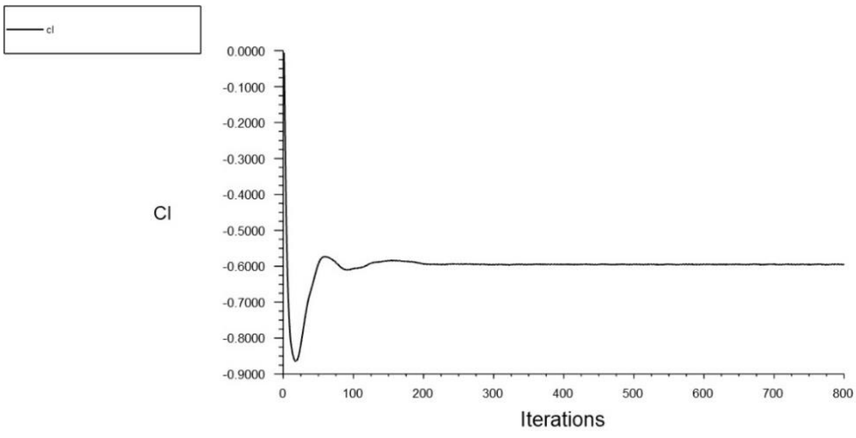

Figure 5.95. Lift coefficient convergence history of mode seven at 160 km/h

The drag and lift coefficient convergence histories in Figures 5.90–5.96 above show that both parameters converged well before the 800th iteration.

The drag and lift coefficients of a model seven examined at different speeds are summarized in Table 5.10. The drag coefficient of model seven increased with increasing speed, suggesting increased aerodynamic resistance. While the lift coefficient decreased, this led to increased vehicle stability at high speeds.

Table 5.10. Drag and lift coefficient of the model seven at various speeds

Model	Speed		C_d	C_l
	Km/h	m/s		
Model seven	80	22.222	0.4676	-0.5825
	120	33.333	0.4708	-0.5898
	160	44.444	0.4737	-0.5944

5.9.2 Pressure contour

Figures 5.96–5.98 show the pressure contour on the symmetry plane and on the body of the model seven at three different velocities (80, 120, and 160 km/h).

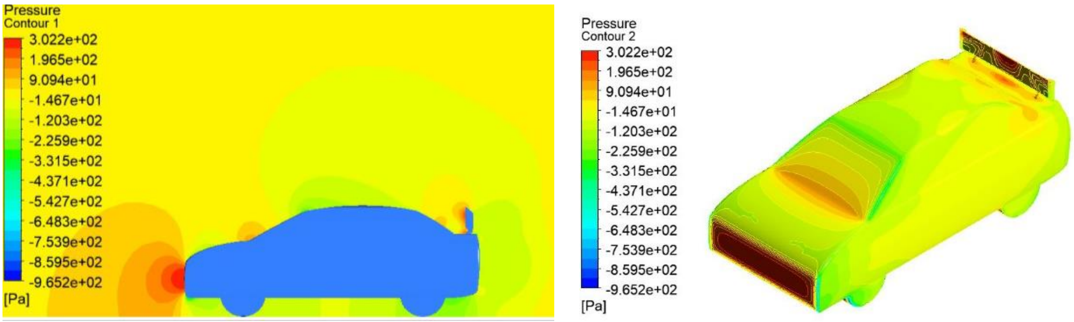

(a) (b)

Figure 5. 96. Pressure contour (a) on symmetry plane (b) on body at 80 km/h

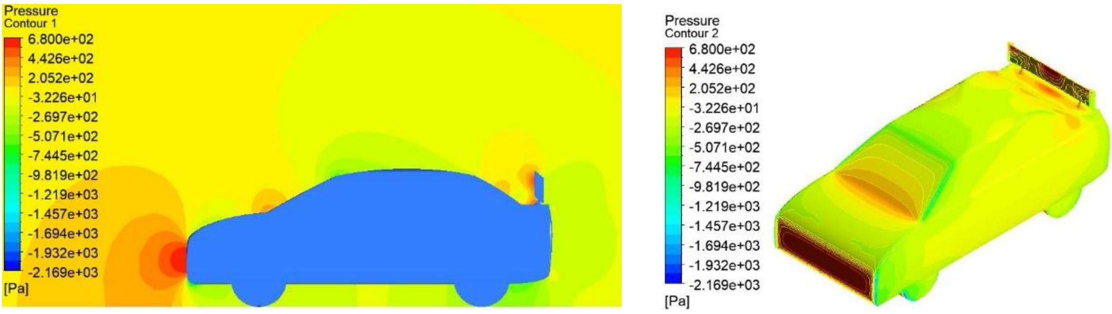

(a) (b)

Figure 5. 97. Pressure contour (a) on symmetry plane (b) on body at 120 km/h

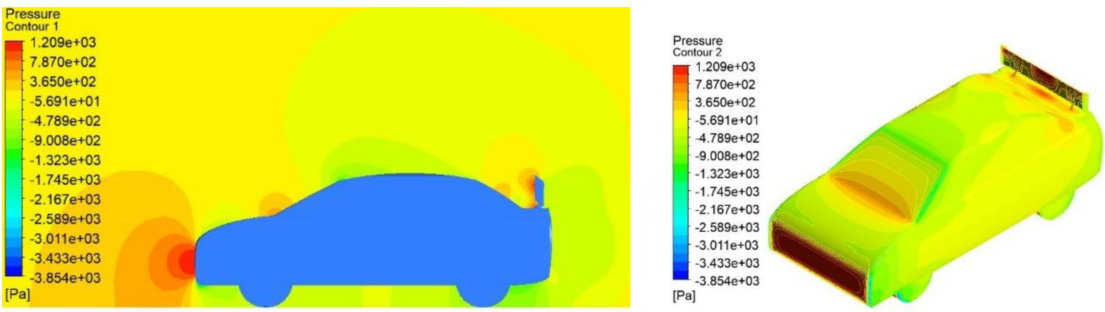

(a) (b)

Figure 5. 98. Pressure contour (a) on symmetry plane (b) on body at 160 km/h

The level of pressure influence on the car's surface is shown in Figures 5.96–5.98, indicated by the contour of the static pressure distribution. The contour of the pressure distribution in Figures 5.96–5.98 is more similar to the above models. However, we can see that the pressure around the rear wing-type spoiler increased due to an increase in its angle of inclination. When the speed of a vehicle increases, the maximum pressure also increases on the vehicle body and around the rear wing-type spoiler.

5.9.3 Velocity contour and streamline

Figures 5.99–5.101 show the velocity contour and streamline flow of a model seven at three different velocities (80, 120, and 160 km/h) on the symmetry plane.

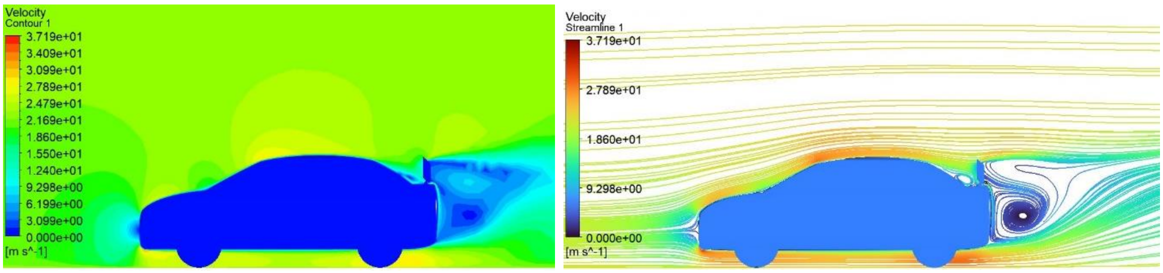

(a) (b)

Figure 5.99. (a) Velocity contour and (b) Streamline of model seven at 80 km/h

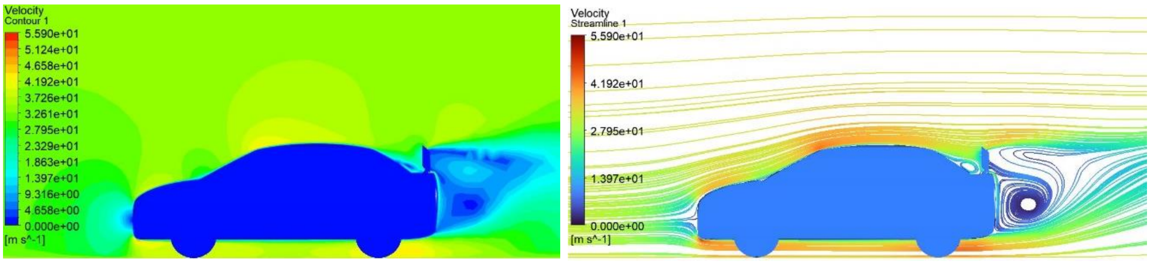

(a) (b)

Figure 5. 100. (a) Velocity contour and (b) Streamline of model seven at 120 km/h

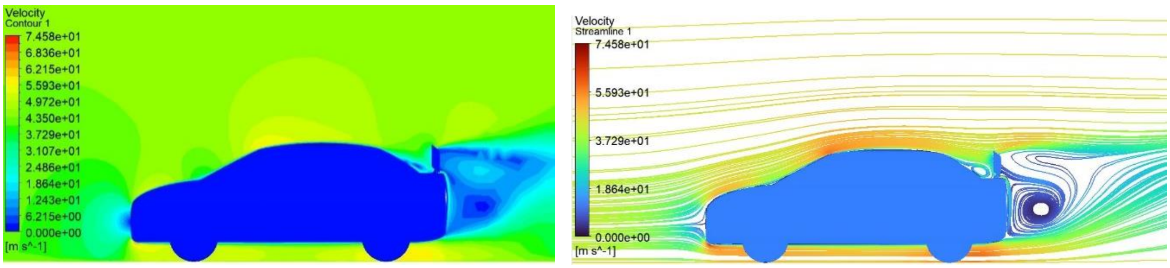

(a) (b)

Figure 5. 101. (a) Velocity contour and (b) Streamline of model seven at 160 km/h

The flow of air over the car body causes a velocity distribution, leading to aerodynamic loads on the body of the model seven. The velocity distribution in Figure 5.99–5.101 shows the amount of velocity at various region of the model seven.

5.10 Comparative Analysis of Models

The drag and lift coefficients for all models are shown in the following Figures 5.102–5.103 at three different speeds: 80 km/h, 120 km/h, and 160 km/h. allowing to compare the aerodynamic performance of each model by examining these values.

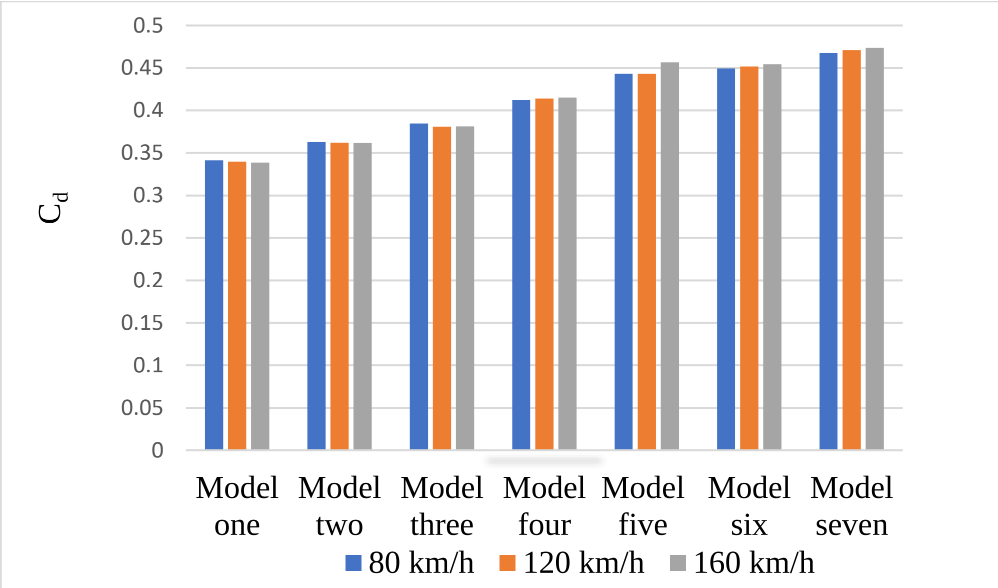

Figure 5.102. Comparison of the drag coefficient of models at various speed

As shown in Figure 5.102 and Table 5.11 the drag coefficient (C_d) for model one through three decreases as speed increases from 80 km/h to 160 km/h. However, models four, five, six and seven exhibit an increase in drag coefficient with increasing speed over the same range. At 160 km/h, the model one had the lowest drag coefficient among all the models analyzed. Model seven, on the other hand, had the highest coefficient of drag at the same speed.

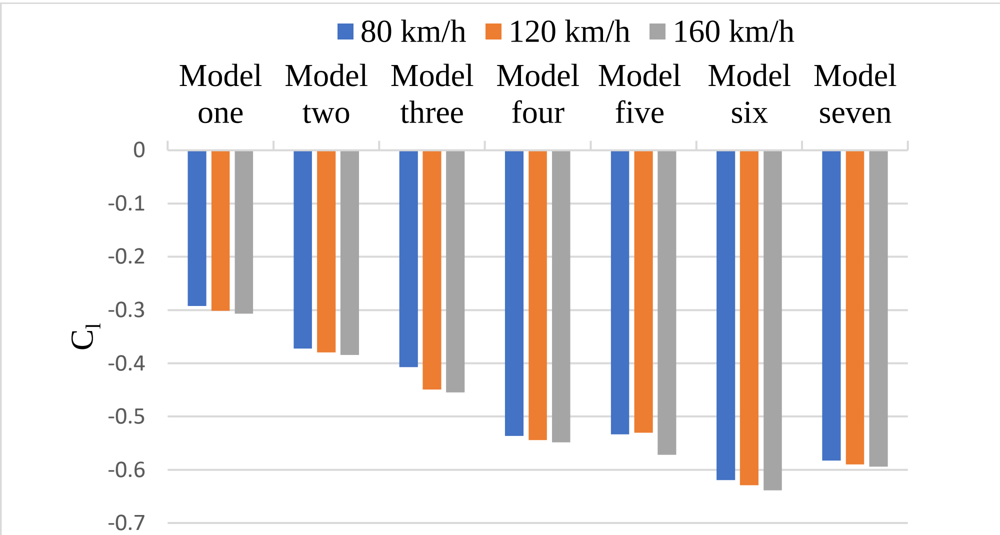

Figure 5.103. Comparison of the lift coefficient of models at various speed

Figure 5.103 and Table 5.11 show that the lift coefficient (C_l) for all models, decreases as speed increases from 80 km/h to 160 km/h. At 80 km/h, the model one exhibited the highest lift coefficient among all the models analyzed. Model six, on the other hand, exhibited the lowest coefficient of lift at a speed of 160 km/h.

From Table 5.11, when the angle of inclination of the rear wing-type spoiler increases, the average drag coefficient increases, but the lift coefficient decreases. However, in model seven, the lift is not higher compared to model six.

Table 5.11. Comparative Analysis of Models

Models	Speed (Km/h)	C_d	Average c_d value	C_d % change	C_l	Average c_l value	C_l % change
Model one	80	0.3414	0.3399	-	-0.2923	-0.3	-
	120	0.3397			-0.3013		
	160	0.3387			-0.3066		
Model two	80	0.3629	0.3623	+6.59	-0.3722	-0.3788	-26.27
	120	0.3622			-0.3797		
	160	0.3618			-0.3846		
Model three	80	0.3845	0.3822	+12.44	-0.4072	-0.4371	-45.7
	120	0.3808			-0.4495		
	160	0.3813			-0.4546		
Model four	80	0.4123	0.4139	+21.77	-0.5362	-0.5431	-81.03
	120	0.4140			-0.5442		
	160	0.4153			-0.5488		
Model five	80	0.4432	0.4484	+31.92	-0.5332	-0.5453	-81.77
	120	0.4454			-0.5304		
	160	0.4565			-0.5723		
Model six	80	0.4493	0.4518	+32.92	-0.6194	-0.6290	-109.67
	120	0.4518			-0.6290		
	160	0.4544			-0.6387		
Model seven	80	0.4676	0.4707	+38.48	-0.5825	-0.5889	-96.3
	120	0.4708			-0.5898		
	160	0.4737			-0.5944		

5.11 Aerodynamic braking distance calculation

The braking distance is the most useful parameter for evaluating the impact of improved aerodynamic braking on vehicle performance (Niu et al., 2021). According to (Kurec et al., 2019a; Ramar et al., 2020), only aerodynamic braking is considered, and the braking distance is calculated using the equation below.

$$m\frac{dv}{dt} = -\mu(mg - 0.5\rho v^2 AC_l) - 0.5\rho v^2 AC_d \quad (4.\ 1)$$

By integrating the above equation (4.1), the following equation for the braking distance (s), can be obtained:

$$s = \int_{v_i}^{v_f} \frac{mv \cdot dv}{-\mu(mg - 0.5\rho v^2 AC_l) - 0.5\rho v^2 AC_d} \quad (4.\ 2)$$

Where s, m, v, $\frac{dv}{dt}$ represents the braking distance, vehicle mass, vehicle speed and acceleration, respectively. v_f And v_i are the final target speed after braking and initial speed, respectively. While the vertical loads' transfer depends on the coefficient of friction μ, the vehicle's body is influenced by the force that it’s mass exerts, caused by the acceleration by gravity(mg), the aerodynamic lift ($0.5\rho v^2 AC_l$), and the aerodynamic drag ($0.5\rho v^2 AC_d$). The Gross mass of baseline model was equal to 1335 kg, while the standard model's reference area was 2.234 m^2 and the models with the rear end wing type spoiler was 2.254 m^2. As Eq. (4.1) includes the entire values of the aerodynamic loads, it can only be used to examine the scenario in which a vehicle brakes in a straight path and level road. The performance of the vehicle's braking mechanism, the driver's braking manner, and the characteristics of the tires are among the aspects that are ignored because of the simplicity of use of the calculation in Eq. (4.1).

A variety of velocities were examined for a passenger car in order to take into consideration the effect of aerodynamic forces on velocity, including 80 km/h (22.222 m/s), 120 km/h (33.333 m/s), and 160 km/h (44.444 m/s). The coefficient of friction on the road can be estimated to be 1, 0.5, and 0.1. 1 indicates ideal road conditions for driving, whereas a value of 0.5 indicates difficult or bad road conditions that demand caution. A value of 0.1 indicates an exceedingly risky surface, such as an ice patch, stressing the significant drop in traction available (Harned et al., 1969; Kurec et al., 2019; Ramar et al., 2020). Table 5.12 shows that the braking capabilities of the models with rear wing-type spoiler inclined at different angles are being evaluated for decelerating from an initial speed to zero and compared with model one.

Table 5.12. The braking capabilities of the model one and other models considering slowing down to zero from the initial speed

Models	Friction Coefficient	Initial Speed (km/h)	Braking Distance(m)	Difference from model one(%)
Model one	1	80	24.76	-
		120	54.60	-
		160	94.51	-
	0.5	80	49.1	-
		120	107.21	-
		160	183.23	-
	0.1	80	230.18	-
		120	470.49	-
		160	746.49	-
Model two	1	80	24.70	-0.24
		120	54.35	-0.46
		160	93.63	-0.93
	0.5	80	48.95	-0.31
		120	106.52	-0.64
		160	181.25	-1.08
	0.1	80	228.63	-0.67
		120	464.42	-1.29
		160	732.29	-1.90
Model three	1	80	24.65	-0.44
		120	54.08	-0.95
		160	92.96	-1.64
	0.5	80	48.83	-0.55
		120	105.97	-1.17
		160	179.71	-1.92
	0.1	80	227.33	-1.24
		120	459.42	-2.35
		160	720.75	-3.45
Model four	1	80	24.56	-0.81
		120	53.68	-1.68
		160	91.81	-2.86
	0.5	80	48.62	-0.98
		120	105.04	-2.02
		160	177.13	-3.33
	0.1	80	225.24	-2.15
		120	451.49	-4.04
		160	702.75	-5.86

Model five	1	80	24.54	-0.89
		120	53.57	-1.89
		160	91.51	-3.17
	0.5	80	48.54	-1.14
		120	104.65	-2.39
		160	176.07	-3.91
	0.1	80	223.56	-2.88
		120	445.25	-5.36
		160	688.80	-7.73
Model six	1	80	24.49	-1.09
		120	53.32	-2.34
		160	90.80	-3.93
	0.5	80	48.43	-1.36
		120	104.17	-2.84
		160	174.75	-4.63
	0.1	80	222.10	-3.51
		120	443.18	-5.8
		160	684.29	-8.33
Model seven	1	80	24.50	-1.05
		120	53.38	-2.23
		160	90.98	-3.74
	0.5	80	48.43	-1.36
		120	104.18	-2.83
		160	174.79	-4.61
	0.1	80	222.29	-3.43
		120	440.60	-6.35
		160	678.55	-9.10

From Table 5.12, we can observe that the braking performance improves as the inclination angle of the rear-end wing-type spoiler increases. The highest angle, which generates high drag and negative lift, significantly reduces the braking distance on ideal road and bad road conditions, such as model six. The Model seven reduced the maximum aerodynamic braking distance on icy roads by 9.1% compared to the model one. During deceleration from 160 km/h to zero.

5.12 Adjustable rear end wing type Spoiler Prototype Development

This section covers the circuit diagram, simulation of the prototype, and assembly of the final functional prototype of an adjustable rear-end wing type of spoiler.

5.12.1 Circuit design and simulation

The Proteus software and Cirkit Designer were used for circuit design and simulation. A set of tools for creating and simulating electronic circuits is provided by Proteus software. Before building physical prototypes, Proteus software was used to model and analyze the behavior of circuits to make sure they operated as intended. Finally, Cirkit Designer was used to show a clear representation of the actual components and their wiring diagram.

The Arduino UNO microcontroller serves as CPU in this prototype, interpreting sensor input and controlling its functions according to pre-programmed logic. A microcontroller serves key functions in this application, including:

- Reads the digital outputs from the speed sensor
- Provide the LCD with accurate data and information
- Give a command to the relay depending on the reading from the speed sensor

Figure 5.104 shows a Proteus simulation illustrating the application of the brake when the speed is below 80 km/h. In this simulation, the red LED represents a solenoid. If the speed is below 80 km/h, the Arduino microcontroller does not energize the relay. At this time, if the brake pedal is depressed and the brake switch is closed, the solenoid is not energized (the LED is off) because the circuit is not closed due to the relay being open.

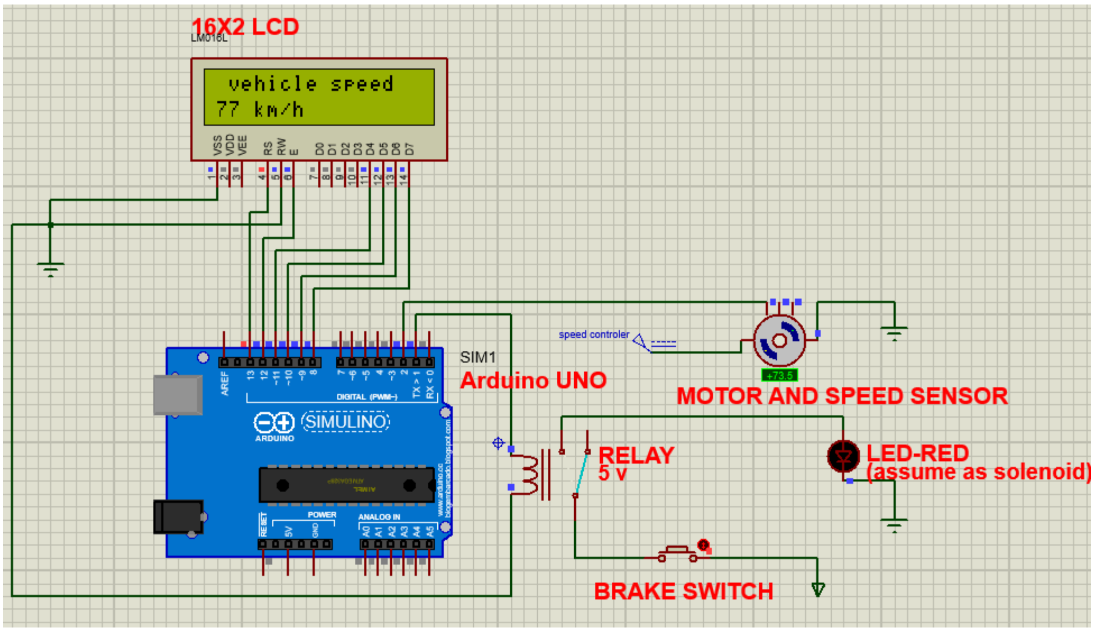

Figure 5.104. Proteus simulation when the brake is applied and the speed is below 80 km/h

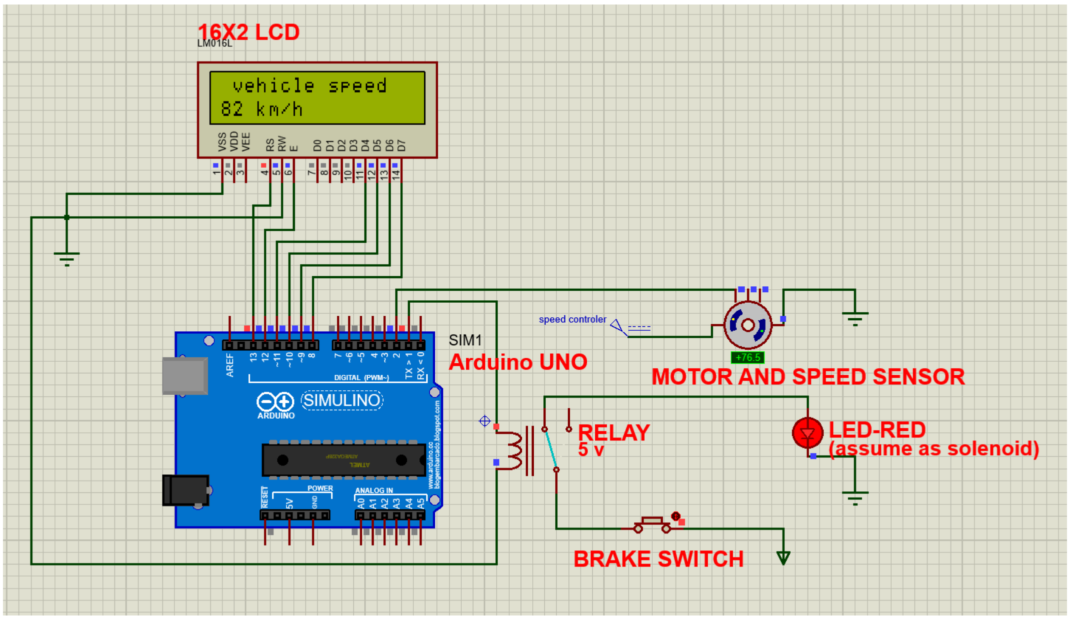

Figure 5.105. Proteus simulation when the brake is applied and the speed is above 80 km/h

Figure 5.105 shows a Proteus simulation illustrating the application of the brake when the speed exceeds 80 km/h. In this simulation, if the speed exceeds 80 km/h, the Arduino microcontroller will energize the relay. At this time, when the brake pedal is depressed and the brake switch is closed, the solenoid is energized (the LED is on) because the circuit is closed due to the relay being closed.

Figure 5.106 shows the clear image of the wiring diagram of the prototype with their each components.

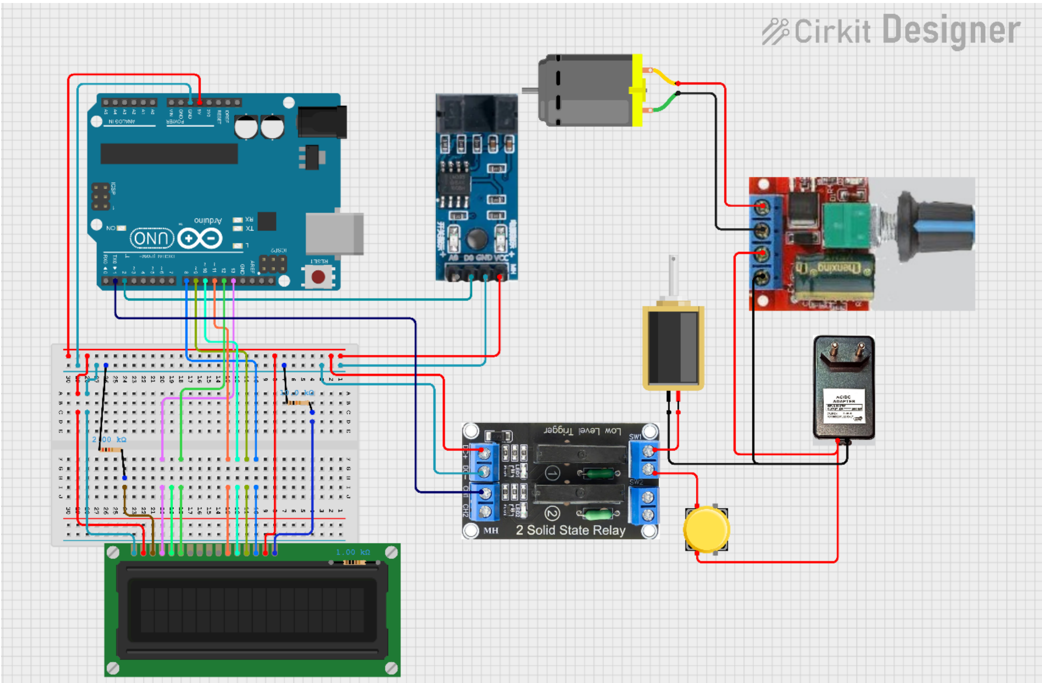

Figure 5.106. Wiring diagram of the prototype

5.12.2 Working principle and Assembly of Rear Wing Type Spoiler

On this prototype, the vehicle speed is determined by the DC electric motor speed, and the motor's speed can be regulated by using a mini-DC motor PWM speed controller. The LM393 is a dual comparator IC, which means it compares two analog values and returns a digital signal (HIGH or LOW) based on the result. The LM393 can be used here to compare the sensor's voltage to a predetermined reference voltage. When a cover rotor part passes by, the voltage rises, resulting in a high signal from the LM393. This high signal can then be used as an interrupt or trigger by the Arduino code to perform additional speed calculations. Once the Arduino has calculated the speed, it may display it on the LCD panel. And the algorithm then compares the measured speed with a predefined threshold, set at 80 km/h. If the speed exceeds 80 km/h as shown in Figure 5.109, the code triggers the solid state relay by setting the control pin to a high signal (5V). If the brake is applied at this moment, the solenoid connected to the wing spoiler is activated, causing it to tilt the spoiler to a maximum angle. Otherwise, it stays at a 0-degree angle as shown in Figure 5.108. The Arduino is powered by 5 volts, while the DC electric motor uses 12 volts from the adapter.

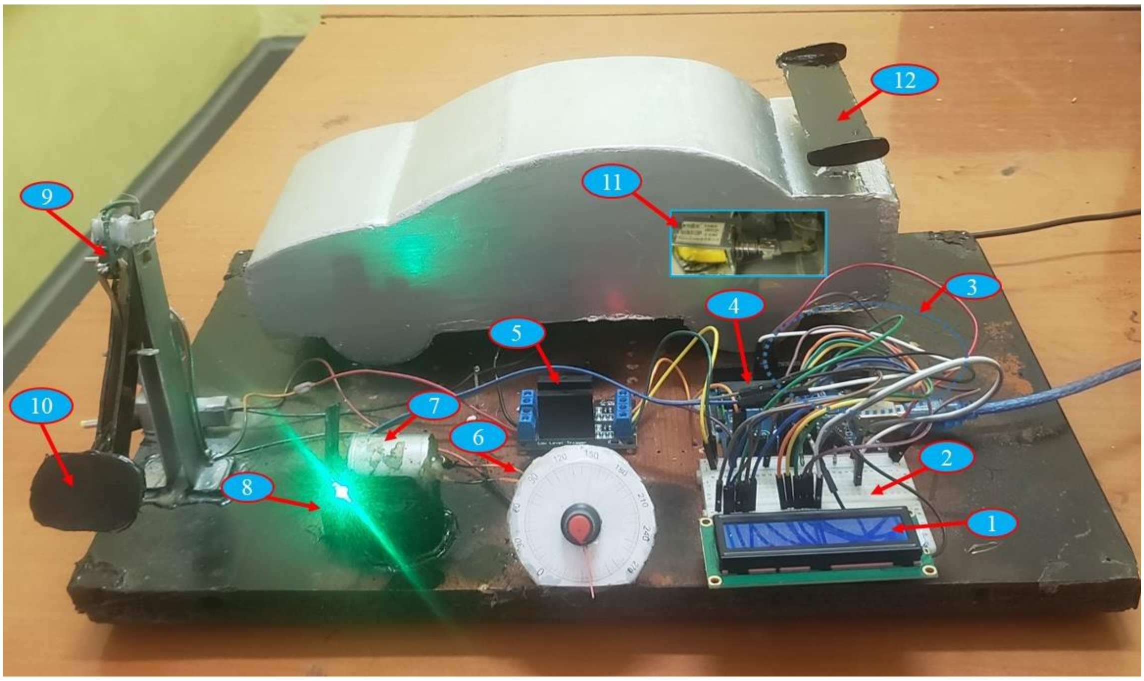

1. 16×2 LCD	4. Arduino Uno	7. DC motor	10. Brake pedal
2. Breadboard	5. Solid State Relay (SSR)	8. LM393 Infrared Speed Sensor	11. Solenoid
3. Jumper wires	6. DC motor PWM Speed Controller	9. Brake switch	12. Rear end wing type Spoiler

Figure 5.107. Components used in the system

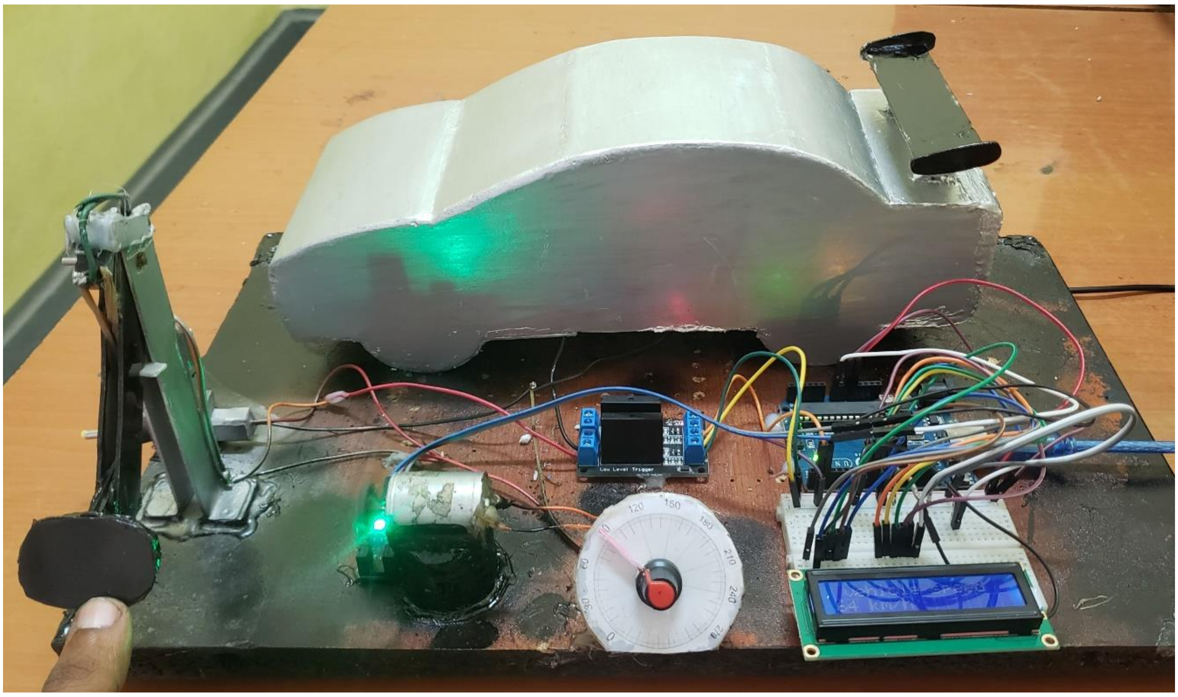

Figure 5.108. Brake applied at the speed below 80 km/h

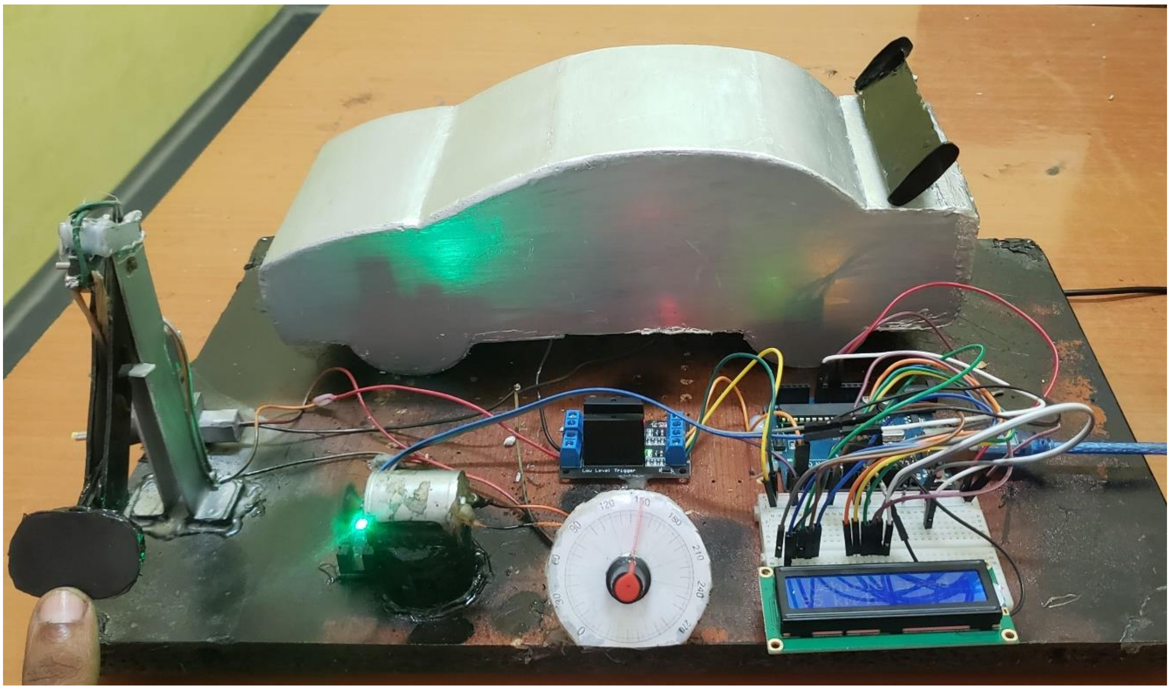

Figure 5.109. Brake applied at speed above 80 km/h

5.12.2.1 Relationship between the rotation angle of the knob, voltage, and speed

A Pulse Width Modulation (PWM) speed controller regulates a DC motor's speed by manipulating the voltage it receives. Instead of directly altering the voltage, it employs a rapid on-off switching technique. Visualize a switch that rapidly turns the full supply voltage on and off at a high frequency. The proportion of time the switch is on compared to when it's off is known as the duty cycle. This duty cycle is what the knob on the controller adjusts.

When the knob turn (often linked to a potentiometer), the resistance changes, thereby controlling the on-off timing of the switch. By modifying this duty cycle, the controller effectively changes the average voltage that the motor receives. A higher duty cycle (more "on" time) leads to a higher average voltage, causing the motor to spin faster. Conversely, a lower duty cycle (less "on" time) results in a lower average voltage, slowing down the motor. Essentially, the knob controls the on-off pattern of the voltage, which ultimately determines the average voltage supplied to the motor and consequently its speed.

Table 5.13. Relationship between the rotation angle of the knob, voltage, and speed

Angle of the knob (degree)	Voltage (volt)	Speed (km/h)
0	0	0
30	1.36	18
60	2.9	43
90	4.4	65
120	6.09	101
150	7.6	117
180	9.09	135
210	10.41	154
240	12.08	184

5.13 Summary

The baseline model car and the wing-type spoiler were designed using SOLIDWORKS 2023 software. The models were assigned as follows: model one (baseline model with spoiler inclined at a 0-degree angle), model two (baseline model with spoiler inclined at an 10-degree angle), model three (baseline model with spoiler inclined at a 20-degree angle), model four (baseline model with spoiler inclined at a 30-degree angle), model five (baseline model with spoiler inclined at a 40-degree angle), model six (baseline model with spoiler inclined at a 50-degree angle) and model seven (baseline model with spoiler inclined at a 90-degree angle). And then all models, including the baseline model, were analyzed using ANSYS Fluent 2022 software at different speeds (80, 120, and 160 km/h). The CFD software allows for the simulation of the flow of air around the car and spoiler. This analysis was used to determine the aerodynamic forces acting on the car, such as drag and lift. The braking distance was also calculated, and the model that provides a greater reduction is model seven, which can reduce braking distance by 9.1% compared to model one when the vehicle is driven on icy roads. The prototype was also developed to demonstrate the working principle.

It had both software and hardware components. The Arduino IDE software was used to program the Arduino UNO microcontroller. The Proteus software and Cirkit Designer were used for circuit design and simulation. the hardware components (including an Arduino UNO board, solid state relay, solenoid, breadboard, brake switch, infrared speed sensor, LCD, DC motor, Jumper wire and Mini DC motor PWM Speed Controller) that were assembled to create the prototype.

CHAPTER SIX
CONCLUSIONS AND RECOMMENDATIONS

6.1 Conclusions

The baseline model of the Suzuki Dzire was analyzed using ANSYS Fluent, both without and with a rear-end wing-type spoiler, at different speeds and angles after all the 3D models were designed using SOLIDWORKS 2023 software. The results indicated that as the angle increased, both the drag and negative lift also increased. Model seven exhibited the highest drag, but it generated less negative lift compared to model six.

The highest drag is 0.4737 obtained from model seven at a speed of 160 km/h, while the lowest is 0.3387 from model one at the same speed when compared with all models, excluding the baseline model. The lowest lift coefficient is -0.6387, obtained from model six at a speed of 160 km/h, and the highest is -0.2923 from model one at a speed of 80 km/h excluding the baseline model.

The addition of the rear-end wing-type spoiler slightly increased drag at low inclination angles but significantly improved the negative lift force, making it much more effective for stability during acceleration. On model one, the minimum drag coefficient and a higher lift coefficient were obtained. This indicates that while drag may increase slightly by 3.95% and the lift decreases significantly by 108.9%, it enhances stability and handling during acceleration. Therefore, at a 0-degree angle of attack, an increase in downforce can be achieved.

At a higher angle of inclination model seven, the drag force increase. However, this results in reduced acceleration because increased drag causes a decrease in the vehicle's acceleration. This is crucial during deceleration.

The aerodynamic braking distance was calculated for models one, two, three, four, five, six and seven at different speeds and finally compared with Model One. The highest angle, which generates high drag, significantly reduces the braking distance on icy road condition. The aerodynamic braking effect increases when the friction coefficient decreases. For normal road conditions, the friction coefficient is taken as 1.0. For bad road conditions (rain and moisture on the road), it is 0.5, and for icy roads, it is 0.1. The Model Seven reduced the maximum aerodynamic braking distance on icy roads by 9.1% compared to Model One when slowing down from 160 km/h to zero.

6.2 Recommendations

- ✓ A computer with high processing speed and capacity is recommended for more precise outcomes. It will also help to reduce processing time and improve mesh quality.
- ✓ It is recommended that the university acquire a 3D printing facility. The acquisition of such a facility would significantly enhance the university's research capabilities. 3D printing enables researchers to create models for wind tunnel testing.
- ✓ It is recommended to the automotive companies to implement adjustable spoiler on cars, which improves braking efficiency and increase stability at high speed.

Recommendation for future work

- ✓ Conduct wind tunnel test on the baseline model makes sure the accuracy of the numerical results.
- ✓ To achieve good performance in all driving conditions, the spoiler should be adjusted to the optimum angle based on speed and every situation. Making the design of the adjustable spoiler, which changes its angle with speed, more ideal for fuel consumption, stability, and braking effectiveness
- ✓ By using optimization tools and investigating with alternative chord lengths, spoiler types (different NACA airfoils), and spoiler heights, it may be possible to further enhance the drag and lift coefficients. For different speeds and conditions.

REFERENCES

Abdellah, E., & Wang, B. (2017). CFD analysis on effect of front windshield angle on aerodynamic drag. *IOP Conference Series: Materials Science and Engineering*, *231*(1). https://doi.org/10.1088/1757-899X/231/1/012173

Al-Saadi, A. (2019). *Analysis of Novel Techniques of Drag Reduction and Stability Increase for Sport Utility Vehicles using Computational Fluid Dynamics*. https://doi.org/10.13140/RG.2.2.15580.74880

Baker, N., Kelly, G., & O'Sullivan, P. (2019). A grid convergence index study of mesh style effect on the accuracy of the numerical results for an indoor airflow profile. In *International Journal of Ventilation* (Vol. 19). https://doi.org/10.1080/14733315.2019.1667558

Baldwin, B., & Lomax, H. (1978). Thin-layer approximation and algebraic model for separated turbulentflows. *16th Aerospace Sciences Meeting*, 257.

Bates, M. (2011). Hardware Prototyping. In *PIC Microcontrollers* (pp. 201–231). Elsevier. https://doi.org/10.1016/b978-0-08-096911-4.10010-2

Bourgoin, A., El Kadi Abderrezzak, K., Benhamadouche, S., & Ata, R. (2021). An adoption of the Spalart–Allmaras turbulence model for two-and three-dimensional free surface environmental flows. *Journal of Hydraulic Research*, *59*(2), 314–328.

Cakir, M. (2012). *Scholar Commons CFD study on aerodynamic effects of a rear wing/ spoiler on a passenger vehicle*. http://scholarcommons.scu.edu/mech_mstr

Chen, H., Zhou, X., Feng, Z., & Cao, S.-J. (2022). Application of polyhedral meshing strategy in indoor environment simulation: Model accuracy and computing time. *Indoor and Built Environment*, *31*(3), 719–731.

Che Zakem, R. (2008). Aerodynamics of aftermarket rear spoiler. *Bachelor Thesis*.

Chidhambaram, K., Kumar, S. A., Kumar, T. M., & Dhanasekar, D. (2019). Design Analysis of Land Surveying Robot Using Arduino Uno. *No. May*, 6208–6214.

Costa, L. M. F., Montiel, J. E. S., Corrêa, L., Lofrano, F. C., Nakao, O. S., & Kurokawa, F. A. (2022). Influence of standard k-ε, SST κ-ω and LES turbulence models on the numerical assessment of a suspension bridge deck aerodynamic behavior. *Journal of the Brazilian Society of Mechanical Sciences and Engineering*, *44*(8), 350.

Das, R. C., & Riyad, M. (2017). CFD analysis of passenger vehicleat various angle of rear end spoiler. *Procedia Engineering*, *194*, 160–165.

Elwakeel, A. E., Mazrou, Y. S. A., Eissa, A. S., Okasha, A. M., Elmetwalli, A. H., Makhlouf, A. H., Metwally, K. A., Mahmoud, W. A., & Elsayed, S. (2023). Design and Validation of a Variable-Rate Control Metering Mechanism and Smart Monitoring System for a High-Precision Sugarcane Transplanter. *Agriculture*, *13*(12), 2218.

Gao, W., Kong, X., Deng, Z., Yu, W., Wu, Y., & Luo, J. (2021). Review of state of the art in active aerodynamic control research for vehicles. *Journal of Physics: Conference Series*, *1985*(1). https://doi.org/10.1088/1742-6596/1985/1/012040

Gemba, K. L. (2007). *Shape effects on drag*. https://www.researchgate.net/publication/330684511

Gorman, J., Bhattacharyya, S., Cheng, L., & Abraham, J. (2021). *Turbulence Models Commonly Used in CFD*. https://doi.org/10.5772/intechopen.99784

Haidar, A. M. A., Razali, R., Abdalla, A., Aziz, H. A., Noman, K. M. G., & Al-Jawfi, R. A. (2011). Protection of solar electric car DC motor with PIC controller. *Electrical Engineering and Control: Selected Papers from the 2011 International Conference on Electric and Electronics (EEIC 2011) in Nanchang, China on June 20-22, 2011, Volume 2*, 149–161.

Harned, J. L., Johnston, L. E., & Scharpf, G. (1969). *Measurement of Tire Brake Force Characteristics as Related to Wheel Slip (Antilock) Control System Design*. https://api.semanticscholar.org/CorpusID:109296144

Hasan Ali, M., Mashud, M., Al Bari, A., & Misbah-Ul Islam, M. (2013). *Aerodynamic Drag Reduction of a Car by Vortex Generation*. http://www.ijmejournal.com/https://sites.google.com/site/journalijme/

Hasibuan, A., Qodri, A., & Isa, M. (2021). Temperature monitoring system using arduino uno and smartphone application. *Bulletin of Computer Science and Electrical Engineering*, *2*(2), 46–55.

Hasibuan, A., Rosdiana, R., & Tambunan, D. S. (2021). Design and Development of An Automatic Door Gate Based on Internet of Things Using Arduino Uno. *Bulletin of Computer Science and Electrical Engineering*, *2*(1), 17–27.

Hucho, W.-Heinrich., & Ahmed, S. R. (1987). *Aerodynamics of road vehicles : from fluid mechanics to vehicle engineering*. Butterworths.

Ipilakyaa, T. D., Tuleun, L. T., & Kekung, M. O. (2018). Computational fluid dynamics modelling of an aerodynamic rear spoiler on cars. *Nigerian Journal of Technology*, *37*(4), 975. https://doi.org/10.4314/njt.v37i4.17

Islam, M. M., & Inam, M. I. (2022). *Numerical Investigation of the effect of different Aerofoil profile of a spoiler in a car*.

Ismail, M. P., Ishak, I. A., Samiran, N. A., Mohammad, A. F., Salleh, Z. M., & Darlis, N. (2022). CFD analysis on the effect of vortex generator on sedan car using ansys software. *International Journal of Integrated Engineering*, *14*(1), 73–83.

Jadhav, S. P., Dongare, G., Garud, A., Adsule, S., & Bobhate, C. (2021). DESIGN AND ANALYSIS OF EFFICIENT SHAPE OF AERODYNAMIC SHAPE OF CAR BODY. In *International Research Journal of Modernization in Engineering Technology and Science*. www.irjmets.com

Janković, A. S., & Dukic, R. V. (2011). Experimental determination of force and displacement of a car suspension. *Central European Journal of Engineering*, *1*(3), 279–286. https://doi.org/10.2478/s13531-011-0032-7

Jaszczur, M., & Młynarczykowska, A. (2020). A General Review of the Current Development of Mechanically Agitated Vessels. *Processes*, *8*, 982. https://doi.org/10.3390/pr8080982

Jesshope, D. J. (2012). *Development of an electronically controlled thruster*.

Jiang, L., Diao, M., Sun, H., & Ren, Y. (2018). Numerical Modeling of Flow Over a Rectangular Broad-Crested Weir with a Sloped Upstream Face. *Water*, *10*, 1663. https://doi.org/10.3390/w10111663

Jones, W. P., & Launder, B. E. (1972). The prediction of laminarization with a two-equation model of turbulence. *International Journal of Heat and Mass Transfer*, *15*(2), 301–314.

Kamal, M. N. F., Ishak, I. A., Darlis, N., Maji, D. S. B., Sukiman, S. L., Abd Rashid, R., & Azizul, M. A. (2021). A review of aerodynamics influence on various car model geometry through CFD techniques. *Journal of Advanced Research in Fluid Mechanics and Thermal Sciences*, *88*(1), 109–125.

Kang, S. O., Jun, S. O., Park, H. I., Song, K. S., Kee, J. D., Kim, K. H., & Lee, D. H. (2012). ACTIVELY TRANSLATING A REAR DIFFUSER DEVICE FOR THE AERODYNAMIC DRAG REDUCTION OF A PASSENGER CAR. *International Journal of Automotive Technology*, *13*(4), 583–592. https://doi.org/10.1007/s12239−012−0056−x

Kurec, K., Remer, M., & Piechna, J. (2019). The influence of different aerodynamic setups on enhancing a sports car's braking. *International Journal of Mechanical Sciences*, *164*, 105140. https://doi.org/https://doi.org/10.1016/j.ijmecsci.2019.105140

Leary, J. (2010). Computational Fluid Dynamics Analysis of a Low Cost Wind Turbine. *Mini-Project Report. University of Sheffield*.

Lee, M., Park, G., Park, C., & Kim, C. (2020). Improvement of grid independence test for computational fluid dynamics model of building based on grid resolution. *Advances in Civil Engineering*, *2020*, 1–11.

Louis, L. (2016). Working Principle of Arduino and Using it as a Tool for Study and Research. *International Journal of Control, Automation, Communication and Systems, 1*(2), 21–29. https://doi.org/10.5121/ijcacs.2016.1203

Maji, D. S. B., & Mustaffa, N. (2022). CFD Analysis of Rear-Spoilers Effectiveness on Sedan Vehicle in Compliance with Malaysia National Speed Limit. *Journal of Automotive Powertrain and Transportation Technology*, *2*(1), 26–36.

Malik, L., & Parshad, H. (2023). AERODYNAMIC ANALYSIS OF A CAR FOR REDUCING DRAG FORCE. *International Research Journal of Modernization in Engineering Technology and Science*.

Mariaprakasam, R. D. R., Mat, S., Samin, P. M., Othman, N., Wahid, M. A., & Said, M. (2023). Review on Flow Controls for Vehicles Aerodynamic Drag Reduction. *Journal of Advanced Research in Fluid Mechanics and Thermal Sciences*, *101*(1), 11–36. https://doi.org/10.37934/arfmts.101.1.1136

Mohankumar, M., & Raj, H. (2015). Investigating the Effect of Rear Spoiler and Rear Diffuser on Aerodynamic Forces using CFD. *International Journal of Engineering Research & Technology*, *3*(26), 1–6.

Muiruri, P. I., Motsamai, O. S., & Ndeda, R. (2019). A comparative study of RANS-based turbulence models for an upscale wind turbine blade. *SN Applied Sciences*, *1*(3), 237.

Muralidharan, V., Balakrishnan, A., Vardhan, V. K., Meena, N., & Kumar, Y. S. (2018). Design of Mechanically Actuated Aerodynamic Braking System on a Formula Student Race Car. *Journal of The Institution of Engineers (India): Series C*, *99*(2), 247–253. https://doi.org/10.1007/s40032-017-0354-1

Nagappan, D., Ravicahnder, K., Zikry, Z., Fikri, A., Amri, A., Subramaniam, S., Didane, D., Elshayeb, S., & Manshoor, B. (2023). *CFD Analysis of Heat Exchanger Over a Staggered Tube Bank for Different Angle Arrangement of Tube Banks*. *5*, 18–22.

Nath, D. S., Pujari, P. C., Jain, A., & Rastogi, V. (2021). Drag reduction by application of aerodynamic devices in a race car. *Advances in Aerodynamics*, *3*, 1–20.

Nawam, M. Z., Afzanizam, M., Rosli, M., Azwar, N., & Rosli, S. (2018). Simulation Study on the Effect of Rear-Wing Spoiler on the Open Aerodynamic Performance of Sedan Vehicle. *Journal of Advanced Research in Fluid Mechanics and Thermal Sciences Journal Homepage*, *49*, 146–154. www.akademiabaru.com/arfmts.html

Nayyar, A., & Puri, V. (2017). Smart farming: Iot based smart sensors agriculture stick for live temperature and moisture monitoring using arduino, cloud computing & solar technology. *Communication and Computing Systems - Proceedings of the International Conference on Communication and Computing Systems, ICCCS 2016*, 673–680. https://doi.org/10.1201/9781315364094-121

Niu, J., Wang, Y., Chen, Z., & Liu, F. (2021). Numerical study on the effect of braking plates on flow structure and vehicle and enhanced braking of vehicles inside and outside tunnels. *Journal of Wind Engineering and Industrial Aerodynamics*, *214*, 104670.

Norwazan, A. R., Khalid, A. J., Zulkiffli, A. K., Nadia, O., & Fuad, M. N. (2012). Experimental and numerical analysis of lift and drag force of sedan car spoiler. *Applied Mechanics and Materials*, *165*, 43–47. https://doi.org/10.4028/www.scientific.net/AMM.165.43

Parab, R., & Prajapati, S. (2019). IoT based relay operation. *International Journal of Engineering and Advanced Technology*, *9*(1), 6515–6520.

Paul, R. D., Al-Faruk, A., & Karua, P. (2020). *A Numerical Study on the Drag Reduction of Sedan Car using Vortex Generator*.

Poul Greibe. (2007). *Braking distance, friction and behaviour Findings, analyses and recommendations based on braking trials*. www.trafitec.dk

Ramar, K., Paramasivam, K., Subramani, Y., Jayaraman, J., Kumar, A., & Saicharan, T. R. (2020). Influence of various aerodynamic setups for enhancing car braking. *AIP Conference Proceedings*, *2311*. https://doi.org/10.1063/5.0034419

Sakib, M. H. R., & Mahmud, M. S. (2022). *CFD ANALYSIS OF CAR USING NACA 4412 SPOILER*.

Saleh, Z. M., & Ali, A. H. (2020). Numerical Investigation of Drag Reduction Techniques in a Car Model. *IOP Conference Series: Materials Science and Engineering*, *671*(1). https://doi.org/10.1088/1757-899X/671/1/012160

Samarasinghe, S. (2016). *Pool Playing Robot*. https://doi.org/10.13140/RG.2.2.30300.39044

Saxena, S., Mahesha, G. T., & Srinivas, G. (2020). Recent aerodynamic performance evaluation of commercial and non-commercial vehicles. *Journal of Physics: Conference Series*, *1706*(1). https://doi.org/10.1088/1742-6596/1706/1/012220

Sayma, A. (2009). *Computational fluid dynamics*. Bookboon.

Selvaraju, P. N., Parammasivam, K. M., & Shankar, D. G. D. (2015). Analysis of Drag and Lift performance in sedan car model using CFD. *Journal of Chemical and Pharmaceutical Sciences Www. Jchps. Com ISSN*, *974*, 2115.

Shukla, V., & Saxena, G. (2015). Computational Drag Analysis of Passenger Car Using Splines and Spoiler. *International Journal of Engineering Trends and Technology*, *21*(1), 1–11. https://doi.org/10.14445/22315381/IJETT-V21P201

Socrates, S., Naveen, M., #2, P., Suryanand, S., Kishore, J., & Suman Kumar, P. (2018). *COMPUTATIONAL INVESTIGATIONS OF AERODYNAMIC DRAG USING SPOILER OF AN AUTOMOBILE*. http://www.ijpam.eu

Somashekar, V. (2021). Comparative study on the prediction of aerodynamic characteristics of mini-unmanned aerial vehicle with turbulence models. *International Journal of Aviation, Aeronautics, and Aerospace*, *8*(1), 7.

Spalart, P., & Allmaras, S. (1992). A one-equation turbulence model for aerodynamic flows. *30th Aerospace Sciences Meeting and Exhibit*, 439.

Sripathi, A. V. (2017). *The impact of active aerodynamics on motorcycles using computational fluid dynamics simulations*. Minnesota State University, Mankato.

Stroustrup, B. (2013). *The C++ programming language*. Pearson Education.

Sudin, M. N., Abdullah, M. A., Shamsuddin, S. A., Ramli, F. R., & Tahir, M. M. (2014). Review of research on vehicles aerodynamic drag reduction methods. *International Journal of Mechanical and Mechatronics Engineering*, *14*(02), 37–47.

Tang, T., Anupam, K., Kasbergen, C., & Scarpas, A. (2017). Study of Influence of Operating Parameters on Braking Distance. *Transportation Research Record*, *2641*(1), 139–148. https://doi.org/10.3141/2641-16

Vinith, K. S. K., & Sathiamurthi, P. (2020). *Design And Fabrication Of Adaptive Spoiler For Go-Kart Vehicles*. www.ijstr.org

Weaver, D. S., & Mišković, S. (2021). A study of RANS turbulence models in fully turbulent jets: a perspective for CFD-DEM simulations. *Fluids*, *6*(8), 271.

Wilcox, D. (2006). *Turbulence Modeling for CFD (Third Edition) (Hardcover)*.

Yakkundi, V. (2018). *Effect of Spoilers on Aerodynamic Properties of Car*. http://dynamicpublisher.org/

Yusuf, S. N. A., Asako, Y., Sidik, N. A. C., Mohamed, S. B., & Japar, W. M. A. A. (2020). A short review on rans turbulence models. *CFD Letters*, *12*(11), 83–96.

Zafaruddin, M. A. D., Depikalasben, N. D. I., Azahar, M. B., Halim, A. W. A., Harun, N. F., Didane, D. H., Manshoor, B., & Abdelaal, M. A. S. (2023). A 3D CFD Simulation Study on The Impact of Backlight Angles on Drag Coefficients of Passenger Vehicles. *Journal of Design for Sustainable and Environment*, *5*(2), 38–45.

Zhang, H., Tang, S., Yue, H., Wu, K., Zhu, Y., Liu, C., Liang, B., & Li, C. (2020). Comparison of computational fluid dynamic simulation of a stirred tank with polyhedral and tetrahedral meshes. *Iranian Journal of Chemistry and Chemical Engineering (IJCCE)*, *39*(4), 311–319.

Zhang, X., & Zhang, H. (2011). The accelerated life experiment study of Solid State Relay. *2011 International Conference on Quality, Reliability, Risk, Maintenance, and Safety Engineering*, 349–351.

Zhao, Y., Akolekar, H. D., Weatheritt, J., Michelassi, V., & Sandberg, R. D. (2020). RANS turbulence model development using CFD-driven machine learning. *Journal of Computational Physics*, *411*, 109413.

Zharfan, M., Nazri, D. A., Adib, A., Najib, M., Faris Norazmi, M., Intry, M. K., Jian, Y., Hissein Didane, D., Manshoor, B., & Kabrein, H. A. (2023). Journal of Design for Sustainable and Environment Computational Fluid Dynamics Simulations of Multi-blade Savonius Wind Turbine. *JDSE Journal of Design for Sustainable and Environment*, *5*(2), 1–10. http://www.fazpublishing.com/jdse

Zikanov, O. (2019). *Essential computational fluid dynamics*. John Wiley & Sons.

APPENDICES

Appendix A: Drawings for parts and assemblies

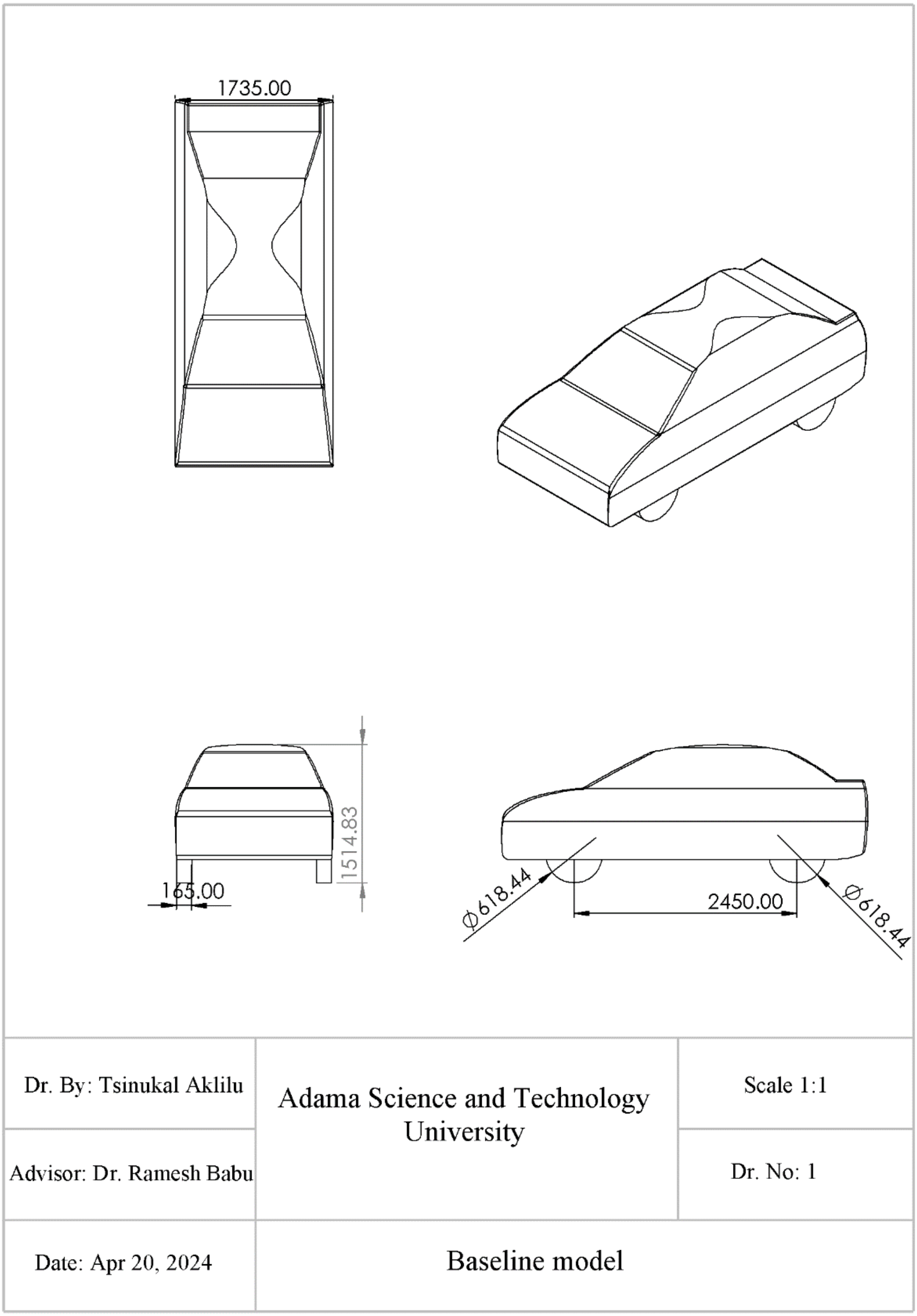

Figure A.1. Multiview of the baseline model

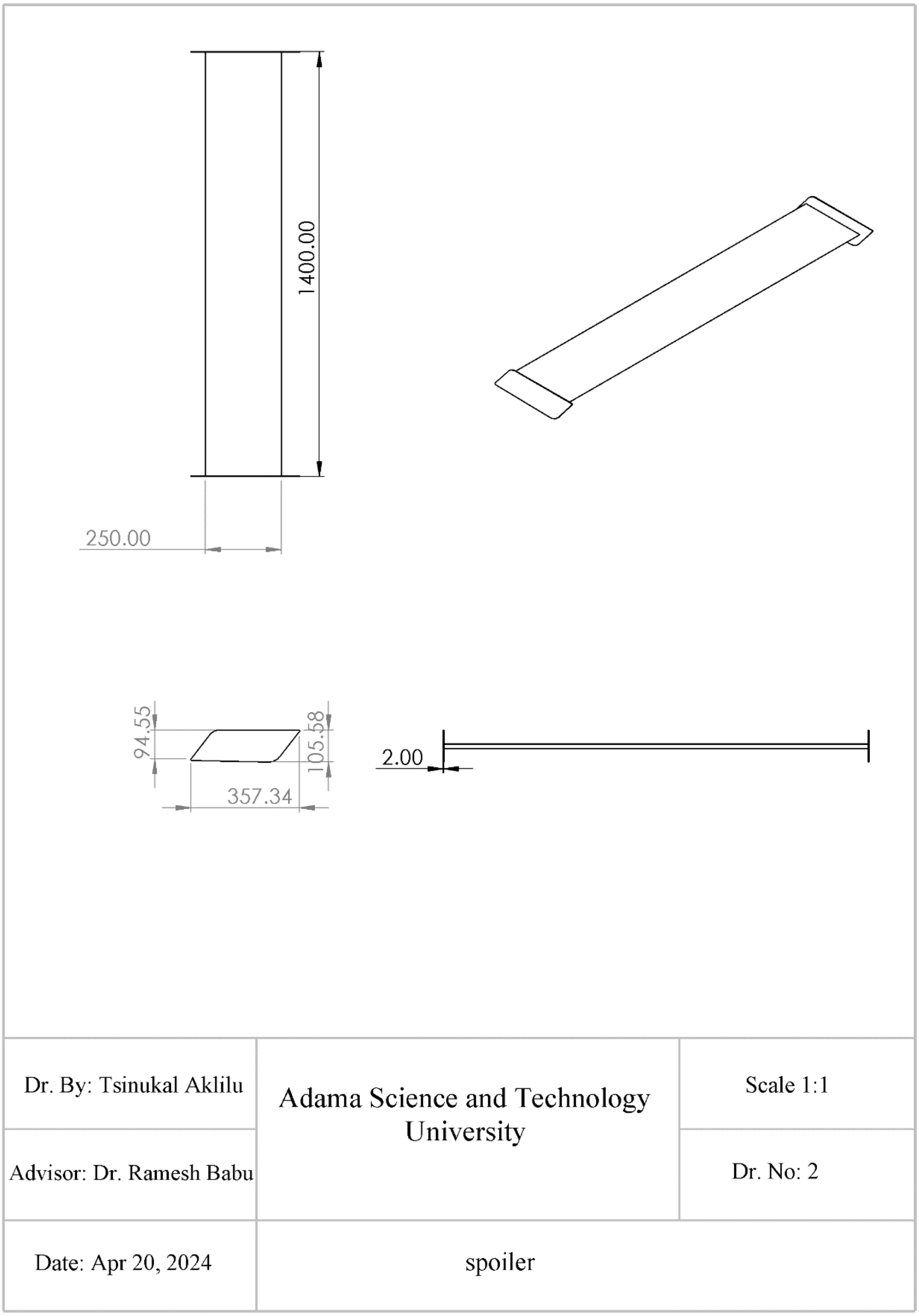

Figure A. 2. Multiview of the wing type spoiler model

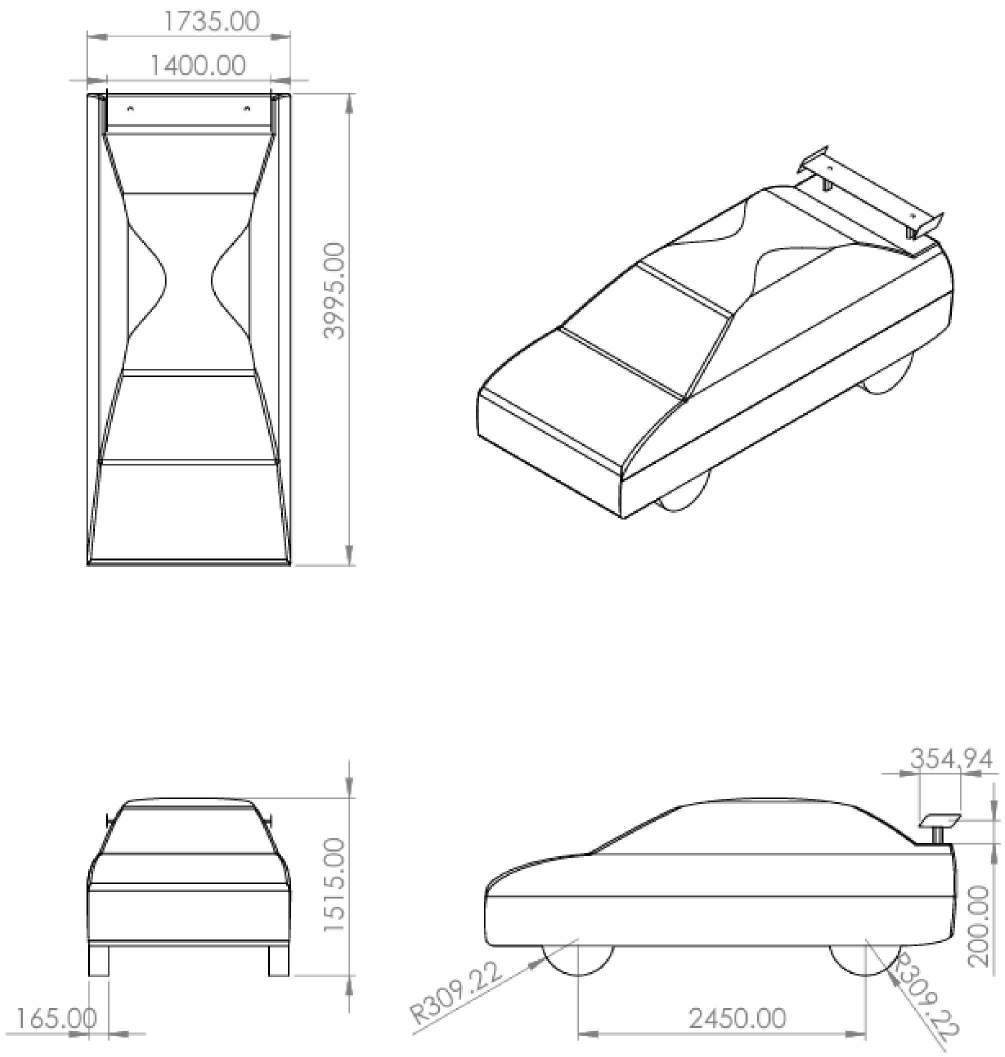

Dr. by: Tsinukal Aklilu	**Adama Science and Technology University**	**Scale 1:1**
Advisor: Dr. Ramesh Babu		**Dr.No: 3**
Date: Apr 20,2024	**Model one**	

Figure A. 3. Multiview of the model one

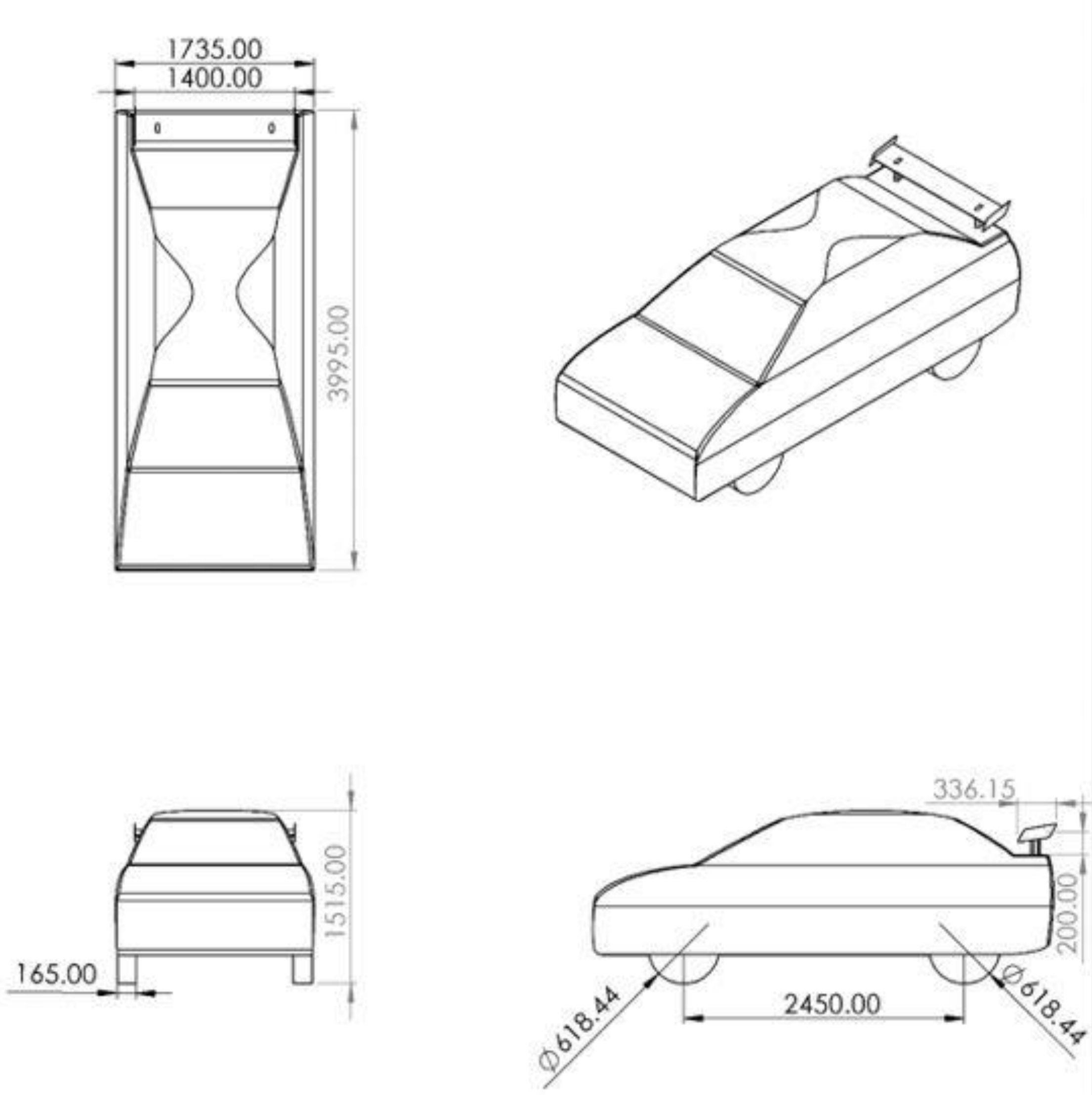

Dr. By: Tsinukal Aklilu	Adama Science and Technology University	Scale 1:1
Advisor: Dr. Ramesh Babu		Dr. No: 4
Date: Apr 20, 2024	**Model two**	

Figure A. 4. Multiview of the model two

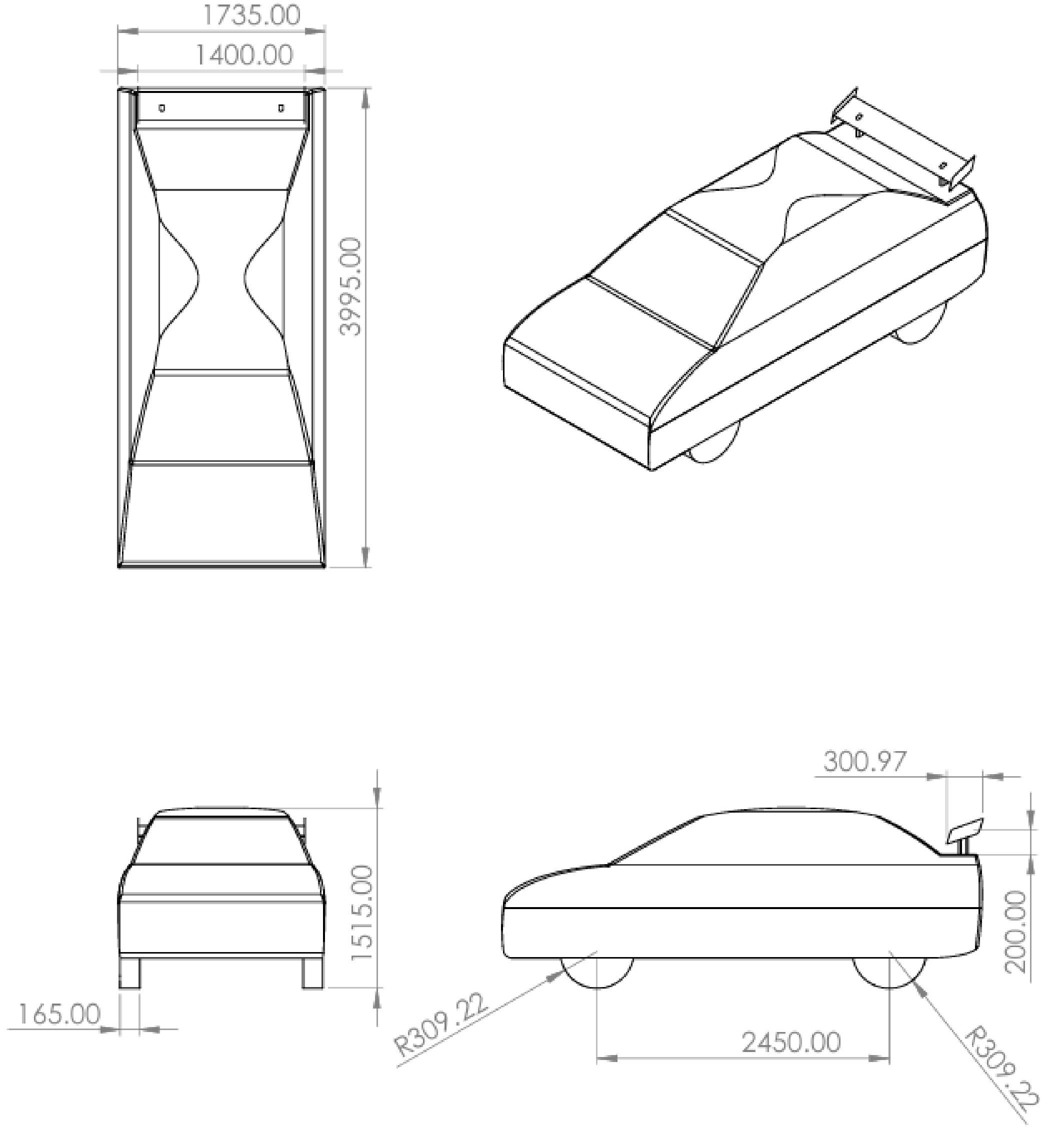

Dr. by: Tsinukal Aklilu	**Adama Science and Technology University**	**Scale 1:1**
Advisor: Dr. Ramesh Babu		**Dr.No: 5**
Date: Apr 20,2024	**Model three**	

Figure A. 5. Multiview of the model three

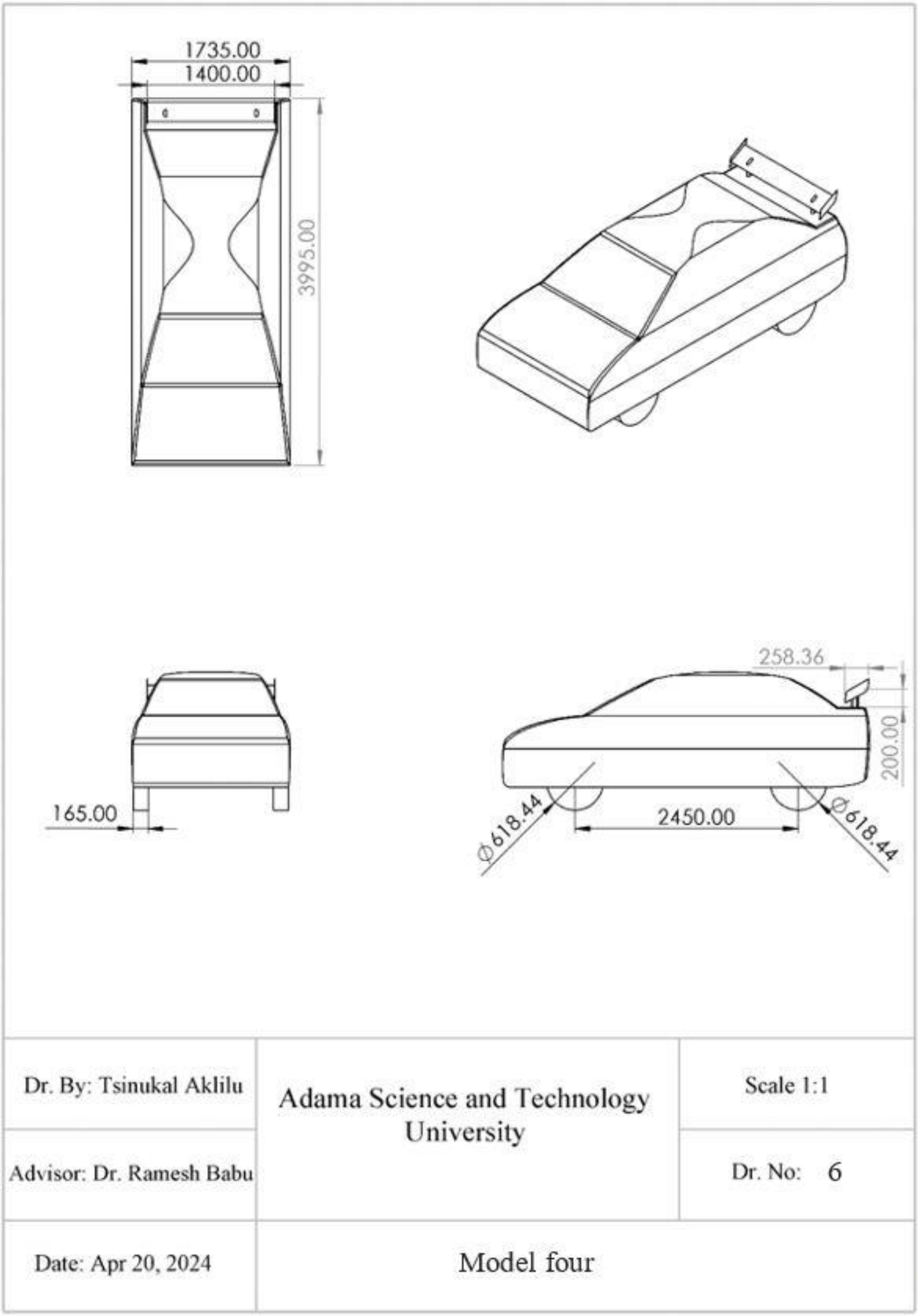

Figure A. 6. Multiview of the model four

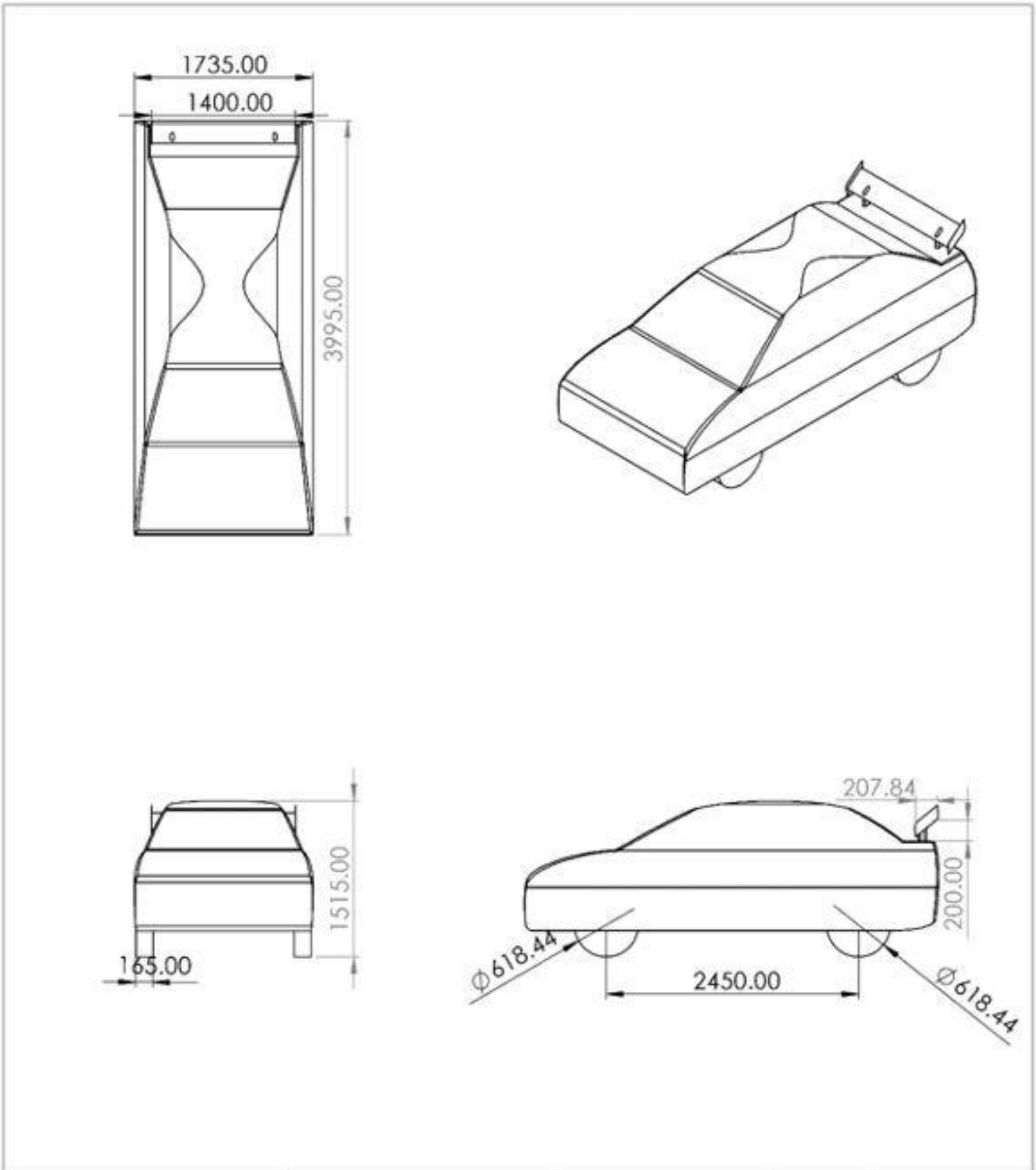

Dr. By: Tsinukal Aklilu	Adama Science and Technology University	Scale 1:1
Advisor: Dr. Ramesh Babu		Dr. No: 7
Date: Apr 20, 2024	Model five	

Figure A. 7. Multiview of the model five

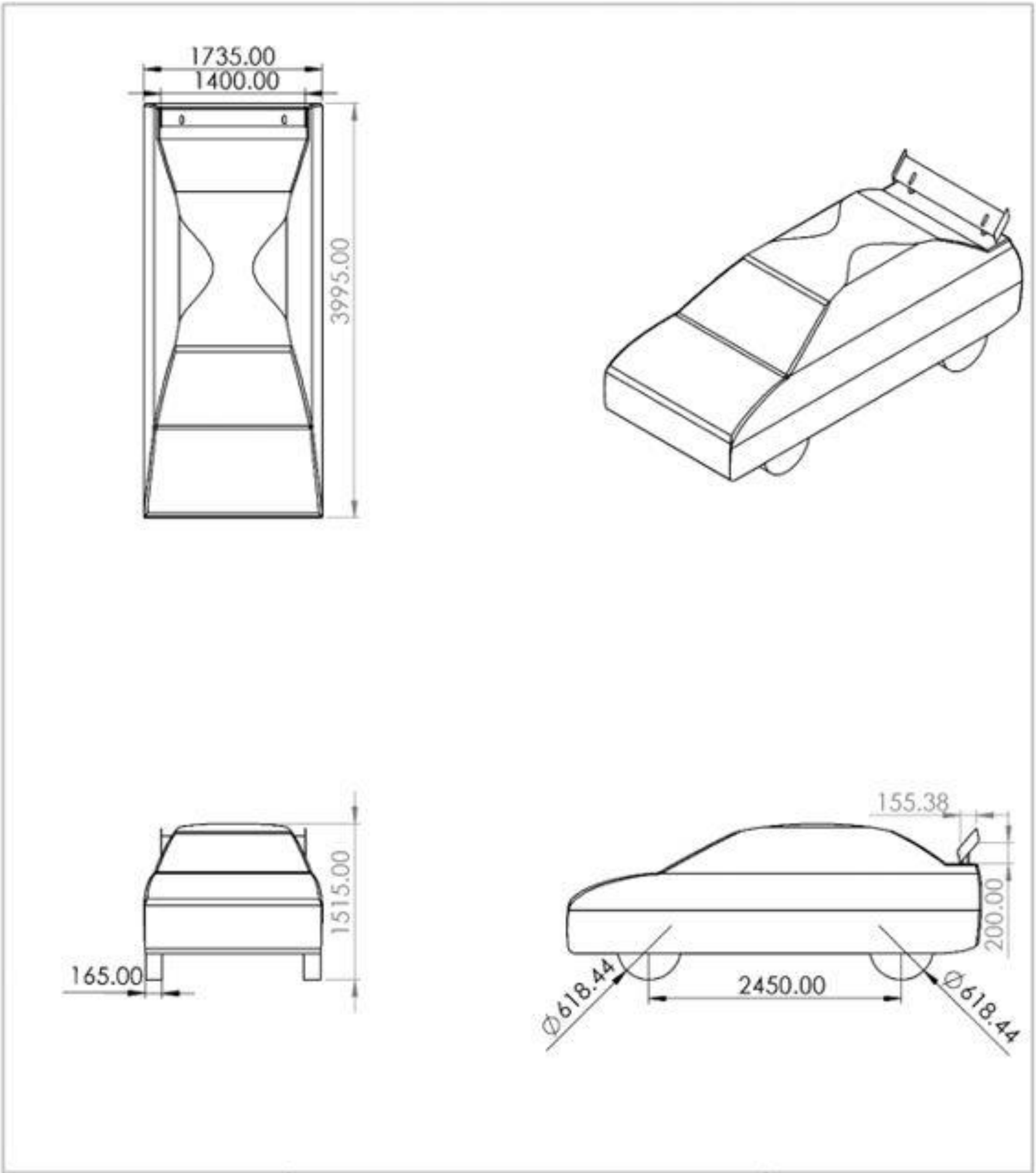

Dr. By: Tsinukal Aklilu	Adama Science and Technology University	Scale 1:1
Advisor: Dr. Ramesh Babu		Dr. No: 8
Date: Apr 20, 2024	Model six	

Figure A. 8. Multiview of the model six

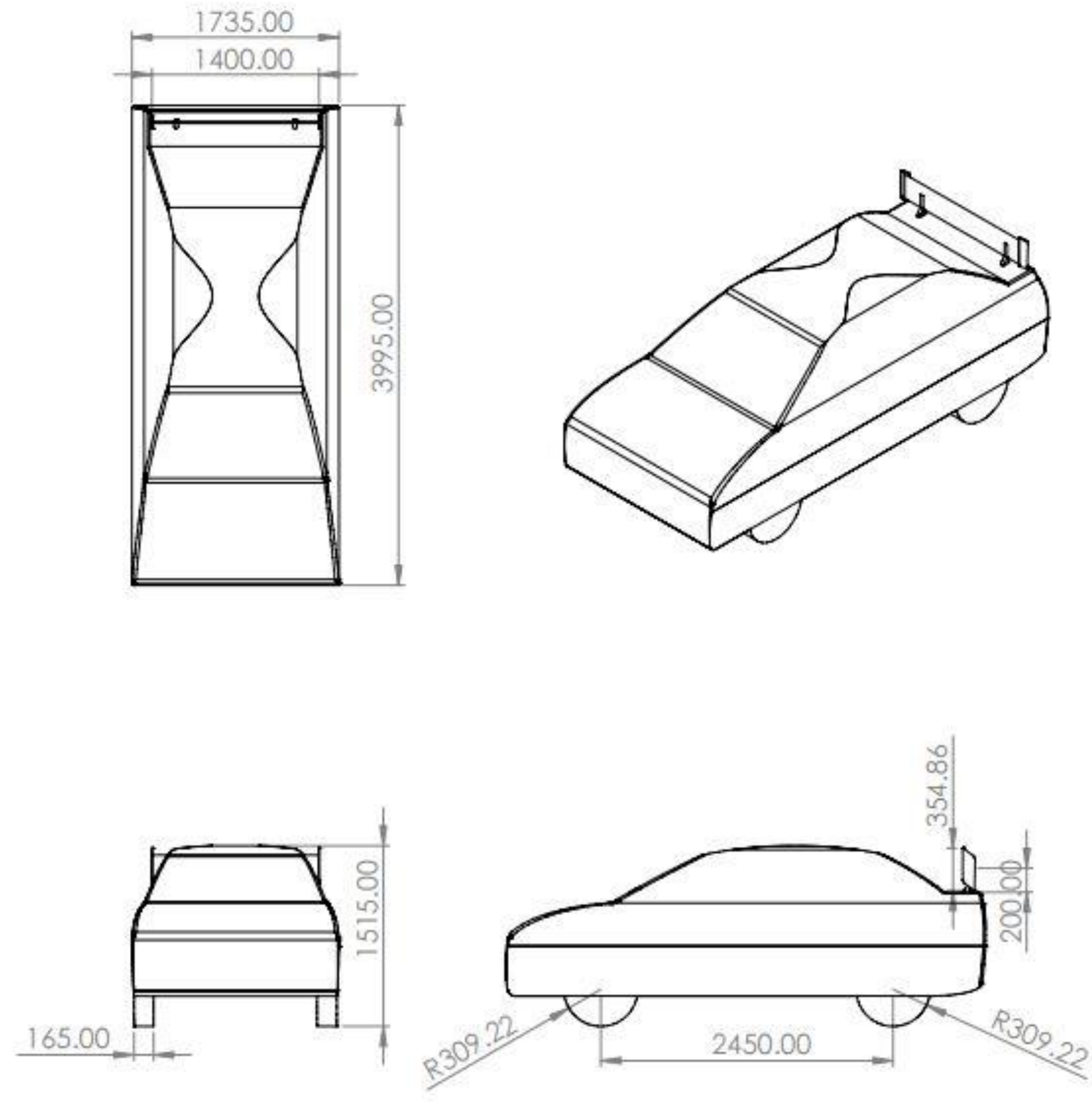

Dr. by: Tsinukal Aklilu	**Adama Science and Technology University**	**Scale 1:1**
Advisor: Dr. Ramesh Babu		**Dr.No: 9**
Date: Apr 20,2024	**Model seven**	

Figure A.9. Multiview of the model seven

Appendix B: Scaled Residual Convergence

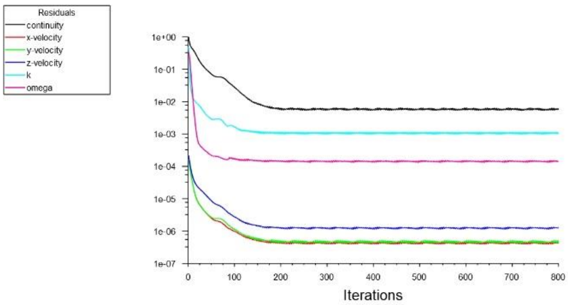

Model one

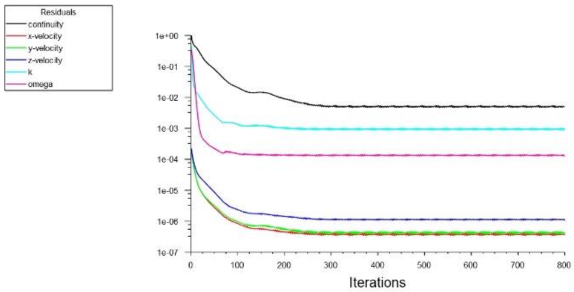

Model two

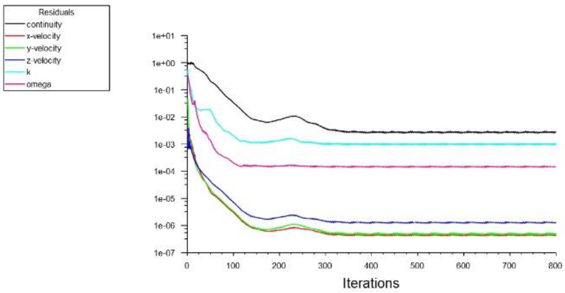

Model three

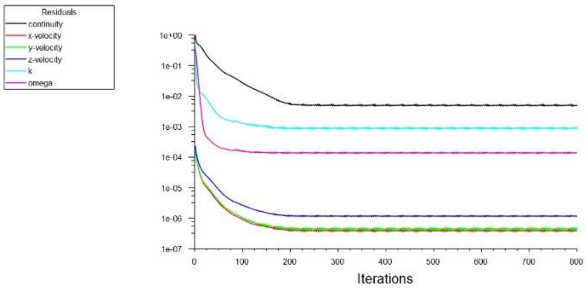

Model four

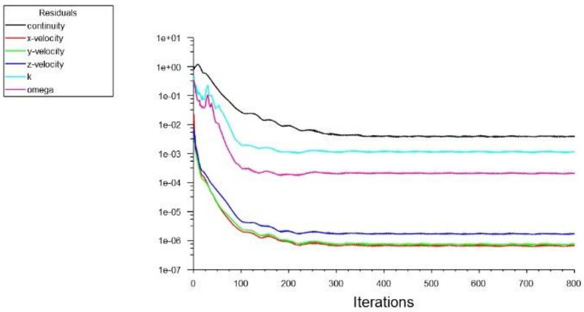

Model five

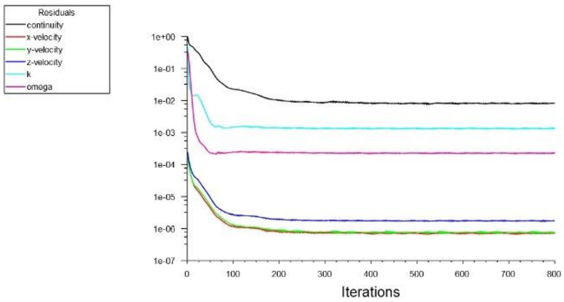

Model six

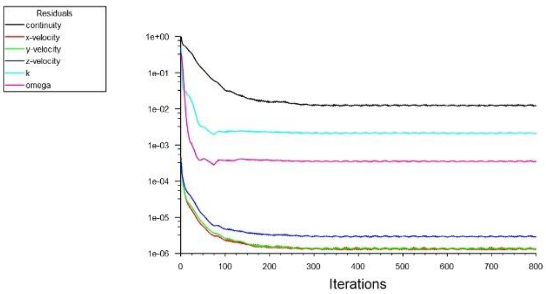

Model seven

Figure B.1. Scaled Residual Convergences of all models

Appendix C: Wind tunnel test and result

Figure C.1. Prototype in wind tunnel

Table C.1. C_d result of Prototype with a 0-degree spoiler inclination at different speed

	Speed m/s	C_d
Prototype with a 0-degree spoiler inclination	14	0.5245
	19.6	0.4683
	25.2	0.4435

Table C.2. C_d result of Prototype with a 20-degree spoiler inclination at different speed

	Speed m/s	C_d
Prototype with a 20-degree spoiler inclination	14	0.5956
	19.6	0.5352
	25.2	0.5566

Table C. 3. C_d result of Prototype with a 30-degree spoiler inclination at different speed

	Speed m/s	C_d
Prototype with a 30-degree spoiler inclination	14	0.6011
	19.6	0.5855
	25.2	0.6088

Table C. 4. C_d result of Prototype with a 50-degree spoiler inclination at different speed

	Speed m/s	C_d
Prototype with a 50-degree spoiler inclination	14	0.6334
	19.6	0.6133
	25.2	0.6240

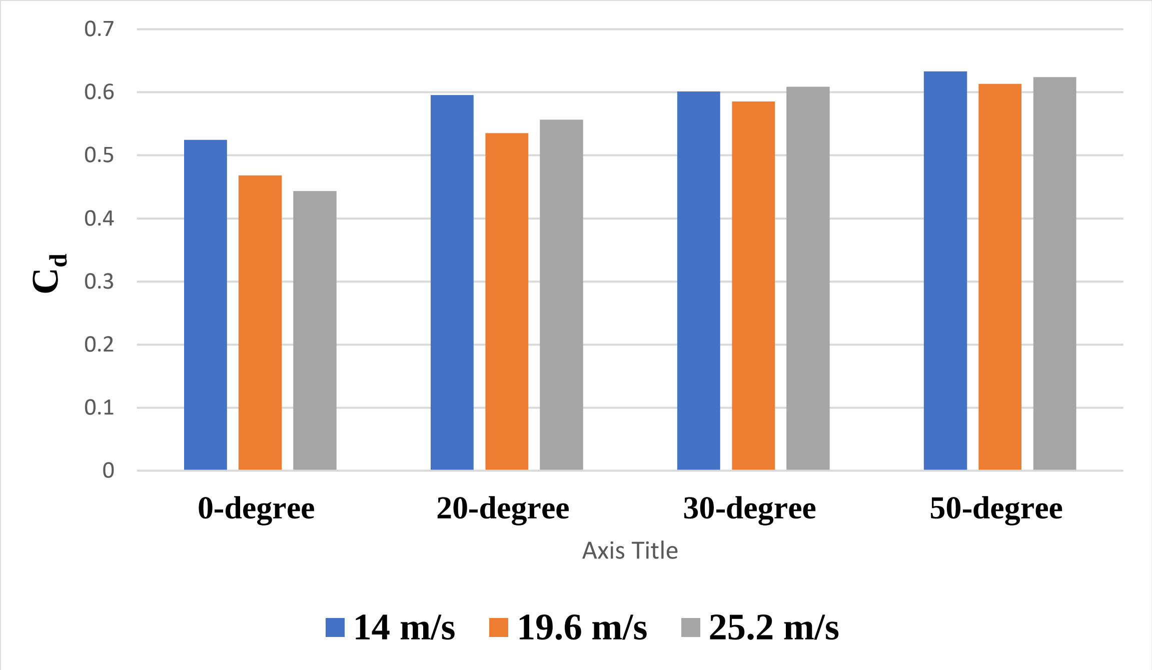

Figure C.2. Comparison of the drag coefficient of a prototype at different spoiler angles of inclination and various speeds

Appendix D: Code for programming an Arduino board

```
#include <LiquidCrystal.h> // initialize the library by associating any needed LCD interface pin

const int rs = 13, en = 12, d4 = 11, d5 = 10, d6 = 9, d7 = 8; // define the pins connected to the LCD's

LiquidCrystal lcd(rs, en, d4, d5, d6, d7);

int relayPin = 1; // Sets the pin number for the relay

float rev=0;

int rpm;

int kmh;

int oldtime=0;

int time;

void isr()                    //interrupt service routine, only in pin number 2 or pin number 3

{

rev++;

}

void setup()

{

pinMode(relayPin, OUTPUT);

lcd.begin(16,2);              //initialize LCD

attachInterrupt(0,isr,FALLING);  //attaching the interrupt

}

void loop()

{

delay(1000); // Creates a one-second delay
```

```
detachInterrupt(0);
time=millis()-oldtime;        //finding total time for one rev
rpm=(rev/time)*60000;//calculating the rpm
kmh=rpm * 0.045; //  Estimates the speed in kilometers per hour
oldtime=millis();
rev=0;
lcd.clear();  // Clears the LCD screen.
lcd.setCursor(0,0); //
lcd.print("  vehicle speed  ");    //printing on LCD
lcd.setCursor(0,1);              //sets the position where to print
lcd.print(     kmh);
lcd.print("     km/h");
lcd.print("   "); //final result
attachInterrupt(0,isr,FALLING);
if (kmh <80 ){
digitalWrite(relayPin,LOW);
}        //   If the speed is below 80 km/h, the relay pin is set to LOW
if (kmh >80 ){
digitalWrite(relayPin,HIGH);
}       //    If the speed is above 80 km/h, the relay pin is set to HIGH
}
```